12-2021

Improvement Opportunities in the Two-Source Energy Balance Model for ET using UAV Imagery and Point Cloud Information

Mahyar Aboutalebi
Utah State University

IMPROVEMENT OPPORTUNITIES IN THE TWO-SOURCE ENERGY BALANCE MODEL FOR ET USING UAV IMAGERY AND POINT CLOUD INFORMATION

by

Mahyar Aboutalebi

A dissertation submitted in partial fulfillment
of the requirements for the degree

of

DOCTOR OF PHILOSOPHY

in

Civil and Environmental Engineering

Approved:

Alfonso F. Torres-Rua, Ph.D. Major Professor	Mac McKee, Ph.D. Committee Member
Lawrence Hipps, Ph.D. Committee Member	William P. Kustas, Ph.D. Committee Member
Niel Allen, Ph.D. Committee Member	D. Richard Cutler, Ph.D. Interim Vice Provost of Graduate Studies

UTAH STATE UNIVERSITY
Logan, Utah

2021

ABSTRACT

Improvement opportunities in the Two-Source Energy Balance Model for ET using UAV imagery and point cloud information

by

Mahyar Aboutalebi, Doctor of Philosophy

Utah State University, 2021

Major Professor: Alfonso F. Torres-Rua, Ph.D.
Department: Civil and Environmental Engineering

Unmanned aerial vehicles (UAVs) are a rapidly developing technology for acquiring high-resolution imagery at the desirable location and time. With the recent advances in accelerating image processing algorithms and sensor technology, UAV high resolution imagery is one of the main sources for monitoring crop conditions in agricultural fields and in a short time interval. This UAV technology is now being used on farms and particularly on high-value crops such as orchards and vineyards to estimate evapotranspiration (ET) and stress of individual plants, an important feature that is not possible using satellite imagery. However, with increasing image resolution, new challenges/opportunities emerge. The current study has been conducted in response to improving the estimation of crop water requirement and irrigation scheduling using the integration of spatially-distributed information that can be derived from high-resolution imagery into remote sensing evapotranspiration (ET) model. The UAV high-resolution imageries have been collected over a California vineyard during the Grape Remote sensing Atmospheric Profile and Evapotranspiration eXperiment (GRAPEX) field campaigns. First, several existing approaches for shadow detection used in satellite imagery are evaluated for high-resolution UAV imagery

and the impacts of shaded pixels on vegetation indices and ET estimates using the Two-Source energy balance (TSEB) model are presented. Second, an open source algorithm is developed to extract useful information from UAV point cloud products for modeling Leaf Area Index (LAI), which is a key input for the TSEB model. Third, a new algorithm is designed to downscale radiometric temperature (Tr) to the spatial resolution of the optical bands and the impact of downscaled Tr on the TSEB is discussed. The information provided by the shadow detection model, LAI and downscaling algorithms has the potential to increase precision in irrigation water allocation and scheduling.

(192 pages)

PUBLIC ABSTRACT

Improvement opportunities in the Two-Source Energy Balance Model for ET using UAV imagery and point cloud information

Mahyar Aboutalebi

In recent years, satellites and unmanned aerial vehicles (UAVs) provide enormous amounts of spatially-distributed information for monitoring crop conditions by measuring crop's reflected and emitted radiation at a distance. However, applications of high-resolution UAV imagery and its intermediate products for improving crop water use estimates are not well studied. In other words, the available approaches, methods and algorithms for determining how much water to apply for irrigation using remotely sensed data have been mostly developed at satellite spatial resolutions. High-resolution imageries that have been achieved by small UAVs open new opportunities for revisiting, re-evaluating, and revising available crop water use methods. In this study, different aspects of opportunities of UAV high-resolution imagery for enhancing remote sensing crop water use models, notably the Two-Source Energy Balance model (TSEB), over a commercial vineyard located in California are presented. In particular, this dissertation presents the impact of shadows, leaf area index (LAI) modeled from UAV 3D information, and higher-resolution temperature on the TSEB model. The high-resolution spatially-distributed crop water use derived by integration of UAV imagery into the TSEB model provides the capability to visualize spatial variations of crop water use at a compatible resolution with irrigation systems. This information is an essential part of scheduling irrigation with greater precision.

ACKNOWLEDGMENTS

I would like to express my sincere appreciation to Dr. Alfonso Torres-Rua for his valuable advice and his role in directing my attention toward the practical utility of my present and future work. Special thanks to Dr. McKee, Dr. Kustas, Dr. Hipps and Dr. Allen for their guidance throughout the research and for supporting me during these years. I would like to thank Utah Water Research Laboratory and Utah State University for supporting my research. I acknowledge the extraordinary efforts of the AggieAir flight team and the viticulture department of the E&J Gallo company, whose cooperation greatly improved the data collection procedure. I would like to express my gratitude to my parents "Mohammad Reza" and "Maryam" and my sister "Mahsa" for their continuous and unparalleled love and for their unfailing emotional support. And last but not least, I give my special thanks to my wife and my best friend "Irene" for her love, unconditional support, and her encouragement. Irene has been extremely supportive of me throughout this entire process and has made countless sacrifices to help me get to this point.

Mahyar Aboutalebi

CONTENTS

LIST OF TABLES

LIST OF FIGURES

ACRONYMS

EVI	Enhanced Vegetation Index
HSI	Hue-Saturation-Intensity
NDSI	Normalized Difference Snow Index
NDWI	Normalized Difference Water Index
MLC	Maximum Likelihood Classifier
ARVI	Atmospherically Resistant Vegetation Index
DN	Digital Number
SIFT	Scale Invariant Feature Transformation
VNIR	visible and NIR
DTM	Digital Terrain Model
IMU	Inertial Measurement Unit
ANOVA	analysis of variance
G	soil heat flux
H	sensible heat flux
LE	latent heat flux
Rn	net radiation flux
NIR	near-infrared
ASTER	Advanced Space-borne Thermal Emission and Reflection Radiometer
Sfm	Structure from Motion
LiDAR	Light Detection and Ranging
CSM	Crop Surface Model
GCP	ground control point
CHM	canopy height model
DEM	Digital Elevation Model
DTM	Digital Terrain Model
PCA	Plant Canopy Analyzer
RTK	Real-time kinematic
TIN	triangulated irregular network
CSV	comma-separated values
GP	Genetic Programming
GA	Genetic Algorithm
IOP	Intensive Observation Period
ANN	Artificial Neural Network
TSEB	Two-Source Energy Balance Model

agl	above ground level
ESRI	Environmental Systems Research Institute
USU	Utah State University
G-LiHT	Goddard's LiDAR, Hyperspectral & Thermal Imager
IRGA	Infrared Gas Analyzer
S_n	Net Shortwave Radiation
L_n	Net Longwave Radiation
Ln_c	Canopy Net Longwave Radiation
Ln_s	Soil Net Longwave Radiation
Sn_c	Canopy Net Shortwave Radiation
Sn_s	Soil Net Shortwave Radiation
Rn_c	Canopy Net Radiation
Rn_s	Soil Net Radiation
G	Soil Heat Flux
H_c	Sensible Heat Flux for Canopy
H_s	Sensible Heat Flux for Soil
LE_c	Latent Heat Flux for Canopy
LE_s	Latent Heat Flux for Soil
R^2	Coefficient of Determination
MAE	Mean Absolute Error
RMSE	Root Mean Square Error
RRMSE	Relative Root Mean Square Error
RTK	Real-Time Kinematic
R_v	Average of R for Vegetation
G_v	Average of G for Vegetation
B_v	Average of B for Vegetation
N_v	Average of N for Vegetation
$NDVI_v$	Average of NDVI for Vegetation
h_v	Average of Vegetation Heights
$Volume_v$	Volume of Vegetation
$SArea_v$	Surface area of Vegetation
$Area_v$	Projected of $SArea_v$
R_{vc}	Average of R for Vine Canopy
G_{vc}	Average of G for Vine Canopy
B_{vc}	Average of B for Vine Canopy
N_{vc}	Average of N for Vine Canopy
$NDVI_{vc}$	Average of NDVI for Vine Canopy
h_{vc}	Average of Vine Canopy Height
$Volume_{vc}$	Volume of Vine Canopy
$SArea_{vc}$	Surface Area of Vine Canopy
$Area_{vc}$	Projected of $SArea_{vc}$
f_c	Fractional Cover
w_c	Canopy Width
$S1$	Scenario 1
$S2$	Scenario 2
$S3$	Scenario 3

VSSIXA	Vegetation Structural-Spectral Information eXtraction Algorithm
LST	Land Surface Temperature
DWT	Discrete Wavelet Transform
DT	Decision Tree
DTER	Ensemble Decision Tree
SVM	Support Vector Machine
GPR	Gaussian process regression
Dtr	downscaled Tr
GEOS	Geostationary Orbiting Environmental Satellite
AVHRR	Advanced Very High Resolution Radiometer
MODIS	Moderate Resolution Imaging Spectroradiometer
TME	thermal mixture effect
$NDVI_s$	NDVI soil threshold
$NDVI_c$	NDVI canopy threshold
PDM	physical downscaling method
SDM	statistical downscaling method
BR	Bowen ratio
LL	low-low
HL	high-low
LH	low-high
HH	high-high
LR	linear regression
RLR	robust linear regression
ILR	inter-actions linear regression
SLR	step-wise linear regression
Tr	Radiometric Temperature
DTr	Downscaled Radiometric Temperature
DSM	Digital Surface Model
NDVI	Normalized Difference Vegetation Index
CMOS	Complementary Metal Oxide Semiconductor
(ξ)	permitted error
C	penalty coefficienc
κ	actual absolute error
ET	Evapotranspiration
UAV	Unmanned Aerial Vehicle
RS	Remote Sensing
DSM	Digital Surface Model
T_s	soil temperature
T_c	canopy temperature
T_a	air temperature

CHAPTER 1

Introduction

One of the major components in water balance model for increasing crop water use efficiency is Evapotranspiration (ET) [4]. ET can be measured using lysimeters and eddy covariance towers or estimated based on empirical or physically-based models. Although field-based observations based on lysimeters and eddy covariance towers are considered as the most accurate methods for measuring ET, such measurements are expensive and are made at point scale. In contrast to lysimeters and eddy covariance towers, various remotely-sensed ET models have been developed providing estimation of ET across a variety of spatial and temporal scales using satellite and aerial imagery. However, physically-based models suffer from two major challenges: (1) input requirements and (2) model complexity. The complexity of ET models increases in non-homogeneous areas where both soil and vegetation contribute to radiometric temperature (Tr) and surface energy fluxes [9].

Among available remote sensing-based ET models, the Two-Source Energy Balance Model (TSEB) is one ET model that successfully estimates spatially-distributed surface energy fluxes from remotely-sensed land surface temperature over various types of crops. To overcome the challenges related to the impact of canopy geometry characteristics, sensor view, and solar zenith angle on the Tr and consequently on the surface temperature, the original version of the TSEB model was developed to estimate surface energy fluxes using a single measurement of Tr at one view angle [2]. In the past few years, the TSEB model outputs are evaluated at different grid sizes, climate conditions, and landscape heterogeneity ([6], [4], [1], [8], [3], and [5]).

The development of lightweight unmanned aerial vehicles (UAVs) provides an opportunity for collecting high-resolution multi-spectral imagery. Image processing and photogrammetry algorithms working at high spatial resolution offer a great opportunity for producing ortho-mosaics and 3D information products such as point cloud dataset. While UAV im-

agery has been widely used in crop water stress, yield monitoring, crop type identification, and weed and pest detection, the application of UAV 3D products such as point clouds in precision water management has not been well evaluated. Point clouds can be generated with overlapping UAV imagery. This information is likely to be a useful source for estimation of biomass parameters that can be more directly correlated to LAI.

Although UAVs are cost-effective and can provide higher resolution imagery, increases in resolution may lead to opening new opportunities as well as creating new challenges for available crop water requirement methods since most of these approaches have been developed, tested and enhanced at satellite resolution. Concerning new challenges, shadows are one of the objects that will appear in the high resolution imagery and affect the signal received by optical and thermal sensors. The occurrence of shadows in high-resolution imagery can affect vegetation indices and consequently estimated bio-physical parameters such as leaf area index (LAI), which is a key component for ET models.

Regarding new opportunities, one overlooked factor in ET models is the incorporation of vegetation-canopy structure information derived from multi-spectral imagery and photogrammetry algorithms into evapotranspiration models. In general, canopy structure information is the main source of information for (1) projection of shadows on the canopy and the ground and (2) estimation of biomass parameters such as LAI. In addition to vegetation-canopy structure information, spatial resolution differences between optical and thermal bands of UAV sensors can provide a unique opportunity for downscaling land surface temperature (LST) based on information derived from optical bands. This research explores different aspects of these challenges and opportunities for improving the performance of remote sensing ET models, particularly TSEB, over a commercial vineyard located in California.

The first chapter reveals how shadows caused by canopy structure, sun position, and geographical location can affect vegetation indices (VIs) and energy fluxes estimated by TSEB. TSEB doesn't consider the effect of shadows that appear in the high-resolution imagery captured by UAV. Because of shaded pixels in the high-resolution imagery, VIs

such as the Normalized difference vegetation index (NDVI), LAI, and empirical relationship between NDVI and Tr for component temperature estimation are affected. Divergence of NDVI values due to lack of incident radiation can lead to a bias in LAI, temperature components, and consequently ET estimation. This chapter evaluates the performance of four shadow detection methods in high-resolution UAV imagery. The shadow detection methods are (1) unsupervised and (2) supervised classifications, (3) an index-based method, and (4) a physically-based model for shadow projection that uses sun position and a digital surface elevation model generated from point cloud dataset. Four high-resolution images (less than 20 cm/pixel) captured by the AggieAir UAV system in 2014, 2015, and 2016 over a vineyard located in near Lodi, California, are used in this chapter. Finally, the impacts of shadowed areas on the calculation of the VIs LAI and surface energy fluxes are presented.

In the second chapter, a new algorithm called Vegetation Spectral-Structural Information eXtraction Algorithm (VSSIXA) is developed. VSSIXA can estimate plant parameters such as canopy height, volume and surface area based on point cloud dataset and provide spectral-structural canopy properties. The spectral-structural canopy properties are used to develop several LAI models. The TSEB model is executed based on these LAI models and the TSEB outputs are tested against eddy covariance flux measurements. Besides, instead of using nominal field values of canopy geometry characteristics as inputs to the TSEB model, maps of canopy height, canopy width, and fractional cover are used. The two main objectives for this chapter are to (1) improve the estimation of LAI and biomass parameters using point cloud dataset and (2) understand how spatially-distributed canopy parameters derived from VSSIXA can contribute to the TSEB model performance. The results reveal the correlation between in situ LAI measurements and estimated canopy geometry parameters from VSSIXA and improvement in the TSEB model when new LAI models and maps of canopy structure parameters are employed.

In the third chapter, a new algorithm for thermal sharpening is presented. To downscale LST, a wavelet-machine learning technique is used to (1) decompose the optical bands, VIs, and DSM to approximation and detail coefficients (using wavelet transform); (2) find a

possible relationship between approximation coefficients of those variables (VIs, DSM, etc.) and Tr (training/testing the network of the machine learning); (3) generate a detailed coefficient for Tr (applying the trained network); and (4) restore the higher resolution of Tr using inverse wavelet transform. Next, the high-resolution version of Tr is separated into Ts and Tc by searching for pure canopy and bare soil pixels in a spatial domain. TSEB is executed with pairs of Ts and Tc estimated from the original and downscaled Tr. Ultimately, TSEB outputs are evaluated using measurements of eddy covariance towers.

The objectives and hypotheses of these three chapters are tested for the same imagery from the Utah State University AggieAir UAV program as part of the USDA-ARS GRAPEX project conducted since 2014 over multiple vineyards located in California. These three chapters cover new challenges and opportunities into remote sensing ET models originated by UAV high resolution imagery that have not yet examined in detail.

Bibliography

[1] Aboutalebi, M.; Torres-Rua, A.F.; Kustas, W.P.; Nieto, H.; Coopmans, C.; McKee, M. Assessment of different methods for shadow detection in high-resolution optical imagery and evaluation of shadow impact on calculation of NDVI, and evapotranspiration. Irrigation Science, 2019, 37, 407–429.

[2] Anderson, M.C.; Norman, J.M.; Kustas, W.P.; Li, F.; Prueger, J.H.; and Mecikalski, J.R. Effects of Vegetation Clumping on Two–Source Model Estimates of Surface Energy Fluxes from an Agricultural Landscape during SMACEX. J. Hydrometeorol. 2005, 6, 892–909.

[3] Chávez, J.L.; Gowda, P.H.; Howell, T.A.; Neale, C.M.U.; and Copeland, K.S. Estimating hourly crop ET using a two-source energy balance model and multispectral airborne imagery. Irrigation Science, 2009, 28, 79–91.

[4] Colaizzi, P.D.; Kustas, W.P.; Anderson, M.C.; Agam, N.; Tolk, J.A.; Evett, S.R.; Howell, T.A.; Gowda, P.H.; and O'Shaughnessy, S.A. Two-source energy balance model estimates of evapotranspiration using component and composite surface temperatures. Adv. Water Resour, 2012, 50,134–151.

[5] Kustas, W.P.; Alfieri, J.G.; Nieto, H.; Wilson, T.G.; Gao, F.; and Anderson, M.C. Utility of the two-source energy balance (TSEB) model in vine and interrow flux partitioning over the growing season. Irrigation Science, 2019, 37, 375–388.

[6] Kustas, W.P.; Anderson, M.C.; Alfieri, J.G.; Knipper, K.; Torres-Rua, A.; Parry, C.K.; Nieto, H.; Agam, N.; White, A.; Gao, F.; McKee, L.; Prueger, J.H.; Hipps, L.E.; Los, S.; Alsina, M.; Sanchez, L.; Sams, B.; Dokoozlian, N.; McKee, M.; Jones, S.; Yang, Y.; Wilson, T.G.; Lei, F.; McElrone, A.; Heitman, J.L.; Howard, A.M.; Post, K.;

Melton, F.; and Hain, C. The Grape Remote sensing Atmospheric Profile and Evapotranspiration eXperiment (GRAPEX). Bulletin of the American Meteorological Society, https://doi.org/10.1175/BAMS-D-16-0244.1

[7] Nieto, H.; Kustas, W.; Torres-Rua, A.; Alfieri, J.; Gao, F.; Anderson, M.; White, A.; Song, L.; Mar Alsina, M.; Prueger, J.; McKee, M.; Elarab, M.; and McKee, L. Evaluation of TSEB turbulent fluxes using different methods for the retrieval of soil and canopy component temperatures from UAV thermal and multispectral imagery. Irrigation Science, 2019, 37, 389–406. https://doi.org/10.1007/s00271-018-0585-9

[8] Nieto, H.; Kustas, W.P.; Torres-Rúa, A.; Alfieri, J.G.; Gao, F.; Anderson, M.C.; White, W.A.; Song, L.; Alsina, M.; Prueger, J.H.; et al. Evaluation of TSEB turbulent fluxes using different methods for the retrieval of soil and canopy component temperatures from UAV thermal and multispectral imagery. Irrigation Science, 2019, 37,389–406.

[9] Timmermans, W.J.; Kustas, W.P.; Anderson, M.C.; and French, A.N. An intercomparison of the Surface Energy Balance Algorithm for Land (SEBAL) and the Two-Source Energy Balance (TSEB) modeling schemes. Remote Sens. Environ. 2007, 108, 369–384

CHAPTER 2

Assessment of different methods for shadow detection in high-resolution optical imagery and evaluation of shadows impact on calculation of NDVI, and evapotranspiration

2.1 Abstract

Significant efforts have been made recently in the application of high-resolution remote sensing imagery (i.e., sub-meter) captured by unmanned aerial vehicles (UAVs) for precision agricultural applications for high-value crops such as wine grapes. However, at such high resolution shadows will appear in the optical imagery effectively reducing the reflectance and emission signal received by imaging sensors. To date, research that evaluates procedures to identify the occurrence of shadows in imagery produced by UAVs is limited. In this study, the performance of four different shadow detection methods used in satellite imagery were evaluated for high-resolution UAV imagery collected over a California vineyard during the Grape Remote sensing Atmospheric Profile and Evapotranspiration eXperiment (GRAPEX) field campaigns. The performance of the shadow detection methods was compared and impacts of shadowed areas on the normalized difference vegetation index (NDVI) and estimated evapotranspiration (ET) using the Two-Source Energy Balance (TSEB) model are presented. The results indicated that two of the shadow detection methods, the supervised classification and index-based methods, had better performance than two other methods. Furthermore, assessment of shadowed pixels in the vine canopy led to significant differences in the calculated NDVI and ET in areas affected by shadows in the high-resolution imagery. Shadows are shown to have the greatest impact on modeled soil heat flux, while net radiation and sensible heat flux are less affected. Shadows also have an impact on the modeled Bowen ratio (ratio of sensible to latent heat) which can be used as an indicator of vine stress level.

2.2 Introduction

Unmanned aerial vehicles (UAVs) used for remote sensing (RS) purposes have become a rapidly developing technology for acquiring high-resolution imagery of the earth's surface. The use of UAVs for monitoring agricultural crop conditions has greatly expanded in recent years due to recent advances in high-resolution aerial image processing and sensor technology. These advances have extended the capability to measure crop conditions from a single field to multiple fields in a small time interval. The MIT Technology Review has listed Agricultural UAVs (or drones) as number one in 10 Breakthrough Technologies of 2014 [25]. UAVs now offer sub-meter resolution remote sensing relevant to water management through optical and thermal imagery and evapotranspiration estimation advances. This UAV technology is now being applied to high-value crops such as orchards and vineyards to assess individual plant water use or evapotranspiration (ET) and stress (Ortega-Farias et al. 2016 [32]; Nieto et al. this issue [30]). This enhanced sensing capability can provide information of plant water use and symptoms for biotic/abiotic stresses at individual plant scale, a capability not achievable with commercial or NASA satellite data. However, as image resolution increases, new challenges emerge such as data transfer and storage, image processing, and detection and characterization of finer-scale features such as plant canopy glint, blurriness due to wind, and shadows. Although in some cases shadows might not be a significant issue, they affect surface reflectance and temperature not accounted for in RS energy balance models, which in turn are likely to cause bias in determining plant water use and stress, among other parameters. Therefore, neglecting the shadow impact on monitoring and detecting plant water use and stress and soil moisture status might well result in less reliable assessments for high-value crops.

Shadows appear when elevated objects, such as buildings or trees, occlude and block the direct light (e.g. sun shortwave radiation) produced by a source of illumination. In some cases, information about shadows can provide additional clues about the geometric shape of the elevated object (Lillesand and Kiefer, 2000 [24]), the position of the source of light (Bethsda, 1997 [4]), and the height of the object (Sirmacek and Unsalan, 2008 [45]). In most

cases, the appearance of shadows in an image acquired by RS complicates the detection of objects or areas of interest that are located under the shaded area and thus reflect reduced radiance. The appearance of shadows in aerial imagery may also cause loss of valuable information about features, such as shape, height, and color. Consequently, the darkening effect of shadows increases land cover classification error and causes problems for remote sensing studies, such as calculation of vegetation indices and change detection (Zhu and Woodcock, 2012 [50]). Typical RS vegetation indices and outputs used in agriculture include NDVI, enhanced vegetation index (EVI), LAI (Carlson and Ripley, 1997 [6]), ET estimates (Nemani and Running, 1998 [29]), and land cover classification (Trout and Johnson, 2007 [48]), among others. In addition, sun position changes lead to moving and changing shadow locations. As a result, shadow detection algorithms have received widespread attention, primarily with respect to the impacts of shadows on satellite RS data.

Multiple studies have been conducted to develop methods that detect shadows in images captured by satellites, and several shadow detection methods have been documented. These methods can be categorized into four groups: (a) unsupervised classification or clustering, (b) supervised classification that employ tools such as artificial neural networks (ANNs) or support vector machines (SVMs), (c) Index-based methods, and (d) physically-based methods.

(a) Unsupervised classification/clustering: Xia et al. (2009) [49] presented an unsupervised classification/clustering algorithm to detect shadows using the affinity propagation clustering technique in the Hue-Saturation-Intensity (HSI) color space. Shiting and Hong (2013) [43] presented a clustering-based shadow edge detection method using K-means clustering and punishment rules to modify false alarms. Xia's results revealed that the proposed method has the capability of producing a robust shadow edge mask.

(b) Supervised classification/object-based methods: Kumar et al. (2002) [50] proposed an object-based method to detect shadows using a color space other than RGB. Siala et al. (2004) [44] worked on a supervised classification method to detect moving shadows using support vectors in the color ratio space. Zhu and Woodcock (2012) [50] presented an

object-based approach to detect shadows and clouds in Landsat imagery.

(c) Index-based methods: Scanlan et al. (1990) [42] reported a method to detect and remove shadows in images by partitioning the image into pixel blocks, calculating the mean of each block, and comparing it with the image median. Rosin and Ellis (1995) [38] worked on the impact of different thresholds on the detection of shadows in an index-based method. Choi and Bindschadler (2004) [7] presented an algorithm to detect clouds using normalized difference snow index (NDSI) to match plausible cloud shadow pixels based on solar position and Landsat7 images. Qiao et al. (2016) [36] used normalized difference water index (NDWI) and NDVI to separate shadow pixels from both water bodies and vegetation, and then applied a maximum likelihood classifier (MLC) and support vector machines (SVMs) to classify the shadow pixels. Kiran (2016) [17] converted an RGB color image to a grayscale image using the average of the three bands, and then used Otsus' method to define a threshold for differentiating between shadow and non-shadow pixels. Finally, a histogram equalization method was applied to improve the contrast of the grayscale image.

(d) Physically-based methods: Sandnes (2010) [40] used the sun position and shadow length to approximately estimate the geolocation of the sensor. Huang and Chen (2009a) [15] presented a physical approach for detecting the shadows in video imagery and showed that the proposed method can effectively identify the shadows in three challenging video sequences. Also, Huang and Chen (2009b) [16] proposed a method for detecting a moving shadow using physical-based features. In this method, the physical-based color features are derived using a bi-illumination reflection model. More information about physically-based models can be found in Sanin et al. (2012) [41].

Concerning the impact of shadows on vegetation indices and water stress, Ranson and Daughtry (1987) [37] and Leblon et al. (1996a) [22] concluded that NDVI estimates were highly sensitive to the shaded part of a forest canopy. Leblon et al. (1996b) [23] analyzed the mean sunlit and shadow reflectance spectra of shadows cast by a building and by conifers and hardwood trees on grass, bare soil, and asphalt using the visible and near-infrared bands. Their results indicated that reflectance of hardwood shadows was greater

than those of conifers and buildings, except for shadow reflectance on bare soil. Moreover, the average NDVI and the atmospherically resistant vegetation index (ARVI) in sunlit areas could be lower or higher than in shaded areas depending on the surface type and shadow type. Hsieh et al. (2016) [14] analyzed the spectral characteristics in the shadow areas and also investigated the NDVI differences between shaded and non-shaded land covers using high radiometric resolution digital imagery obtained from Leica ADS-40, Intergraph DMC airborne. They found that digital number (DN) values in shaded pixels are much lower than in sunlit pixels and also reported NDVI mean values in shadows and non-shadows from the vegetation category of 0.38 and 0.64, respectively. Poblete et al. (2018) [34] proposed an approach to detect and remove shadow canopy pixels from high-resolution imagery captured by a UAV using a modified scale invariant feature transformation (SIFT) computer version algorithm and Kmeans++ clustering. Their results indicated that deletion of shadow canopy pixels from a vineyard leads to an improved relationship between the thermal-based Crop Water Stress Index and stem water potential (13% in terms of the coefficient of determination). They also concluded that the impact of shadow canopy pixel removal should be evaluated for ET models working with high-resolution imagery.

While the literature identifies several shadow detection approaches, a few studies have focused on shadow detection for very high-resolution imagery captured by UAVs. Furthermore, limited work is available that demonstrates how shadows might affect the interpretation of the imagery in terms of vegetation indices, biophysical parameters and ET. Therefore, the objectives of this study were to characterize the advantages and disadvantages of a version of each shadow detection model group using high-resolution imagery captured by UAVs over complex canopy locations like vineyards, and consider the impacts of shaded pixels on NDVI and ET estimations.

2.3 Material and Methods

2.3.1 Area of Study and UAV sensor descriptions

The high-resolution images for this study were collected by a small UAV over a Pinot

Noir vineyard located near Lodi, California (38.29 N 121.12 W), in Sacramento County as part of the GRAPEX project. It is a drip-irrigated system vineyard in which irrigation lines run along the base of the trellis at 30 cm agl with two emitters (4 liters/hour) between each vine. The training system is with "U" shaped trellises and canes trained upwards. The vine trellises are 3.35 m apart, and the height to first and second cordon is about 1.45 and 1.9 m, respectively (Kustas et al. 2018 [20]). The orientation of the vine rows is East-West. In terms of cycle of vine canopy growth in that area, the bud break (grape flowering state) occurs in early May, and the veraison to harvest stage occurs in early or mid-June to late August. Thus, June, July, and August are the months that the canopy may undergo stress. The UAV was supplied and operated by the AggieAir UAV Research Group at the Utah Water Research Laboratory at Utah State University ([7]). Four sets of high-resolution imagery (20 cm or finer) were captured over the vineyard by the UAV in 2014, 2015, and 2016. These UAV flights were synchronized with Landsat satellite overpass dates and times. The data were used to evaluate the various shadow detection methods. The study area is shown in Figure 2.1, and information describing the images is summarized in Table 2.1. Details of the AggieAir aircraft, along with sensor payload, are shown in Figure 2.2.

As described in Table 2.1, different optical cameras were used each year (2014, 2015, and 2016). Cameras ranged from consumer-grade Canon S95 cameras to industrial type Lumenera monochrome cameras fitted with narrowband filters equivalent to Landsat 8 specifications. The thermal resolution for all four flights was 60 cm and the visible and NIR (VNIR) were 10 cm except for the first one (15 cm).

A photogrammetric point cloud was produced from the multispectral images with a density of 40 ($points/m^2$) for the 15 cm resolution (2014 imagery) and 100 ($points/m^2$) for the 10 cm resolution (2015 and 2016 imagery), after which a digital surface model (DSM) was generated at the same spatial resolution than the original imagery (i.e. 15 cm for 2014 and 10cm for 2015 and 2016). In addition to UAV point cloud products that describe the surveyed surface, a LiDAR derived bare soil elevation (digital terrain model DTM) product for the same location, collected by the NASA G-LiHT project, were used [9]. Also, 2014

and 2015 images were captured between veraison and harvest stage, and the 2016 flight was between bloom and veraison stage (Table 2.2).

Following the imagery acquisition, a two-step image processing phase occurred, including (1) radiometric calibration and (2) image mosaicking and orthorectification. In the first step, the digital images are converted into a measure of reflectance by estimating the ratio of reference images from pre- and post-flight Labsphere ([21]) Lambertian panel readings. For this conversion, a method has been adapted from Neale and Crowther, 1994 [28]; Miura and Huete, 2009 [26]; and Crowther, 1992 [10]) that is based solely on the reference panel readings, which do not require solar zenith angle calculations. This procedure additionally corrected camera vignetting effects that were confounded in the Lambertian panel readings. In the second step, all images were combined into one large mosaic and rectified into a local coordinate system (WGS84 UTM 10N) using the Agisoft Photoscan software [2], and survey-grade GPS ground measurements. The software produced hundreds of tie-points between overlapping images by using photogrammetric principles in conjunction with image GPS log file data and UAV orientation information from the on-board Inertial Measurement Unit (IMU) to refine the estimate of the position and orientation of individual images. The output of this step is an orthorectified reflectance mosaic (Elarab et al. (2015) [11]). For thermal imagery processing, only step 2 is applied. The resulting thermal mosaic was brightness temperature in degrees Celsius. Moreover, a vicarious calibration for atmospheric correction of microbolometer temperature sensors proposed by Torres-Rua [47] was applied to the thermal images.

.

Fig. 2.1: Example of an aerial image of the study area captured by the AggieAir UAV on June 2015 (left), and NASA phenocam photographs for the same site (right, obtained on 24 March 2013 and 02 July 2 2013 during the growing season)

Table 2.1: Dates, times, cameras and optical filters used to capture images with the UAV

Date	UAV Flight Time (PDT)		UAV elevation	Bands		Cameras and Optical Filters		Spectral Response
	Launch Time	Landing Time	(agl) meters	RGB	NIR	Radiometric Response	MegaPixels	
August 9, 2014	11:30 AM	11:50 AM	450	Cannon S95	Cannon S95 modified (Manufacturer NIR block filter removed)	8-bit	10	RGB: typical CMOS NIR: extended CMOS NIR Kodak Wratten 750 nm LongPass filter
June 2, 2015	11:21 AM	12:06 PM	450	Lumenera Lt65R Color	Lumenera Lt65R Monochrome	14-bit	9	RGB: typical CMOS NIR: Schneider 820 nm LongPass filter
July 11, 2015	11:26 AM	12:00 PM	450	Lumenera Lt65R Color	Lumenera Lt65R Monochrome	14-bit	12	RGB: typical CMOS NIR: Schneider 820 nm LongPass filter
May 2, 2016	12:53 PM	1:17 PM	450	Lumenera Lt65R Mono	Lumenera Lt65R Mono	14-bit	12	RED: Landsat 8 Red Filter equivalent NIR: Landsat 8 NIR Filter equivalent

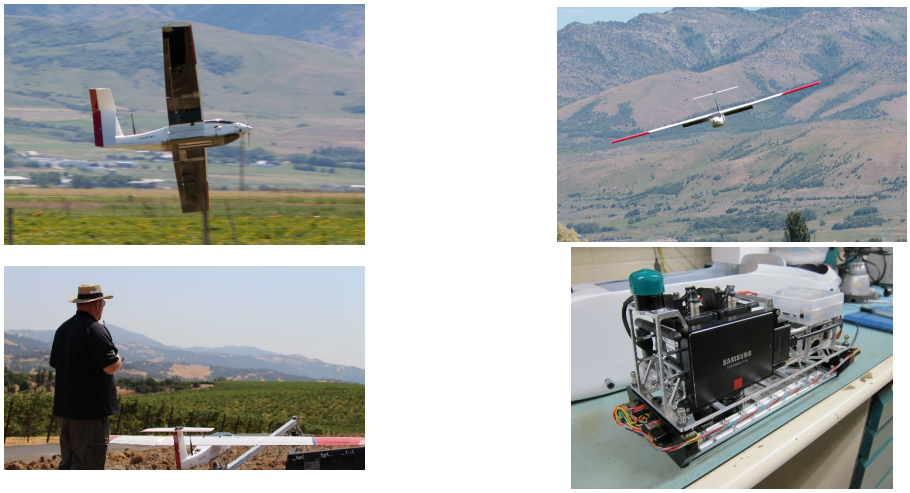

Fig. 2.2: Photos of the AggieAir aircraft and its sensor payload

Table 2.2: Dates, optical, DSM and thermal resolution, point cloud density and phenological stages of the vineyard when the images captured by the UAV

Dates	Optical and DSM resolution	Thermal resolution	Point cloud density (points/mˆ2)	Phenological stage
9-Aug-14	15 cm	60 cm	37	near harvest
2-June-15	10 cm	60 cm	118	near verasion
11-Jul-15	10 cm	60 cm	108	veraison to harvest
2-May-16	10 cm	60 cm	77	bloom to veraison

2.3.2 Shadow detection methods

Figure 2.3 provides a schematic overview of the four different shadow detection methods that were evaluated in this study. For unsupervised k-means classification, the value of k (maximum number of classes) must be determined. When using supervised classification, the signature spectra for each of the categories must be previously identified. The index-based method required that an index be calculated using two or more spectral bands and the identification of a threshold value (digital number or reflectance). Because the shadowed pixels can be visually identified, the threshold value can be modified in a trial-and-error process. Application of the physically-based model involved calculation of the sun position based on the central latitude and longitude of the imagery, together with the local time at

the flight area. Since the case study is not a large area (<0.4 km^2) and the flight time is less than 20 minutes, we can assume that the sun position is constant for all pixels.

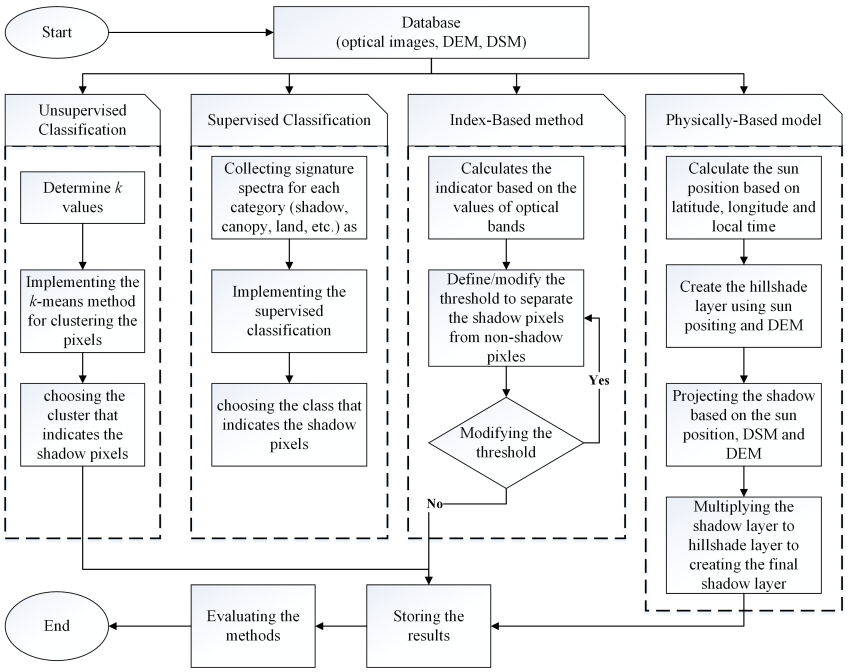

Fig. 2.3: Flowchart illustrating the process of the study for evaluating the shadow detection methods using the very high resolution images captured by UAV

To statistically determine the impact of shadows over NDVI, a standard analysis of variance (ANOVA) analysis was implemented. The ANOVA analysis compared shadowed and non-shadowed pixels over the canopy and was applied to the best of the four shadow detection methods.

To separate the canopy pixels from ground pixels, DTM and DSM products for each image acquisition date are used. If the difference between DSM and DTM was greater than a threshold (e.g. 30 cm), that pixel could be considered as belonging to the canopy vegetation; otherwise, it was assumed to be a pixel of bare ground/inter-row. This threshold filtered the canopy pixels in the images and its selection included a trial-and-error process.

Afterward, based on the filtering procedure and the evaluation of the shadow detection methods, the leaf canopy portions that were shaded or sunlit were extracted. From here,

NDVI was calculated and estimated separately for the shaded and sunlit portions of the canopy. For NDVI, the shadowed versus sunlit pixels were compared to each other in terms of histogram analysis and ANOVA. The null hypothesis for the ANOVA test is that the average of the two populations are similar (e.g. the mean values of the shaded and sunlit NDVI pixels were equal). If the null hypothesis was rejected, a further comparison was performed on how the difference in shaded versus sunlit could affect NDVI and ET.

2.4 Results and Discussion

2.4.1 Unsupervised classification (clustering)

Examples of the results of unsupervised classification (clustering) for shadow detection are illustrated in Figure 2.4 for the various flight dates over the study area. Five clusters were considered in applying the clustering method. These were generated based on the k-means method. The unsupervised classification toolbox of the ERDAS Imagine Software was used to execute the k-means algorithm. As shown in Figure 2.4, it is evident that most of the pixels assigned to Cluster 1 represent the pixels in shadows. Clusters 2 and 3 were mostly related to the sunlit vegetation canopy, and most of the pixels categorized into Clusters 4 and 5 were bare soil. In addition, some parts of the bare soil in the central part (dark pixels) of the 2015 images were classified as shadowed pixels (Cluster 1), which was not correct. Also, in the May 2016 image, some pixels classified in Cluster 5 (which were mostly bare soil pixels) overlapped with vegetation pixels. Thus, each cluster is a mixture of at least two features (shadow, soil, etc.) as different levels of shade (particularly the shadow over the canopy in the vine row) can be found in Cluster 2 not in Cluster 1. As shown in Table 2.1, only the red and NIR bands were used in 2016. This might have affected the performance of classification because it employed less information than was used for the imagery from the 2014 and 2015 UAV flights.

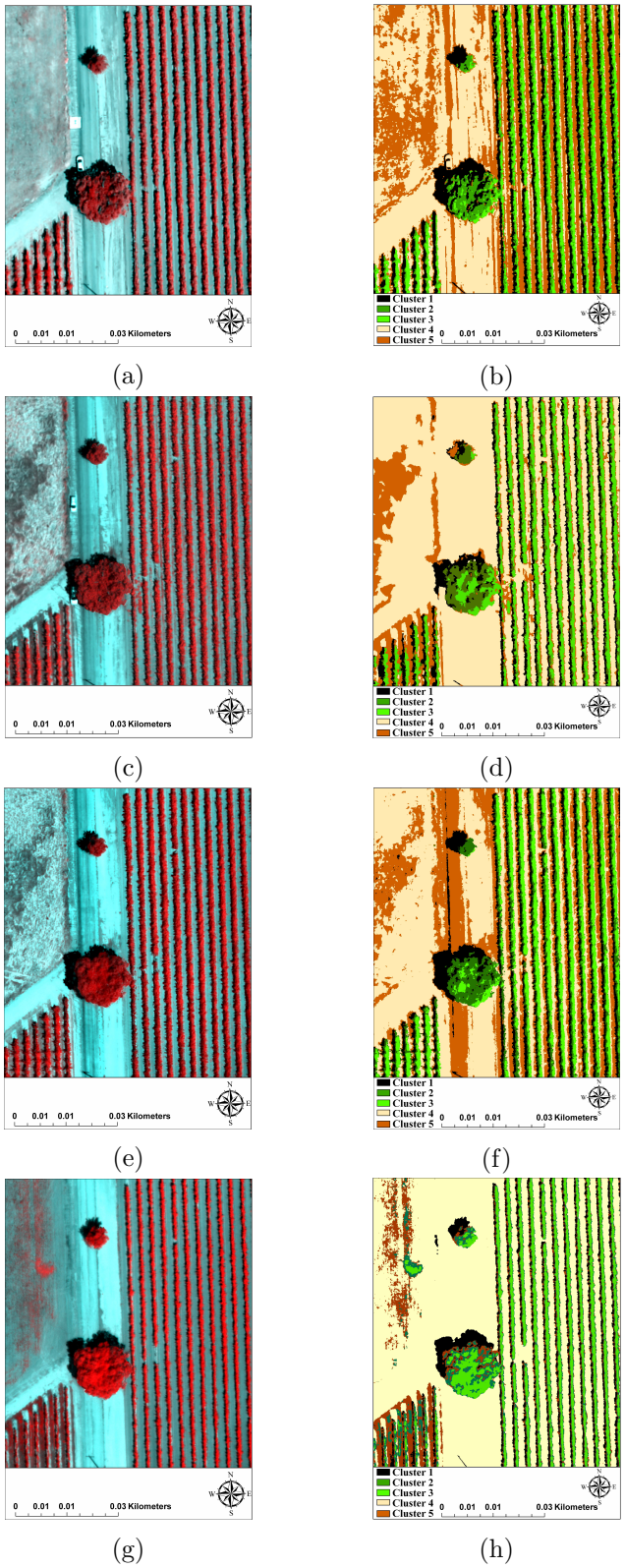

Fig. 2.4: Original UAV false color image subset (left column) and unsupervised classification results (right column) from the vineyard imagery. (a) and (b) correspond to August 2014, (c) and (d) to June 2015, (e) (f) to July 2015 and (g) and (h) to May 2016. Black pixels on the right column represent shaded locations

2.4.2 Supervised Classification

The supervised classification results were obtained using the supervised classification of the ERDAS Imagine Software. Before running this model, a signature file was collected for each of the different targets (vegetation, shadow, bare soil) using the area of interest layers as the training areas and signature editor. Then each pixel was assigned to these discrete signature classes based on a maximum likelihood method. The results of the supervised classification method for shadow detection in images captured by the UAV in August 2014, June 2015, July 2015, and May 2016 are shown in Figure 2.5. From visual inspection, which is the customary approach used to evaluate the performance of different shadow detection methods (Tolt et al. [46], 2011), the performance of this classification for detecting shadows was better than that of the clustering approach, as can be seen by comparing the black pixels in the classified image to the pixels that are obviously in shadows in the false color image. In this method, however, selecting the targets and assigning them to classes was time-consuming.

2.4.3 Index or pixel-based methods

A MATLAB program was written for detecting shadowed pixels using the index-based method. In this program, the average of red and NIR bands was considered as a grayscale image. Then, based on a trial-and-error search, a threshold was applied to the grayscale image to separate shadowed from non-shadowed pixels. The results of the index-based method are illustrated in Figure 2.6. Again, from visual inspection of these figures, the performance of the index-based approach for detecting shadows is better than that of clustering, and somewhat better than that of the classification method. However, as discussed previously, to identify the shadowed pixels with this method, threshold values must be defined to separate the shadowed area from the original version of the image, which requires a trial-and-error approach and a visual histogram analysis.

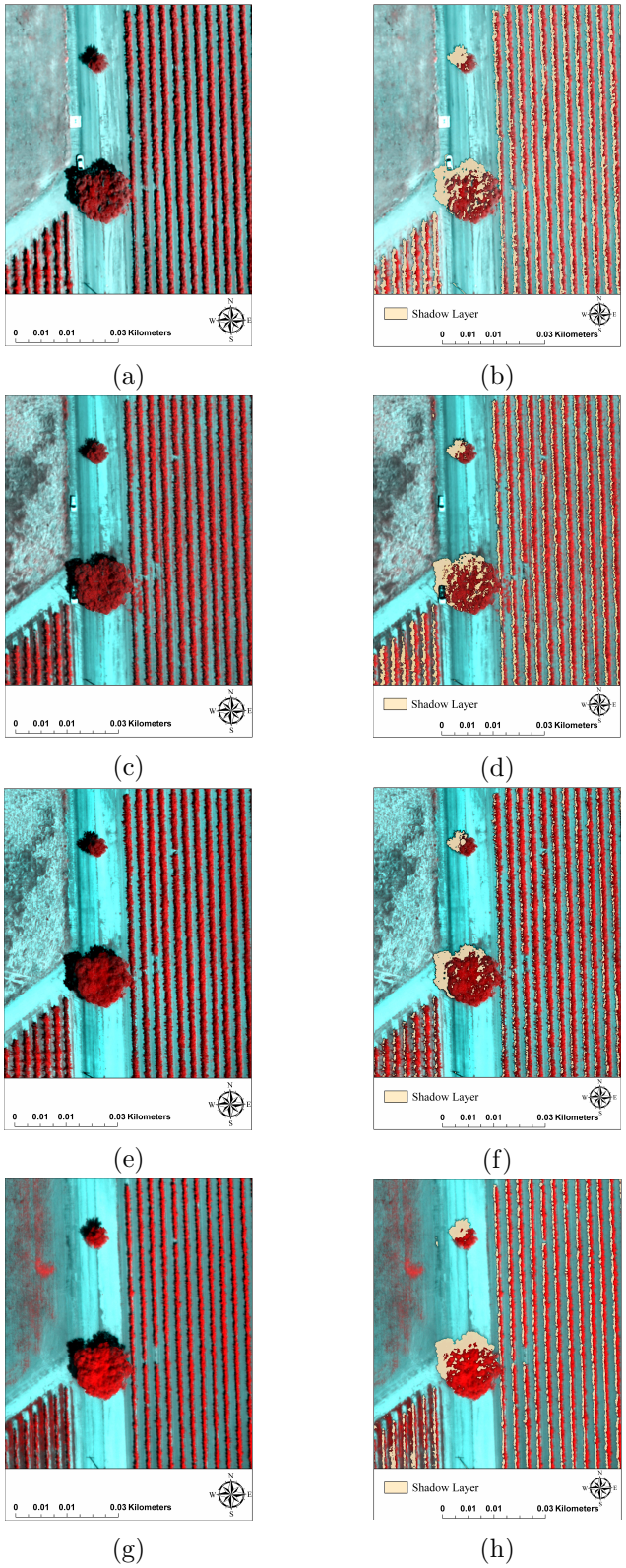

Fig. 2.5: Original UAV false color image subset (left column) and supervised classification results (right column) from the vineyard imagery. (a) and (b) correspond to August 2014, (c) and (d) to June 2015, (e) (f) to July 2015 and (g) and (h) to May 2016. Beige pixels on the right column represent shaded locations

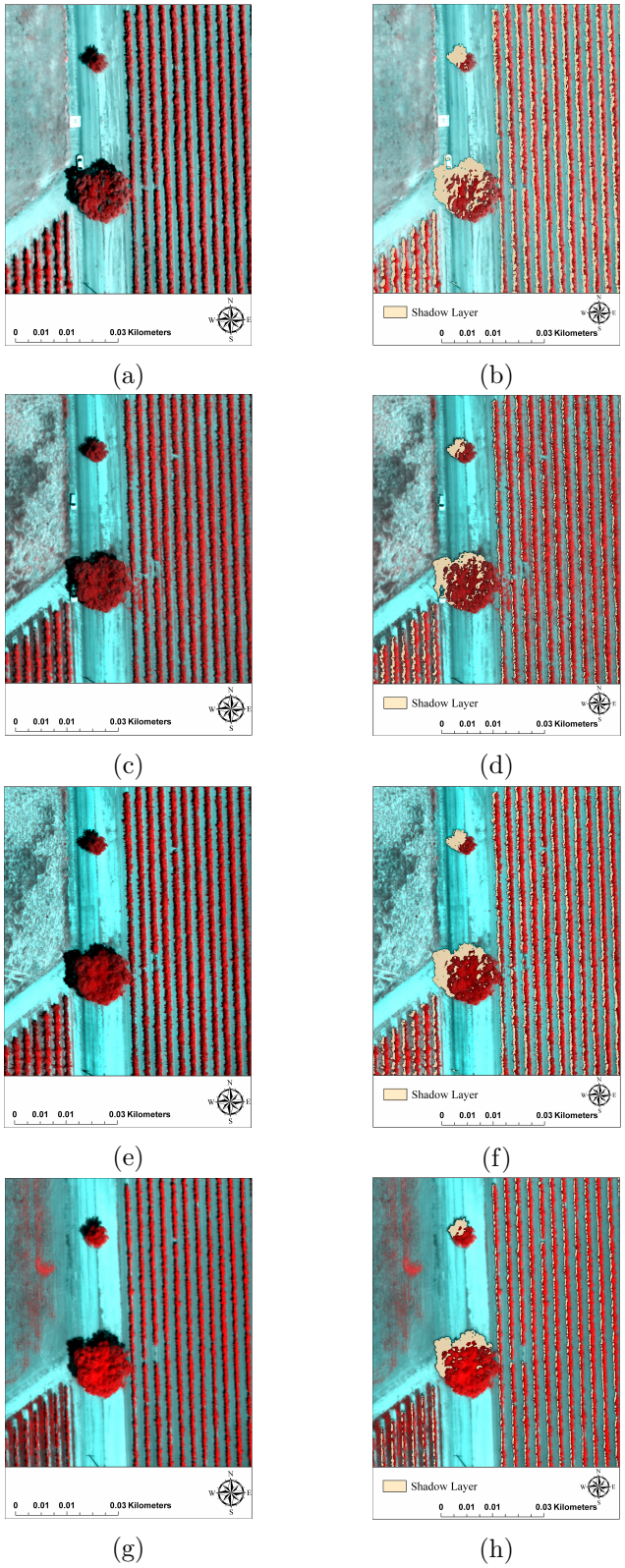

Fig. 2.6: Original UAV false color image subset (left column) and index-based method classification results (right column) from the vineyard imagery. (a) and (b) correspond to August 2014, (c) and (d) to June 2015, (e) (f) to July 2015 and (g) and (h) to May 2016. Beige pixels on the right column represent shaded locations

2.4.4 Physically-based methods

The Hillshade toolbox of ArcGIS was executed to project shadows according to the solar position, using the UAV DSM data. The results of this modeling are shown in Figure 2.7. These images show some uncertainties within the leaf canopy when projecting the shadows using these tools. Although the ArcGIS Hillshade toolbox is independent of the reflectance of each pixel, several factors can affect its accuracy. First, to execute the Hillshade toolbox, the solar position (azimuth and elevation) must be defined. Based upon the latitude and longitude of the image, as well as the time that the image was captured by the UAV, the solar position is defined. Obviously, latitude and longitude are not fixed values over the entire image. Moreover, the duration of the flight is around 20 minutes or less. Therefore, the solar position is not consistent relative to all pixels, so the average solar position was used as input. Moreover, the accuracy of the Hillshade projection critically depends upon the accuracy of the DSM. Similarly to the index-based method, separating the shadowed area from the image required a threshold. Thus, uncertainties for the ArcGIS Hillshade method could be attributed to one or more of the following sources: (1) the accuracy of the DSM, (2) the threshold definition, (3) the use of an average value for the time at which the image was captured by the UAV, and (4) the use of an average value for latitude/longitude.

The Hillshade Toolbox in ArcGIS was executed to project shadows according to solar time and position and DSM. The results of this modeling are shown in Figure 2.7. These images show some errors within the leaf canopy when projecting the shadows using these tools. Although the ArcGIS Hillshade Toolbox is independent of pixel reflectance, the main factor that can affect its performance is related to DSM accuracy. Similar to the index-based method, separating the shadowed area required a threshold selection. One advantage of using this method is the ability to generate the shadow layer in the absence of optical imagery. This is illustrated in Figure 2.8, wherein the diurnal shadow layer for a small part of the vineyard imagery captured by the UAV in July 2015 is simulated from 7:00 a.m. to 8:00 p.m.

2.4.5 Visual Assessment of Shadow Detection Model Performance

Figure 2.9 illustrates the shadow detection differences produced by the different classification methods over an area in the approximate center of the GRAPEX vineyard for imagery captured from the various UAV flights. The performance of the unsupervised and supervised classification approaches and the index-based method varies in this region of the image and serves to contrast their performance in detecting shadows.

From visual inspection of the imagery in Figure 2.9, the performance of these four classification methods in the center portion of the vineyard for the flights in August of 2014 (Figure 2.9.a, Figure 2.9.e, Figure 2.9.i, and Figure 2.9.m) and May of 2016 (Figure 2.9.d, Figure 2.9.h, Figure 2.9.l, and Figure 2.9.p) is acceptable. However, for the flights in June of 2015 (Figure 2.9.b, Figure 2.9.f, Figure 2.9.j, and Figure 2.9.n) and in July of 2015 (Figure 2.9.c, Figure 2.9.g, Figure 2.9.k, and Figure 2.9.o), the physically-based classification methods performed much better than the unsupervised, supervised, and index-based classification methods in the flat region (the center area) where the gray and black pixels can be classified into the shadow class. In addition, the performance of the index-based method is superior to that of the supervised classification method in July 2015 (Figure 2.9.g versus Figure 2.9.k). Thus, although in the flat area, the physically-based and index-based methods performed similarly to each other and much better than the unsupervised, and supervised methods, within the leaf canopy the physically-based method overestimates shadowed pixels (see Figure 2.7 and Figure 2.9.m, Figure 2.9.n, Figure 2.9.o, and Figure 2.9.p).

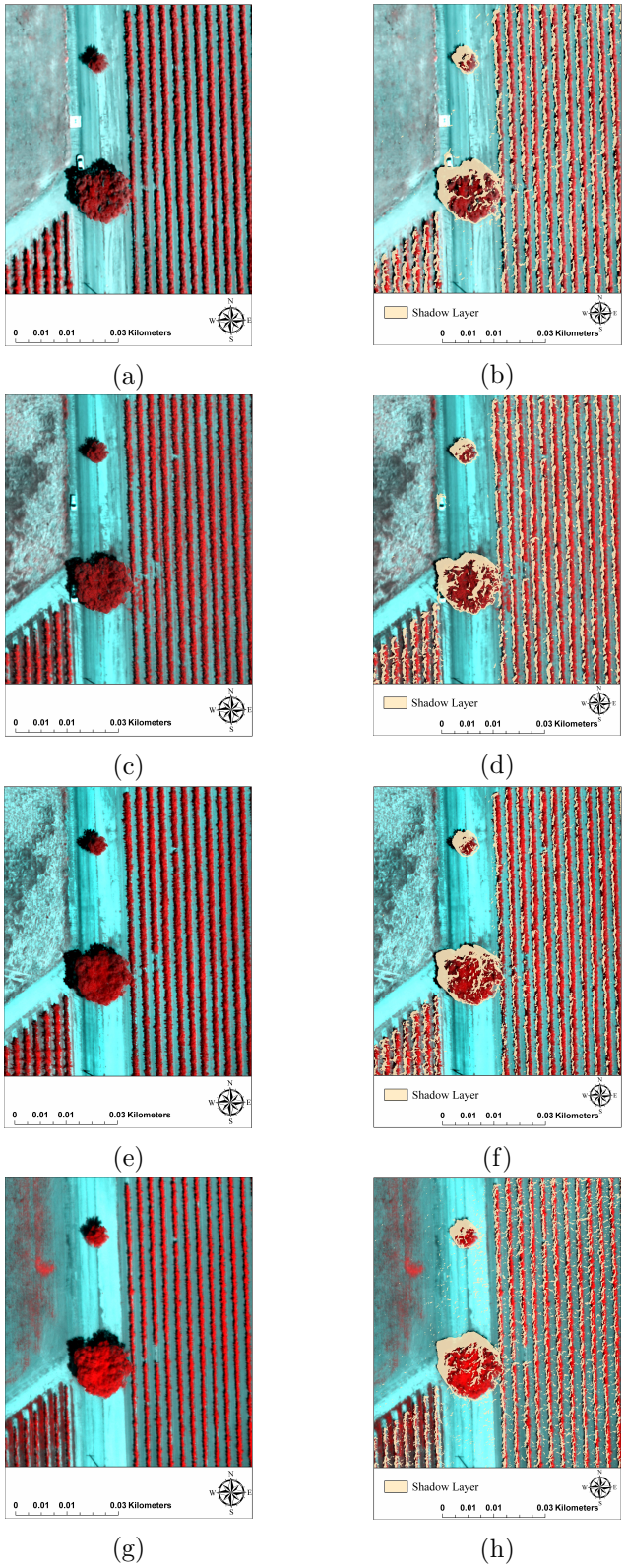

Fig. 2.7: Original UAV false color image subset (left column) and physically-based method classification results (right column) from the vineyard imagery. (a) and (b) correspond to August 2014, (c) and (d) to June 2015, (e) (f) to July 2015 and (g) and (h) to May 2016. Beige pixels on the right column represent shaded locations

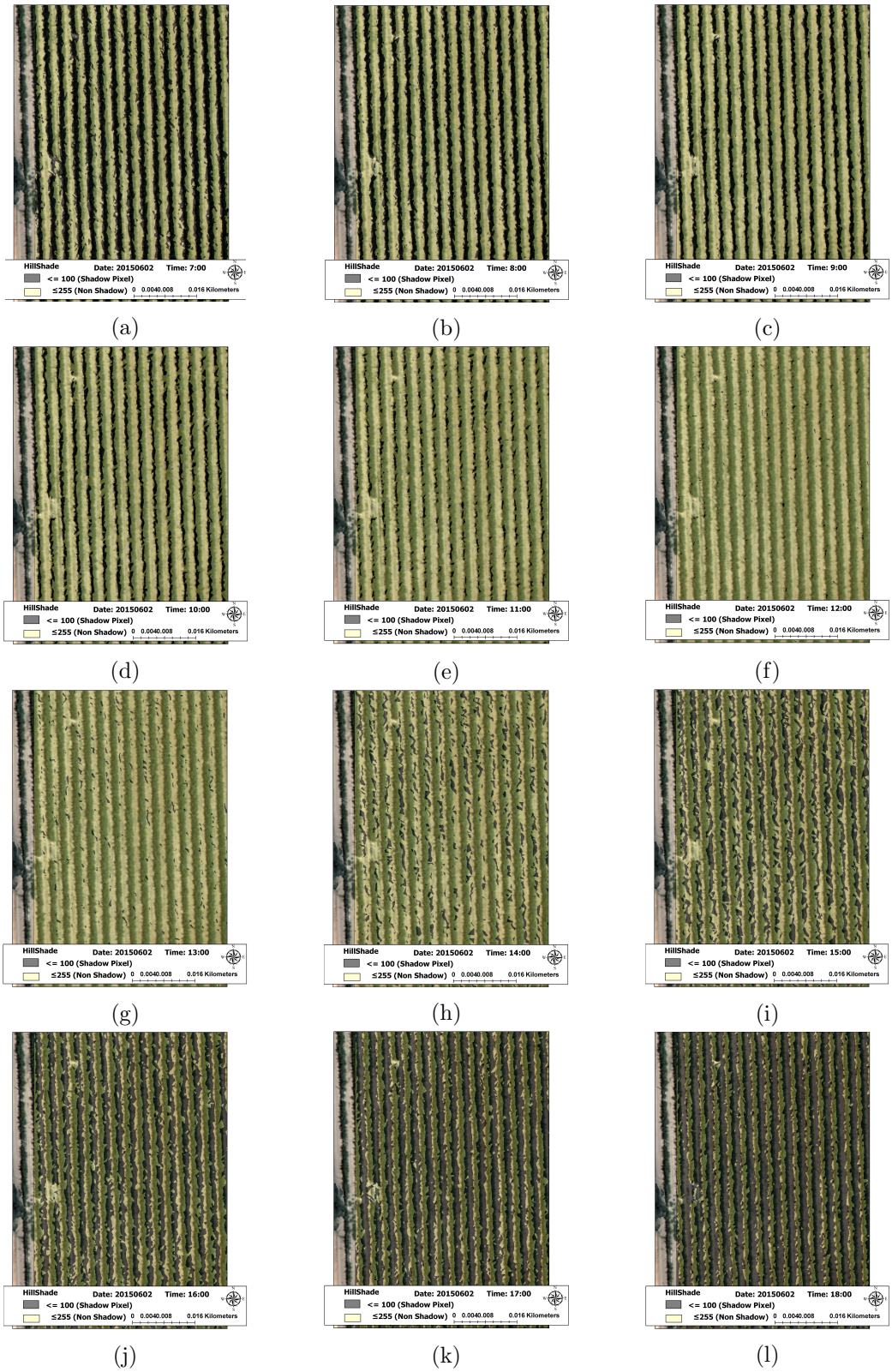

Fig. 2.8: Simulated diurnal shadow pattern shown hourly, from 7:00 a.m. to 8:00 p.m., using the physically based model and shown on the background image captured by the UAV on July 2015 around 11:45 am PST. shadow layer for 7:00 a.m. (a), 8:00 a.m. (b), 9:00 a.m. (c), 10:00 a.m. (d), 11:00 a.m. (e), 12:00 a.m. (f), 1:00 p.m. (g), 2:00 p.m. (h), 3:00 p.m. (i), 4:00 p.m. (j), 5:00 p.m. (k), 6:00 p.m. (l). Dark areas indicate shadow locations.

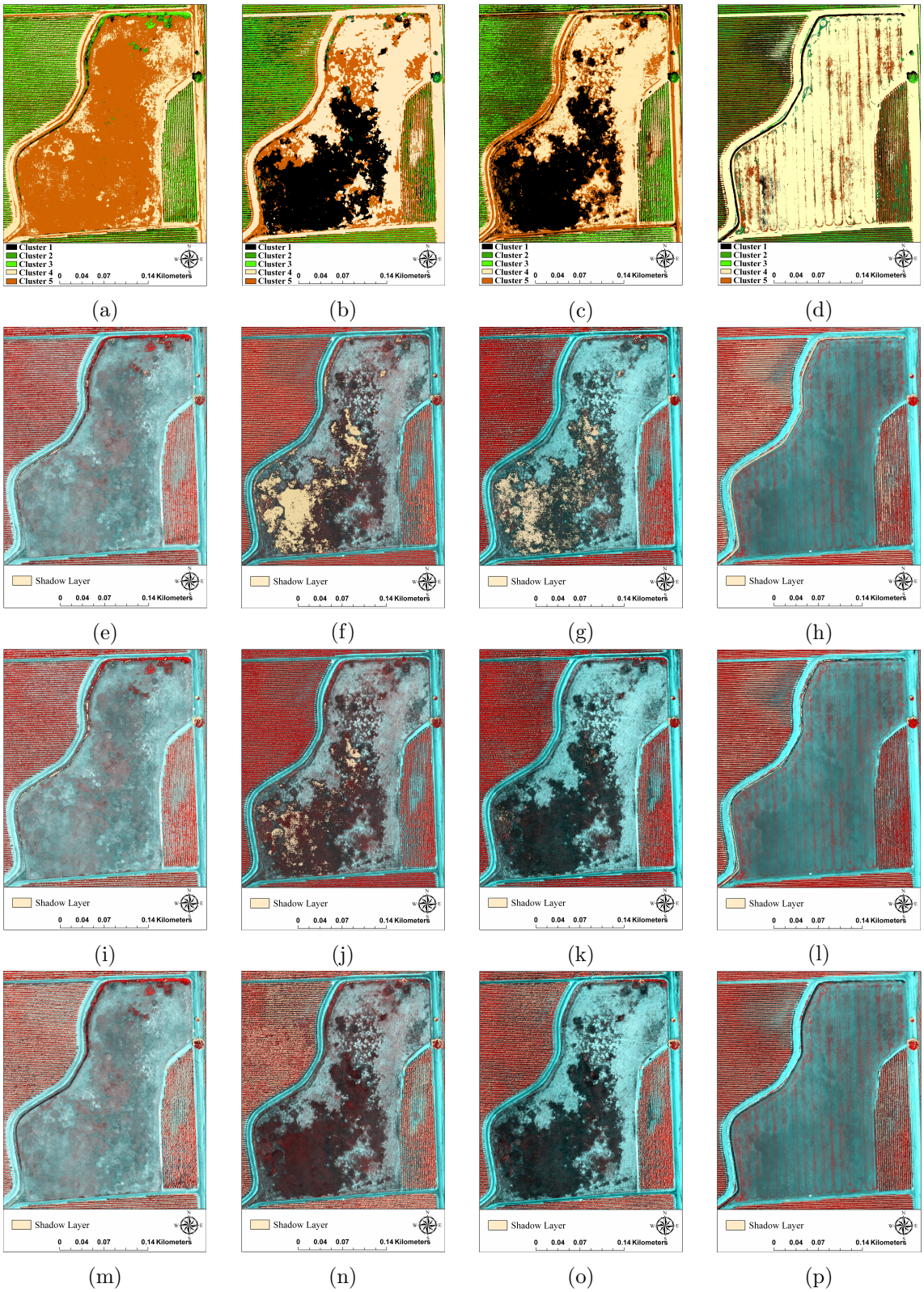

Fig. 2.9: Classification maps of the center portion of the vineyard (original UAV false color image) using unsupervised classification for August of 2014 (a), June of 2015 (b), July of 2015 (c), and May of 2016 (d); using supervised classification for August of 2014 (e), June of 2015 (f), July of 2015 (g), and May of 2016 (h); using the index-based method for August of 2014 (i), June of 2015 (j), July 2015 (k), and May of 2016 (l); using physically-based method for August of 2014 (m), June of 2015 (n), July of 2015 (o), and May of 2016 (p)

2.4.6 Statistical Assessment of Shadow Detection Method Performance

Since shadow detection is a classification task, one approach for evaluating the accuracy of the classification methods is to use the confusion matrix and report the correctness metric (or user's accuracy as described in Congalton, 1991 [8]) shown in (Eq. 2.1). To create a confusion matrix, the images on the left column of Fig 2.5 were manually separated into two categories: (1) shadowed and (2) non-shadowed area. Afterward, each class in the manually extracted method was compared to the corresponding class in each of the classification methods. Ultimately, the correctness metric (Eq. 2.1) was calculated based on the confusion matrix. The results of the confusion matrix, along with the correctness metric, are shown in Table 2.3. According to the correctness metric, the accuracy of the index-based (∼94%) method and the supervised (∼92%) method is higher than for the unsupervised (∼83%) method and the physically-based (∼87%) method. These results confirmed the visual assessment performed in the previous subsection.

$$correctness_{metric} = \frac{TP}{TP + FN} \tag{2.1}$$

in which TP = the numbers of shadow pixels identified correctly, and FN = the numbers of shadow pixels categorized into non-shadow class.

To summarize the advantages and disadvantages of the shadow detection methods, the clustering approach requires no pre-knowledge of the shadow pixel features and the operator only need to specify the number of the clusters, but each cluster contains the information of more than one feature. The performance of the unsupervised classification method is lower than supervised, index-based, and physically-based model, particularly near harvest time (August 2014). However, between bloom and veraison stage of the canopy, the unsupervised classification performance is similar to the physically-based method. The supervised classification method requires pre-knowledge of and sample collection for the desired groups such as vegetation and bare soil and is time-consuming and expensive, especially if there are numerous targets in the imagery. Despite the phenological stages, the accuracy of supervised classification is quite high (more than 90%), but with thriving canopy its performance

improves from 90% (bloom to veraison in May 2016) to 93% (near harvest in August 2014), which is unlike the behavior of the unsupervised classification. In the index-based method, the desired class or target is more sensitive to the threshold that separates the pixels of the desired class from others. Defining an accurate threshold value requires a trial-and-error process that is time-consuming; however, the computational time is generally much less than the unsupervised and supervised classification methods. The accuracy of the index-based method is quite high and even better than the supervised classification method. Like the supervised classification method, the weakest performance of the index-based method occurred when the canopy is not well-developed (bloom to veraison in May 2016), whereas from closing to the harvest time, its accuracy increases (96%). The physically based method requires several inputs, including sun position (azimuth and altitude angles) in the sky, data contained in a DTM, and data from a DSM. The physically based method is independent of the optical imagery and provides an opportunity to model a diurnal pattern of shadow changes over the study area. However, its performance is completely dependent on the quality and spatial resolution of the DEM and DSM data, which is a significant limitation. Its performance classified between the unsupervised and supervised/index-based method. There are no significant changes in the accuracy of the physically-based method with a thriving canopy; however, the supervised, index-based, and physically-based methods all have higher performance in shadow detection during veraison-harvest (June-August) when the canopy may be under stress versus the bloom-veraison.

Table 2.3: Assessment accuracy between different methods and manually extracted method for a small part of the study of area

Date of Flight	Item	Method	Unsupervised		Supervised		Index-Based		Physically-Based	
			Method		Method		Method		Method	
		Classes	Shadow	Non-Shadow	Shadow	Non-Shadow	Shadow	Non-Shadow	Shadow	Non-Shadow
2014, August	Manually Extracted	Shadow	27039	6742	31292	2489	32683	1098	29455	4326
		Non-Shadow	20485	170695	8433	182747	5608	185572	10598	180582
		Total	47524	177437	39725	185236	38291	186670	40053	184908
	Assessment Accuracy (Correctness Metric)		80.6%		93.4%		96.7%		87.2%	
2015, June	Manually Extracted	Shadow	19038	3917	21038	1917	21393	1562	20084	2871
		Non-Shadow	2566	199440	2109	199897	1192	200814	2456	199550
		Total	21604	203357	23147	201814	22585	202376	22540	202421
	Assessment Accuracy (Correctness Metric)		82.9%		91.6%		93.2%		87.5%	
2015, July	Manually Extracted	Shadow	11845	2416	13030	1231	13320	941	12497	1764
		Non-Shadow	3454	207246	2561	208139	1459	209241	2964	207736
		Total	15299	209662	15591	209370	14779	210182	15461	209500
	Assessment Accuracy (Correctness Metric)		83.1%		91.3%		93.4%		87.6%	
2016, May	Manually Extracted	Shadow	18301	3459	19668	2092	20268	1492	18796	2964
		Non-Shadow	5697	197504	3294	199907	2314	200887	4198	199003
		Total	23998	200963	22962	201999	22582	202379	22994	201967
	Assessment Accuracy (Correctness Metric)		84.1%		90.4%		93.1%		86.4%	

2.4.7 Impacts of shadows on NDVI, and ET

The results of evaluating NDVI in both the sunlit and shaded areas of the vineyard leaf canopy are presented here. As discussed in the Methodology Section 2.3, assessing the impact of shadows on NDVI involved extracting two groups of pixels, sunlit and shaded, using two steps. The first step separates the vine canopy pixels from the ground surface and inter-row areas using DTM and DSM data. The second step is the results from the index-based shadow detection method. To test the equality of these two groups, ANOVA was used on the NDVI data from Eq. 2.2. The results of ANOVA for NDVI are presented in Table 2.4. The null hypothesis in the ANOVA is that the mean in both groups (sunlit pixels and shaded pixels) is equal. The results of ANOVA for all images are presented in Table 2.4 (where SS = sum of squares, df = degrees of freedom, MS = mean of squares, F

= f-statistic).

$$H_0 : \mu_1 = \mu_2 \tag{2.2}$$

$$H_1 : \mu_1 \neq \mu_2 \tag{2.3}$$

in which H_0 and H_1 are the null and alternative hypotheses, respectively, and μ_1 and μ_2 are the mean of the two groups (in this study, NDVI on the sunlit and shaded leaf canopy).

Table 2.4: ANOVA results for NDVI for the different flights acquired between 2014 and 2016

Flight Date	Source of Variation	SS	df	MS	F (observed)	P-value	F (critical)
August 2014	Groups	0.038	1	0.038	4.63	0.06	3.84
	Error	8.058	970	0.008			
	Total	8.086	971				
June 2015	Groups	0.328	1	0.32	51.92	0.00	3.84
	Error	6.141	972	0.006			
	Total	6.469	973				
July 2015	Groups	0.043	1	0.04	8.39	0.00	3.84
	Error	6.36	1222	0.005			
	Total	6.40	1223				
May 2016	Groups	0.216	1	0.21	20.58	0.00	3.84
	Error	10.26	974	0.010			
	Total	10.48	975				

As shown in Table 2.4, the F-statistic (observed value) is greater than the critical value for F. Therefore, the null hypothesis is rejected for all images. This means that there is a statistically significant difference between the values of NDVI for the shadowed and non-shadowed pixels within the vine canopy. The histograms shown in Figure 2.10 further illustrate the difference in the distribution of NDVI values for the UAV flights conducted in 2014, 2015, and 2016.

A close examination of the distribution range of the shadowed pixels as presented in Figure 2.10, indicates that it is smaller than that of sunlit pixels. In addition, the average values of NDVI in the sunlit pixels is higher than those in the shadowed pixels. This means that ignoring the effect of shadows on NDVI can lead to biased results and conclusions when

using this variable. The LAI is a critical input to land surface models for ET estimation that can be calculated based on NDVI. Hence shadow effects over this biophysical variable will cause error if the models ignore or fail to compensate for the bias on the LAI estimates. For example, in the two-source energy balance (TSEB) model developed by Norman et al. (1995) [31], the radiometric temperature sensed at the satellite is partitioned into canopy temperature (T_c) and soil temperature (T_s) components using Eq. 2.4.

$$T_R = [f_c(\phi)T_c^4 + (1 - f_c(\phi))T_s^4]^{0.25} \tag{2.4}$$

in which $f_c(\phi)$ is the fraction of vegetation observed by the thermal sensor with view angle ϕ and can be calculated using a Eq. 2.5 proposed by Campbell and Norman (1998). [5].

$$f_c(\phi) = 1 - \exp \frac{-0.5\Omega(\phi)LAI}{\cos \phi} \tag{2.5}$$

in which Ω is a clumping factor, and LAI is estimated in this study using an empirical NDVI-LAI relation (Anderson et al. 2004 [3]) proposed by Fuentes et al. 2014 [12] for vineyards (Eq. 2.6).

$$LAI = 4.4 \times NDVI \tag{2.6}$$

Satellite and also UAV imagery provide a single observation of (T_R) per pixel. Therefore, to partition T_R using Eq. 2.4, there is still two unknown variables, T_c and T_s. One approach to solve the equation is to estimate an initial value for T_c considering plants are losing water at a potential rate defined by Priestley and Taylor (1972) [35] (Eq. 2.7).

$$LE_c = \alpha f_g \frac{S}{S + \gamma} Rn_c \tag{2.7}$$

in which α = the Priestley-Taylor coefficient (default value is 1.26), f_g = fraction of vegetation that is green, S = the slope of the saturation vapor pressure curve versus temperature, and γ = psychrometric constant. Rn_s is the net radiation at the soil surface and Rn_c is the

net radiation at the canopy layer estimated based on irradiance, LAI and surface spectra and temperature (Kustas et al. 1999 [19], Campbell et al. 1998 [5])

By subtracting LE_c from Rn_c, the sensible heat flux of the canopy (H_c) is achieved. Now, we are able to have an initial estimate of (T_c) using Eq. 2.8 and solve Eq. 2.4 with a single unknown variable (T_s).

$$H_c = Rn_c - LE_c = \rho\, c_p\, \frac{T_c - T_0}{R_x} \tag{2.8}$$

in which ρc_p= volumetric heat capacity of air; T_0= aerodynamic temperature at the canopy interface, and R_x= bulk canopy resistance to heat transport. In this step, if the soil latent heat flux (LE_s) calculated based on T_s is non-negative, a solution is found. If not, LE_c decreases using an incremental decrease in α, which leads to increasing T_c and decreasing T_s until a non-negative solution for LE_s is found (Norman et al. (1995) [31] and Kustas and Norman, 1999 [19]). In the case of vineyards, the more sophisticated radiation and wind extinction algorithm in the TSEB model developed by Parry et al. 2017 (this issue [33]) and Nieto et al. 2017 (this issue [30]) requires several additional inputs, including LAI.

To evaluate the impact of shadows on energy balance components, TSEB was applied considering two scenarios (with and without masking shadows), one in which canopy parameters (LAI, canopy width) are estimated from the original VNIR images, and a second in which the canopy parameters are estimated with the image after masking out the shadows. Moreover, in order to preserve the assumptions in TSEB related to turbulent transport, TSEB was run by aggregating the UAV imagery to 3.6m. The impact on the magnitude of the energy balance components and their distribution is illustrated in Figures 2.11-2.14 for the UAV image of August 2014. These figures show the spatial absolute differences of fluxes as well as histogram and relative cumulative frequency of fluxes for both scenarios (with and without masking shadows). The histograms show a clear shift in soil heat flux (G) indicating that the peak is moved to the higher values when shadows are involved. Since the NDVI-derived LAI present smaller values when shaded pixels are involved, LAI yields lower values and therefore net radiation reaching the ground (Rn_s) is increased. As

G is a ratio of (Rn_s) in TSEB, including the shadows in NDVI-LAI calculation led to an increase of G. For the same scenario, the peak of sensible heat flux (H) and Rn are shifted to smaller values. Increasing G and decreasing Rn account for shadows, and indicate that the available energy (Rn-G) is decreasing. As shown in Figure 2.13, H decreased slightly due to slight changes in the soil temperature and canopy temperature values derived from a lower LAI in involving shadows scenario. For the latent heat flux (LE) considering the shadows results in a slight shift in the LE distribution to larger values and a greater number of LE values at the centroid of the distribution.

An additional evaluation of the shadow impact on crop water stress using Bowen Ratio was performed as shown in Figures 2.15 and 2.16. These figures indicate that ignoring shadows led to larger water stress areas, particularly in the southern section of the field. Moreover, the histograms show there are some differences (approximately 6%) in the Bowen ratio calculated by involving versus ignoring the shadows.

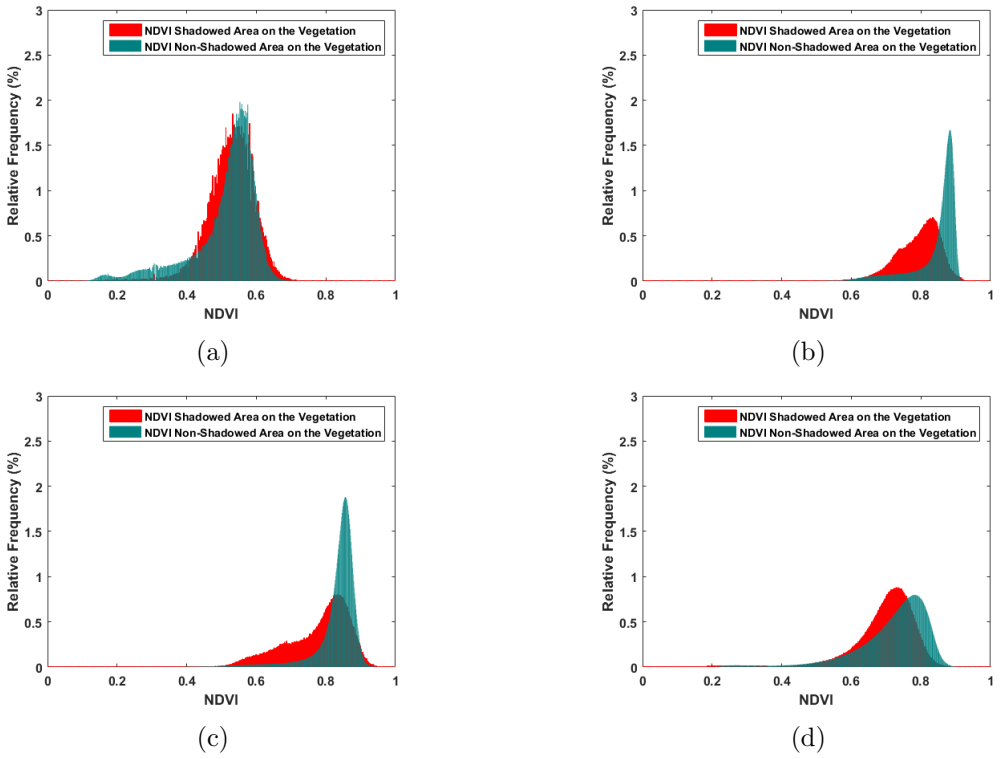

Fig. 2.10: The NDVI histograms for the shadowed and sunlit pixels for the August 2014 imagery (a), the NDVI histograms for the shadowed and sunlit pixels for the June 2015 imagery (b), the NDVI histograms for the shadowed and sunlit pixels for the July 2015 imagery (c), the NDVI histograms for the shadowed and sunlit pixels for the May 2016 imagery (d).

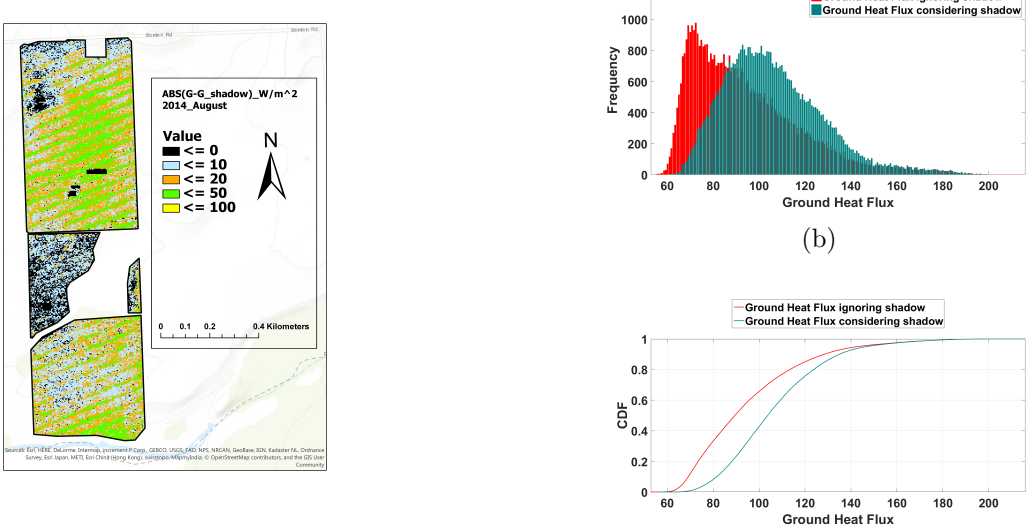

(a) (b) (c)

Fig. 2.11: Flight, August 2014; the spatial absolute differences of soil heat flux considering shadows and ignoring shadows (a), histogram of soil heat flux considering/ignoring shadows (b), CDF of soil heat flux considering/ignoring shadows (c).

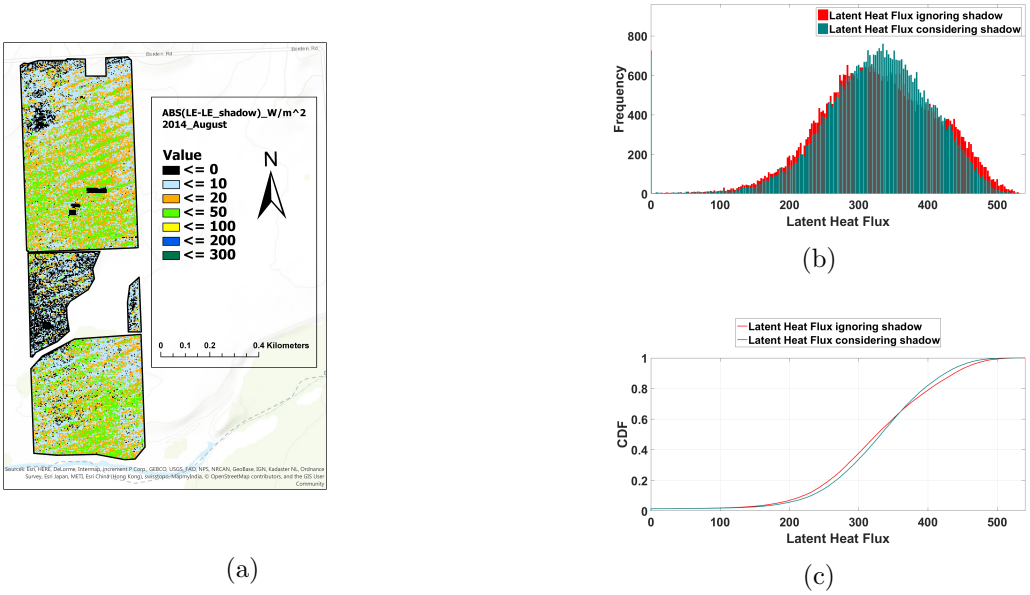

(a) (b) (c)

Fig. 2.12: Flight, August 2014; the spatial absolute differences of latent heat flux considering shadows and ignoring shadows (a), histogram of latent heat flux considering/ignoring shadows (b), CDF of latent heat flux considering/ignoring shadows (c).

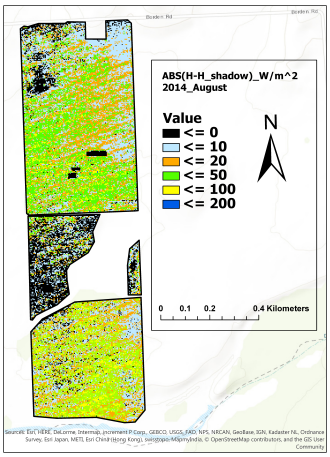

(a)

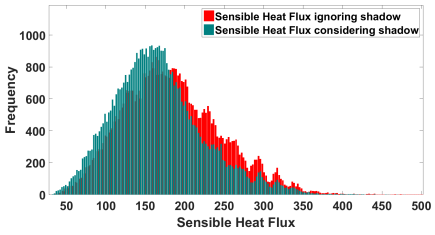

(b)

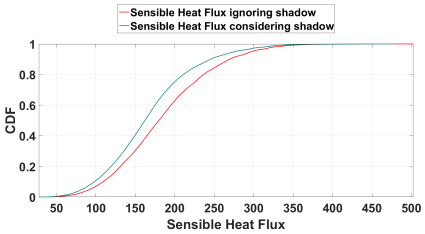

(c)

Fig. 2.13: Flight, August 2014; the spatial absolute differences of sensible heat flux considering shadows and ignoring shadows (a), histogram of sensible heat flux considering/ignoring shadows (b), CDF of sensible heat flux considering/ignoring shadows (c).

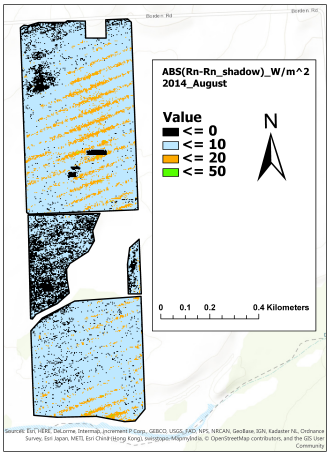

(a)

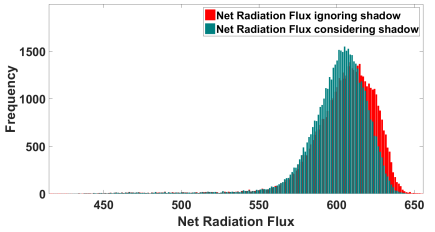

(b)

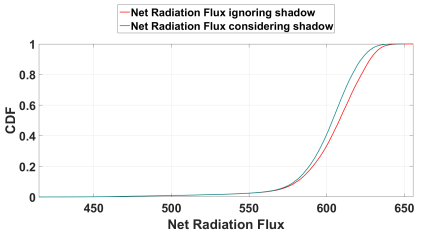

(c)

Fig. 2.14: Flight, August 2014; the spatial absolute differences of net radiation flux considering shadows and ignoring shadows (a), histogram of net radiation considering/ignoring shadows (b), CDF of net radiation flux considering/ignoring shadows (c).

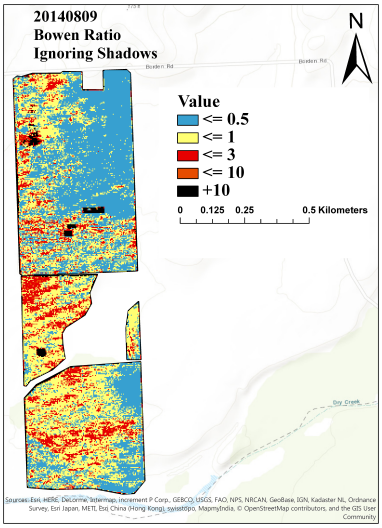

(a)]

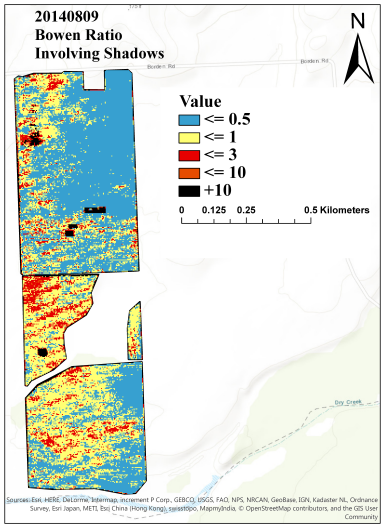

(b)

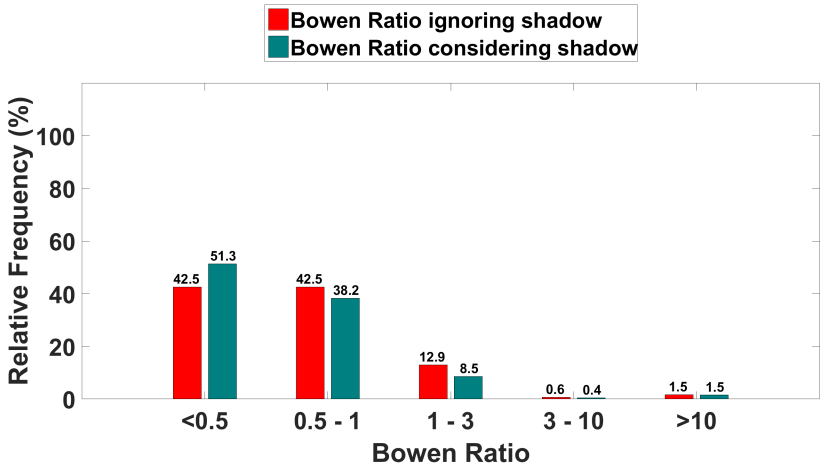

(c)

Fig. 2.15: Flight, August 2014; Bowen Ratio ignoring shadows (a), Bowen Ratio involving shadows (b), Histogram of Bowen Ratio ignoring/involving shadows (c).

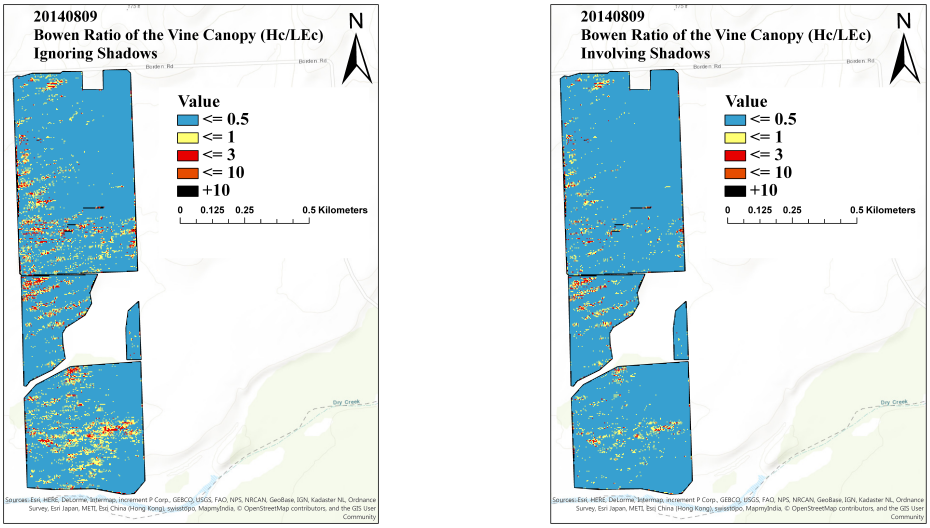

(a)] (b)

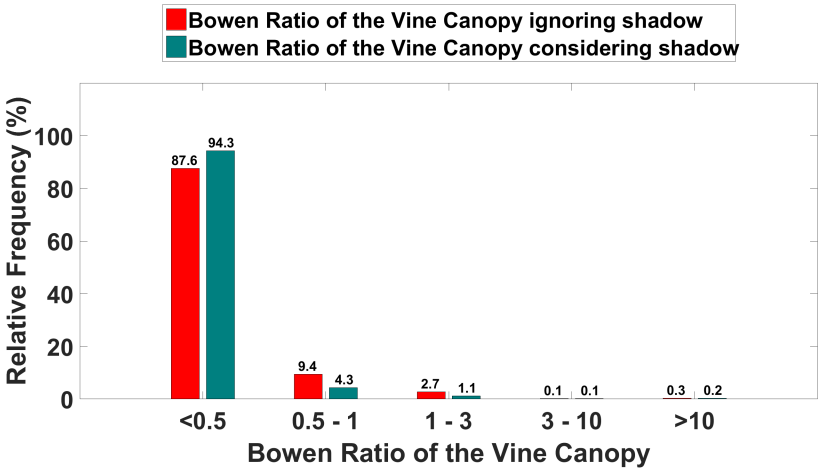

(c)

Fig. 2.16: Flight, August 2014; (a) Bowen Ratio of the vine canopy ignoring shadows, (b) Bowen Ratio of the vine canopy involving shadows, (c) Histogram of Bowen Ratio of the vine canopy ignoring/involving shadows.

The ANOVA test was used to evaluate whether there was a significant difference in the fluxes computed by TSEB when accounting versus ignoring shadows. The results of ANOVA for those fluxes are presented in Table 2.5 to 2.8. The ANOVA results indicate that there is a statistically significant difference in ignoring versus accounting for shading for G and, for

most of the flights, for Rn. However, in only half the flights does the ANOVA indicate that accounting for shadows makes a difference in the output of H (August, 2014 and June, 2015 flights) and in only one of the flights for LE (May, 2016 flight). Although ANOVA does not indicate a significant difference for LE in 2014 and 2015 flights, it is important to note that ANOVA is used for testing the equality of the means of the distributions and consequently does not evaluate differences in the flux distributions between ignoring and accounting for shadows. For this reason, the spatial differences in the fluxes shown in Figures 2.11 - 2.16 to indicate the areas of the vineyard where significant discrepancies in fluxes and stress (i.e., Bowen ratio) can exist.

Table 2.5: ANOVA results for G flux for the different flights acquired between 2014 and 2016

Parameter	Source of Variation	SS	df	MS	F (observed)	P-value	F (critical)
August 2014 (G)	Groups	33484.5	1	33484.5	60.73	0	3.84
	Error	550286.6	998	551.4			
	Total	583771.1	999				
June 2015 (G)	Groups	7064.16	1	7064.16	4.01	0.0456	3.84
	Error	1787208.13	1014	1762.53			
	Total	1794272.25	1015				
July 2015 (G)	Groups	24355.7	1	24355.7	23.14	0	3.84
	Error	1063052.4	1010	1052.5			
	Total	1087408	1011				
May 2016 (G)	Groups	13811.9	1	13811.9	13.26	0.0003	3.84
	Error	1035735.6	994	1042			
	Total	1049547.5	995				

2.5 Conclusions

Shadows are an inherent component of high-resolution RS imagery. If ignored, they can cause bias in products derived from RS data that are intended for monitoring plant and soil conditions. In this study, four different shadow detection methods developed for satellite imagery were applied to very-high-resolution images captured by a UAV at various times over a GRAPEX vineyard and evaluated for accuracy. These methods were (a) unsupervised classification or clustering, (b) supervised classification, (c) index-based methods, and (d)

Table 2.6: ANOVA results for H flux for the different flights acquired between 2014 and 2016

Parameter	Source of Variation	SS	df	MS	F (observed)	P-value	F (critical)
August 2014 (H)	Groups	77736.5	1	77736.5	21.82	0	3.84
	Error	3519222.3	988	3562			
	Total	3596958.8	989				
June 2015 (H)	Groups	58627.9	1	58627.9	3.96	0.0467	3.84
	Error	14544242	984	14781.5			
	Total	14602869	985				
July 2015 (H)	Groups	26698.01	1	26698	1.33	0.2499	3.84
	Error	20223718	1004	20143.1			
	Total	20250416	1005				
May 2016 (H)	Groups	2157.86	1	2157.86	0.82	0.3656	3.84
	Error	2602439	988	2634.05			
	Total	2604596.75	989				

Table 2.7: ANOVA results for LE flux for the different flights acquired between 2014 and 2016

Parameter	Source of Variation	SS	df	MS	F (observed)	P-value	F (critical)
August 2014 (LE)	Groups	2280.2	1	2280.2	0.38	0	3.84
	Error	6000867	998	6012.89			
	Total	6003147	999				
June 2015 (LE)	Groups	14609.2	1	14609.2	0.59	0.4436	3.84
	Error	24472706	984	24870.6			
	Total	24487316	985				
July 2015 (LE)	Groups	4889.28	1	4889.3	0.16	0.6854	3.84
	Error	29661146	996	29780.3			
	Total	29666036	997				
May 2016 (LE)	Groups	11763.3	1	11763.3	4.07	0.0439	3.84
	Error	2889741.5	1000	2889.7			
	Total	2901504.2	1001				

physically-based methods. The results from visual and statistical assessments indicated that the accuracy of the supervised classification method and the index-based method were generally comparable to one another, and superior to the other two. In terms of phenological stage, the performance of the supervised and index-based methods increases with growing canopy (from bloom stage to harvest stage, when the canopy may be under stress) whereas the accuracy of the unsupervised classification decreases during late growing stage. However, the performance of the physically based model was not sensitive to the growth stages of the grapevine canopy. Furthermore, an ANOVA assessment between sunlit or shaded canopy

Table 2.8: ANOVA results for Rn flux for the different flights acquired between 2014 and 2016

Parameter	Source of Variation	SS	df	MS	F (observed)	P-value	F (critical)
August 2014 (Rn)	Groups	4022.5	1	4022.48	8.13	0.0044	3.84
	Error	482734.6	976	494.61			
	Total	486757.1	977				
June 2015 (Rn)	Groups	745.291	1	745.29	0.63	0.4261	3.84
	Error	1140210.55	970	1175.47			
	Total	1140955.5	971				
July 2015 (Rn)	Groups	4884.997	1	4885	4.06	0.0441	3.84
	Error	1223456.25	1018	1201.82			
	Total	1228341.25	1019				
May 2016 (Rn)	Groups	1407.9	1	1407.9	3.99	0.0462	3.84
	Error	344778	976	353.26			
	Total	346186.5	977				

indicates statistical differences between the two groups for NDVI. Finally, the impacts of shadows on ET estimation and other fluxes using energy balance models and high-resolution RS data is examined. According to the TSEB model outputs, G increased, while Rn, H, and available energy (Rn-G) decreased in conditions involving shadows. However, in most cases the overall effect on LE was minimal, although differences were significant in certain areas in the vineyard. This implies that high-resolution models of ET and biophysical parameters should consider the impact of shadowed areas that could cause significant bias in modeled ET.

The analyses presented, together with the emerging ability to employ UAV-based remote sensing technologies to acquire high-resolution, scientific-grade spectral data in three dimensions (high-resolution DTM and DSM data, and point cloud data), also point to the possibility of successfully applying high-resolution energy balance modeling techniques to acquire plant-scale estimates of ET and plant stress. Such information could be potentially exploited by growers to manage irrigation deliveries in differential patterns within individual fields while, at the same time, conserving water and reducing management costs. Additional research is required to prove this capability has utility and economic return for high-value crops, such as wine grapes. Future steps based on this work involve the diurnal modeling of shadows for quantification of their impact on energy balance model results, as

well as incorporation of shadow conditions into energy balance algorithms.

Bibliography

[1] http://www.aggieair.usu.edu/

[2] AgiSoft, L. L. C., and Russia St Petersburg. "Agisoft photoscan." Professional Edition (2016).

[3] Anderson, M. C., Neale, C. M. U., Li, F., Norman, J. M., Kustas, W. P., Jayanthi, H., and Chavez, J. (2004). "Upscaling ground observations of vegetation water content, canopy height, and leaf area index during SMEX02 using aircraft and Landsat imagery." Remote Sensing of Environment, 92, 447-464.

[4] Bethsda, M. D. (1997). "Manual of Photographic Interpretation." 2nd edition, American Society Photogrammetry and remote sensing (ASPRS).

[5] Campbell, G. S. and Norman, J. M. (1998). "An introduction to environmental biophysics", Springer-Verlag, New York.

[6] Carlson, T. N., and Ripley, D. A. (1997). "On the relation between NDVI, fractional vegetation cover, and leaf area index." Remote Sensing of Environment, 62(3), 241-252.

[7] Choi, H., and Bindschadler, R. (2004). "Cloud detection in Landsat imagery of ice sheets using shadow matching technique and automatic normalized difference snow index threshold value decision." Remote Sensing of Environment, 91(2), 237-242.

[8] Congalton, R.G. (1991). "A review of assessing the accuracy of classifications of remotely sensed data." Remote Sensing of Environment, 37(1), 35-46.

[9] Cook, B. D., L. W. Corp, R. F. Nelson, E. M. Middleton, D. C. Morton, J. T. McCorkel, J. G. Masek, K. J. Ranson, V. Ly, and P. M. Montesano. (2013). "NASA Goddard's Lidar, Hyperspectral and Thermal (G-LiHT) airborne imager." Remote Sensing 5:4045-4066, doi:10.3390/rs5084045

[10] Crowther, B.G. (1992). "Radiometric calibration of multispectral video imagery." (Doctoral dissertation, Utah State University. Department of biological and Irrigation Engineering).

[11] Elarab, M., Ticlavilca, A.M., Torres-Rua, A.F., Maslova, I., and McKee, M (2015). "Estimating chlorophyll with thermal and broadband multispectral high resolution imagery from an unmanned aerial system using relevance vector machines for precision agriculture." International Journal of Applied Earth Observation and Geoinformation, 43, 32-42.

[12] Fuentes, S., Poblete-Echeverría, C., Ortega-Farias, S., Tyerman, S., and De Bei, R. (2014). "Automated estimation of leaf area index from grapevine canopies using cover photography video and computational analysis methods." Australian Journal of Grape Wine Research. 20(3), 465-473.

[13] Gonzalez, R.C., Woods, R.E., and Eddins, S.L. (2004). "Digital Image Processing Using MATLAB.", Prentice Hall.

[14] Hsieh, Y. T., Wu, S. T., Chen, C. T., and Chen, J. C. (2016). "Analyzing spectral characteristics of shadow area from ADS-40 high radiometric resolution aerial images." International Archives of the Photogrammetry, Remote Sensing and Spatial Information Sciences, XLI-B7, 223–227.

[15] Huang, J., and Chen, C. (2009a). "A physical approach to moving cast shadow detection." IEEE International Conference on Acoustics, Speech and Signal Processing, 769-772.

[16] Huang, J., and Chen, C. (2009b). "Moving cast shadow detection using physics-based features." IEEE Conference on Computer Vision and Pattern Recognition, 2310-2317.

[17] Kiran, T. S. (2016). "A framework in shadow detection and compensation of images." DJ Journal of Advances in Electronics and Communication Engineering, 2(3), 1-9.

[18] Kumar, P., Sengupta, K., Lee, A. (2002). "A comparative study of different color spaces for foreground and shadow detection for traffic monitoring system." The IEEE 5th International Conference on Intelligent Transportation Systems, 100–105.

[19] Kustas, W.P., Norman, J.M. (1999). "Evaluation of soil and vegetation heat flux predictions using a simple two-source model with radiometric temperatures for partial canopy cover." Agricultural and Forest Meteorology 94(1),13–29, DOI 10.1016/S0168-1923(99)00005-2

[20] Kustas, W.P., Anderson, M.C., Alfieri, J.G., Knipper, K., Torres-Rua, A., Parry, C.K., Nieto, H., Agam, N., White, A., Gao, F., McKee, L., Prueger, J.H., Hipps, L.E., Los, S., Alsina, M., Sanchez, L., Sams, B., Dokoozlian, N., McKee, M., Jones, S., Yang, Y., Wilson, T.G., Lei, F., McElrone, A., Heitman, J.L., Howard, A.M., Post, K., Melton, F., and Hain, C. "The Grape Remote sensing Atmospheric Profile and Evapotranspiration eXperiment (GRAPEX)." Bulletin of the American Meteorological Society, https://doi.org/10.1175/BAMS-D-16-0244.1

[21] https://www.labsphere.com/

[22] Leblon, B., Gallant, L., and Charland, S. D. (1996a). "Shadowing effects on SPOT-HRV and high spectral resolution reflectance in Christmas tree plantation." International of Journal of Remote Sensing, 17(2), 277-289.

[23] Leblon, B., Gallant, L., and Grandberg, H. (1996b). "Effects of shadowing types on ground-measured visible and near-infrared shadow reflectance." Remote Sensing of Environment, 58(3), 322–328.

[24] Lillesand, T. M., and Kiefer, R. W. (2000). "Remote Sensing and Image Interpretation." 4th edition. New York, Wiley.

[25] http://www.technologyreview.com/lists/technologies/2014/

[26] Miura, T., and Huete, A.R. (2009). "Performance of three reflectance calibration methods for airborne hyperspectral spectrometer data." Sensors. 9(2), 794–813.

[27] MosaicMill Oy, (2009). "EnsoMOSAIC Image Processing User's Guide." Version 7.3. Mosaic Mill Ltd. Finland.

[28] Neale, C.M., and Crowther, B.G., (1994). "An airborne multispectral video/radiometer remote sensing system: development and calibration." Remote Sensing of Environment. 49(3), 187–194.

[29] Nemani, R. R., and Running, S. W. (1989). "Estimation of regional surface resistance to evapotranspiration from NDVI and thermal IR AVHRR data." Journal of Applied Meteorology, 28(4), 276-284.

[30] Nieto, H., Kustas, W., Torres-Rua, A., Alfieri, J., Gao, F., Anderson, M., White, W. A., Song, L., Mar Alsina, M., Prueger, J., McKee, M., Elarab, M., and McKee, L. (2017). "Evaluation of TSEB turbulent fluxes using different methods for the retrieval of soil and canopy component temperatures from UAV thermal and multispectral imagery." Irrigation Science, In press.

[31] Norman, J. M., Kustas, W. P., and Humes, K. S. (1995). "Source approach for estimating soil and vegetation energy fluxes in observations of directional radiometric surface temperature." Agricultural and Forest Meteorology, 77, 263-293.

[32] Ortega-Farías, S., Ortega-Salazar, S., Poblete, T., Kilic, A., Allen, R., Poblete-Echeverría, C., Ahumada-Orellana, L.,Zuñiga, M., and Sepúlveda, D. (2016) "Estimation of energy balance components over a drip-irrigated olive orchard using thermal and multispectral cameras placed on a helicopter-based unmanned aerial vehicle (uav)," Remote Sensing, 8(8).

[33] Parry, C., Nieto, H., Guillevic, P., Agam, N., Kustas, B., Alfieri, J., McKee, L. and McElrone, A.J. "An intercomparison of radiation partitioning models in vineyard row structured canopies", Irrigation Science, In press.

[34] Poblete, T., Ortega-Farías, S., and Ryu., D. (2018). "Automatic Coregistration Algorithm to Remove Canopy Shaded Pixels in UAV-Borne Thermal Images to Improve the

Estimation of Crop Water Stress Index of a Drip-Irrigated Cabernet Sauvignon Vineyard." Sensors, 18(2), 397.

[35] Priestley, C.H.B., Taylor, R.J. (1972). "On the assessment of surface heat flux and evaporation using large-scale parameters." Monthly Weather Review, 100, 81–92.

[36] Qiao, X., Yuan, D, and Li, H. (2017). "Urban shadow detection and classification using hyperspectral image." Journal of the Indian Society of Remote Sensing, doi: 10.1007/s12524-016-0649-3.

[37] Ranson, K. J., and Daughtry, C. S. T. (1987). "Scene shadow effects on multispectral response." IEEE Transactions on Geoscience and Remote Sensing, 25(4), 502-509.

[38] Rosin, P.L. and Ellis, T. (1995) "Image difference threshold strategies and shadow detection." Proceedings of the 1995 British Conference on Machine Vision, 1, 347–356.

[39] Ross, J. (1981). "The radiation regime and architecture of plants. In: Lieth, H. (Ed.)", Tasks for Vegetation Sciences 3. Dr. W. Junk, The Hague, Netherlands.

[40] Sandnes, F. E. (2011). "Determining the geographical location of image scenes based object shadow lengths." Journal of Signal Processing systems, 65(1), 35-47.

[41] Sanin, A., Sanderson, C., and Lovell, B. (2012). "Shadow detection: A survey and comparative evaluation of recent methods." Pattern Recognition, 45(4), 1684-1689.

[42] Scanlan, J.M., Chabries, D.M., Christiansen, R., (1990). "A shadow detection and removal algorithm for 2-d images." Proceeding IEEE International Conference on Acoustics, Speech, and Signal Processing (ICASSP), 2057-2060.

[43] Shiting, W., and Hong, Z. (2013) "Clustering-based shadow edge detection in a single color image." International Conference on Mechatronic Sciences, Electric Engineering and Computer (MEC), 1038-1041.

[44] Siala, K., Chakchouk, M., Besbes, O., and Chaieb, F. (2004) "Moving Shadow Detection with Support Vector Domain Description in the Color Ratios Space." In Proceedings of the 17th IEEE International Conference on Pattern Recognition, 384–387.

[45] Sirmacek, B., and Unsalan, C. (2008). "Building detection from aerial images using invariant color features and shadow information." Proceedings of the 23rd International Symposium on Computer and Information Sciences (ISCIS 2008), Istanbul, Turkey, October 27-29, 1-5.

[46] Tolt, G., Shimoni, M., and Ahlberg, J., (2011). "A shadow detection method for remote sensing images using VHR hyperspectral and LIDAR data." Proceeding. Geoscience and Remote Sensing Symposium, IGARSS, Vancouver Canada, 25-29, July, 4423-4426.

[47] Torres-Rua, A. (2017). "Vicarious calibration of sUAS microbolometer temperature imagery for estimation of radiometric land surface temperature" Sensors,17, 1499

[48] Trout, T.J., Johnson, L.F., (2007). "Estimating crop water use from remotely sensed NDVI, crop models, and reference ET." USCID Fourth International Conference on Irrigation and Drainage, Sacramento, California October 3-6, 275-285.

[49] Xia, H., Chen, X., Guo, P. A. (2009). "Shadow detection method for remote sensing images using Affinity Propagation algorithm." In Proceedings of the IEEE International Conference on Systems, Man and Cybernetics, San Antonio, TX, USA, 5-8.

[50] Zhu, Z., and Woodcock, C. E. (2012). "Object-based cloud and cloud shadow detection in Landsat imagery." Remote Sensing of Environment, 118(15), 83-94.

CHAPTER 3

Incorporation of Unmanned Aerial Vehicle (UAV) Point Cloud Products into Remote Sensing Evapotranspiration Models

3.1 Abstract

In recent years, the deployment of satellites and unmanned aerial vehicles (UAVs) has led to production of enormous amounts of data and to novel data processing and analysis techniques for monitoring crop conditions. One overlooked data source amid these efforts, however, is incorporation of 3D information derived from multi-spectral imagery and photogrammetry algorithms into crop monitoring algorithms. Few studies and algorithms have taken advantage of 3D UAV information in monitoring and assessment of plant conditions. In this study, different aspects of UAV point cloud information for enhancing remote sensing evapotranspiration (ET) models, particularly the Two-Source Energy Balance Model (TSEB), over a commercial vineyard located in California are presented. Toward this end, an innovative algorithm called Vegetation Structural-Spectral Information eXtraction Algorithm (VSSIXA) has been developed. This algorithm is able to accurately estimate height, volume, surface area, and projected surface area of the plant canopy solely based on point cloud information. In addition to biomass information, it can add multi-spectral UAV information to point clouds and provide spectral-structural canopy properties. The biomass information is used to assess its relationship with in situ Leaf Area Index (LAI), which is a crucial input for ET models. In addition, instead of using nominal field values of plant parameters, spatial information of fractional cover, canopy height, and canopy width are input to the TSEB model. Therefore, the two main objectives for incorporating point cloud information into remote sensing ET models for this study are to (1) evaluate the possible improvement in the estimation of LAI and biomass parameters from point cloud information in order to create robust LAI maps at the model resolution and (2) assess the sensitivity of

the TSEB model to using average/nominal values versus spatially-distributed canopy fractional cover, height, and width information derived from point cloud data. The proposed algorithm is tested on imagery from the Utah State University AggieAir sUAS Program as part of the ARS-USDA GRAPEX Project (Grape Remote sensing Atmospheric Profile and Evapotranspiration eXperiment) collected since 2014 over multiple vineyards located in California. The results indicate a robust relationship between in situ LAI measurements and estimated biomass parameters from the point cloud data, and improvement in the agreement between TSEB model output of ET with tower measurements when employing LAI and spatially-distributed canopy structure parameters derived from the point cloud data.

3.2 Introduction

Evapotranspiration (ET) is one of the key components in water and energy cycles, and its quantification is essential to increasing crop water use efficiency [19]. However, estimation of ET using physically-based models is not a straightforward process due to input requirements and model complexity [81]. The degree of complexity increases with non-homogeneous landscapes where both soil and vegetation contribute to radiometric temperature and surface energy fluxes [84].

One ET model that has been successful in estimating spatially distributed surface energy fluxes from aerial imagery over different landscapes is the Two-Source Energy Balance model (TSEB) [10]. The TSEB model was developed by Norman et al. [68] to compute surface energy fluxes using a single measurement of remotely-sensed surface temperature (at one view angle) to overcome the difficulties associated with characterizing the impact of canopy structure, fractional cover, sensor view, and sun zenith angle on the radiometric brightness temperature and its relationship to surface aerodynamic temperature. In recent years, numerous studies have evaluated the performance of TSEB-based models at different spatial scales, climates, and landscape heterogeneity.

Satellites and Unmanned Aerial Vehicles (UAVs) offer an opportunity to provide multi-spectral imagery and at different pixel resolutions. Satellites can cover the globe with daily

to bi-weekly re-visit times, while UAVs are designed to cover small areas, obtain higher resolution imagery, and capture information at a specific time. One important remote sensing application is estimation of vegetation biomass, and ultimately yield, typically with vegetation indices (VIs), which is easily calculated using multi-spectral imagery. Numerous research studies have been conducted to fit a linear or nonlinear regression model between VIs and biomass parameters [2]. Basically, significant differences in plant reflectances and energy emission in the optical wavelengths, particularly the red (R) and near-infrared (NIR) region, defined as the range between 700 and 1300 nm due to biochemical plant constitutes such as chlorophyll, have resulted in numerous VI formulas [97]. While the performance of VI-based models has been promising, these indices have generally been developed for uniformly distributed canopies, and are thus not as reliable in estimating plant biomass/Leaf Area Index (LAI) for strongly clumped and uniquely structured canopies such as vineyards [79].

A saturation issue occurs with well-developed canopies, wherein, despite significant increases in biomass parameters (and as a result LAI), VI values become saturated, meaning they plateau at a maximum value and are no longer sensitive to increases in LAI [12, 78]. Thus, VIs are recommended to be used only in early growing stages in denser canopies [15]. The saturated behavior of VIs versus biomass parameters is more noticeable in normalized VIs, which are set to a specific range (e.g., -1, $+1$). For example, Diarra et al. [25] evaluated the TSEB model performance using Advanced Spaceborne Thermal Emission and Reflection Radiometer (ASTER) images and the FAO-56 dual crop coefficient approach versus Eddy Covariance records for monitoring actual ET and detecting water stress over irrigated wheat and sugar beets located in the Haouz plain in the center of the Tensift basin (Central Morocco). They concluded that TSEB performed very well, even at a large scale. However, to estimate LAI based on the vegetation indices (VIs), they found that $LAI > 2.5$ saturates the normalized difference vegetation index (NDVI) and no relationship can be found between NDVI and LAI. In contrast, LAI < 1.5 resulted in a quite linear relationship between NDVI and LAI. Although LAI is a critical input for ET models, accurate estimation of LAI using

only VIs is not possible, particularly when the canopy is well-developed or is uniquely structured. In addition, investigation of the relationship between direct or indirect in situ LAI measurements and VIs is certainly time-consuming and labor-intensive [94]. Thus, exploring new techniques to minimize the need for calibration of remote sensing retrieval of LAI has significant advantages for application in complex canopies.

The development of lightweight UAVs has provided an opportunity for acquiring very high-resolution multi-spectral imagery (less than 50 cm pixel^{-1}) to produce ortho-mosaics and 3D information products such as point-cloud and digital surface models (DSMs) using photogrammetry algorithms [98]. UAV imagery has been widely used in agricultural activities and in extensive research in areas such as yield mapping [27], plant heath monitoring [99], plant water status [74], irrigation efficiency [45], phenotyping [39], and weed and pest detection [71, 87]. In comparison with satellites, UAVs are cost-effective, easy to operate, and portable, while offering very high-resolution products [73]. In addition to these features, dense 3D dense information can be generated for objects from the overlapping imagery captured by UAVs to be used in mapping plant canopy structure and volume that is likely to be more directly correlated to plant biomass and LAI than VIs.

This 3D source of information from UAV imagery is also called a point cloud, which is a dataset representing visible parts of objects where light is reflected [20]. This source can be produced by three-dimensional point-cloud modeling, photogrammetry, and computer visualization algorithms. Two popular algorithms developed for generating point cloud datasets are Structure from Motion (SfM) and Multiview-stereo (MVS), recommended for when optical cameras are used as opposed to expensive laser scanners [98]. Although 3D information for an object can be directly and accurately provided by Light Detection and Ranging (LiDAR) installed on manned and unmanned aerial vehicles, collecting point-cloud information using photogrammetry methods is much less expensive, thus representing an economically viable alternative. In addition, the SfM method requires neither external camera calibration parameters (i.e., position and orientation) nor internal parameters (i.e., lens properties) to perform the bundle adjustment to reconstruct a 3D scene [33]. In some cases, UAV point

clouds provide more details of small objects than airborne LiDAR datasets. For instance, the authors in [83] found that 45 out of 205 trees were not detected when they used an airborne LiDAR dataset, while only 14 trees were missed using a UAV photograph-based point cloud. Compared to LiDAR technology, the main weakness of UAV point cloud and photogrammetry algorithms is that UAV camera sensors are incapable of viewing beneath the canopy, which leads to sparse points and low density information of bare soil [90], whereas a single laser pulse can penetrate into an object, reach the ground, and return with multiple pulses [42]. However, because SfM and MVS are low-cost, easy to access, and easy to use, they can be efficient tools for processing UAV imagery and creating LiDAR-like point clouds [51].

Several factors affect the accuracy of point cloud datasets and consequently the digital surface model (DSM) and crop surface model (CSM) generated from them, including flight height [72], terrain morphology [9], number of ground control points (GCP) [63, 72], weather conditions [23], camera type [88], UAV types (fixed-wing versus multi-rotor) [80], photogrammetry software, and algorithms [43]. For instance, Martínez-Carricondo [59] analyzed the impact of the number and distribution of GCPs on the performance of DSMs produced from UAV photogrammetry. They found that the accuracy improved and the best performance was achieved when GCPs were placed both around the edge of and inside the study area. Although performance evaluation of UAV point cloud datasets requires a comparison with LiDAR data, recently, Aboutalebi et al. [4] developed an algorithm to validate point cloud geometrical information for shaded regions detected from UAV multi-spectral imagery.

The 3D point cloud is a useful source of information about the size, position, and orientation of an object that can be combined with UAV multi-spectral or hyper-spectral imagery to explore relationships between an object's 3D geometry information and its spectral information. Several classification methods, such as supervised and unsupervised machine learning algorithms, have been developed to generate a classified map of aerial imagery based on the similarities in spectral signatures [3]. While these algorithms fail to distin-

guish objects having similar spectral signatures (e.g., differentiating between water and shadows [36] in optical bands), point cloud would be a useful and an additional source to combine with multi-spectral imagery in order to improve the accuracy of classification methods. In addition to the capability of point clouds in segmentation and classification problems, point clouds are considered a crucial source of information for phenotyping.

UAV point cloud has been used to measure canopy height [44], tree height and crown diameter [26, 46, 70], to detect individual trees [47] and development of annual crops such as rice [14] and barley [13]. In addition, several studies show that bio-geophysical properties such as LAI and canopy reflectance parameters such as NDVI are correlated with above-ground biomass [37, 40] and ground cover percentage [28] defined as the area of soil surface masked by plants from nadir view angle [16]. Matese et al. [61] generated a vineyard canopy height model (CHM) using an SfM point cloud and compared it with an NDVI map. They found that, although CHM from SfM underestimated canopy height (about 0.5m) due to camera resolution, it is highly correlated to NDVI maps, which means that high NDVI regions correspond to high canopy height areas. Ultimately, they estimated average volume per vine by multiplying height, width, and length of the vine canopy. Mathews and Jensen [62] explored the relationship between vineyard canopy LAI and several metrics from a UAV point cloud using a step-wise regression model. These metrics include number of points within each vine's zone and height-based metrics (e.g., mean height of canopy). They reported a moderate positive correlation (0.57 in terms of R^2) between modeled LAI and in situ measured LAI. Weisis and Baret [93] proposed a method to estimate row height, width, spacing, and vineyard cover fraction using a UAV point cloud generated from red, green, and blue (RGB) images acquired over a vineyard.

Although UAV point cloud datasets and the SfM algorithm have been widely used in characterizing vegetation structure, the full potential of the photogrammetric data has not been utilized. Most of the cited studies converted dense point cloud information into Digital Elevation Model (DEM), Digital Terrain Model (DTM), DSM, or CSM (raster versions of point cloud datasets) because working with pure LiDAR-like datasets is challenging, and

algorithms and hardware that can handle such massive datasets are limited. In addition, the potential of 3D plant information to improve remote sensing-based ET models has not been explored. To the authors' knowledge, the published studies mostly focused on assessing regression models to estimate biomass parameters such as LAI, which is a key parameter in ET models, using DSMs, CSMs, or CHMs.

In this study, we propose a methodology to incorporate the 3D information extracted from a UAV point cloud into the TSEB model. In particular, a new algorithm called Vegetation Spectral-Structural Information eXtraction algorithm (VSSIXA) is developed to extract canopy height, volume, surface area, and projected surface area (fractional cover) from the point cloud dataset without converting it to a raster file. Next, the possible relationship between in situ LAI measurements, radiometric temperature (T_r), spectral information, and 3D derived structure parameters is explored. The sensitivity of the TSEB model to fixed values of the structural information over a vineyard block versus the spatial structural information is presented. The algorithm is evaluated from imagery and point cloud data collected by Utah State University AggieAir UAVs over a commercial vineyard located in California as part of the ARS-USDA GRAPEX Project (Grape Remote sensing Atmospheric Profile and Evapotranspiration eXperiment). Finally, the TSEB model is executed under different scenarios of LAI and other canopy biomass parameters and TSEB output are compared with flux tower measurements.

3.3 Materials and Methods

3.3.1 Site Description

This study was conducted as a part of GRAPEX, an ongoing project started in 2013 that seeks to improve water-use efficiency through modeling of evapotranspiration and plant stress over vineyards. The vineyard test site selected is located near the town of Lodi in California's Central Valley (38.29N, 121.12W, 38.4 m elev). This vineyard ranch called Sierra Loma (formally listed as the Borden ranch [53] consisted of two vineyard blocks, a northern and southern block, containing a flux tower in each block (Figure 3.1a). An overview

of all continuous and episodic measurements is described in detail in [53]. The northern and southern vineyard blocks (referred to as Site 1 and Site 2 hereafter, respectively) were planted with the Pinot Noir variety in 2009 and 2011, respectively. The age differences resulted in lower vegetation density, biomass and leaf area at Site 2 compared to Site 1.

Both sites share similar trellis structure and vine management. Vines are grown on identical quadrilateral cordon fixed trellis systems with installed drip irrigation in which irrigation lines run along the base of the trellis at 30 cm above ground level (agl) with two emitters (4 L/h) between each vine. The training system employs "U" shaped trellises, and canes are trained upwards. The vine trellises are 3.35 m (11 ft) apart, and the height to first and second cordons is about 1.45 and 1.9 m, respectively [53]. Vine heights vary between 2 and 2.5 m, with space between vines of 1.5 m and an East–West row orientation. The elevated canopy included significant open space between the bottom of the canopy crown and the soil surface. This open space ($\sim$0.7 m in height during peak growing season) is occupied by the narrow trellis posts and drip irrigation line (Figure 3.1b).

In order to regulate soil moisture early in the growing season following the winter season, an inter-row grass cover crop is planted in both vineyards and is mowed in either late April or early May. Two flux towers were installed in 2013, one at Site 1 and another at Site 2. The towers are installed approximately half-way North–South along the Eastern edge of each site as the predominant wind direction is from the West during sunlight hours in the growing season (Figure 3.1c).

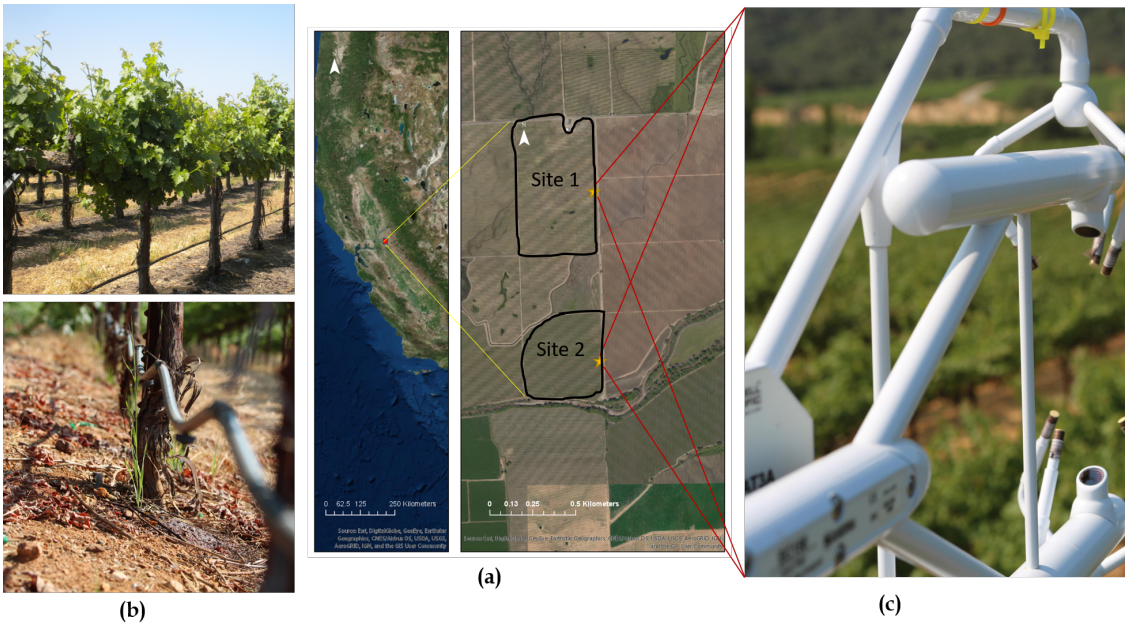

Fig. 3.1: World Imagery of the study area from Environmental Systems Research Institute (ESRI) along with the locations of the flux towers (**a**), drip irrigation system (**b**), and eddy covariance instrument (**c**) installed in the area of study.

3.3.2 AggieAir Remote Sensing Platform

AggieAir is a battery powered unmanned aerial vehicle (UAV) designed by Utah State University (USU) to carry multi-spectral sensor payloads and to acquire high-resolution aerial imagery at both optical and thermal spectra. This UAV platform consists of two cameras, a computer, a GPS module, an inertial measurement unit (IMU), a radio controller, and flight control, and it can be flown autonomously or manually [29]. The UAV can fly over the area of interest using a pre-programmed flight plan (in an autonomous mode) for an hour at a speed of 30 miles per hour [38], with the capability to provide very high-resolution imagery (less than 20 cm) at 1000 m agl and record the position and orientation of the aircraft when each image is taken. Figure 3.2 shows a layout of the AggieAir air-frame.

Fig. 3.2: AggieAir airframe layout flying and capturing imagery over the study area.

3.3.3 AggieAir UAV High-Resolution Imagery

The high-resolution images for this study were collected by an AggieAir UAV over the GRAPEX Pinot Noir vineyard. The UAV was supplied and operated by the AggieAir UAV Research Group at the Utah Water Research Laboratory at USU [7]. Four sets of high-resolution imagery (20 cm or finer) were captured over the vineyard in 2014, 2015, and 2016. These UAV flights were synchronized with Landsat satellite overpass dates and times. A sample of the imagery captured by the UAV over the study area is shown in Figure 3.3, and information describing the images is summarized in Table 3.1.

Figure 3.3 shows the study area with details of sections as captured by UAV. Cameras and optical filter information, fieldwork dates, vineyard phenological stages, and imagery resolution are summarized in Tables 3.1 and 3.2.

Table 3.1: Dates, times, cameras [1], and optical filters used to capture images with the UAV.

Date	UAV Flight Time (PDT)		UAV Elevation (agl) Meters	Bands		Cameras and Optical Filters		Spectral Response
	Lunch Time	Landing		RGB	NIR	Radiometric Response	MegaPixels	
9 August 2014	11:30 a.m.	11:50 a.m.	450	Cannon S95	Cannon S95 modified (Manufacturer NIR block filter removed)	8-bit	10	RGB: typical CMOS NIR: extended CMOS NIR Kodak Wratten 750 nm LongPass filter
2 June 2015	11:21 a.m.	12:06 p.m.	450	Lumenera Lt65R Color	Lumenera Lt65R Monochrome	14-bit	9	RGB: typical CMOS NIR: Schneider 820 nm LongPass filter
11 July 2015	11:26 a.m.	12:00 p.m.	450	Lumenera Lt65R Color	Lumenera Lt65R Monochrome	14-bit	12	RGB: typical CMOS NIR: Schneider 820 nm LongPass filter
2 May 2016	12:53 p.m.	1:17 p.m.	450	Lumenera Lt65R Mono	Lumenera Lt65R Mono	14-bit	12	RGB: Landsat 8 Red Filter equivalent NIR: Landsat 8 NIR Filter equivalent

[1] The use of trade, firm, or corporation names in this article is for the information and convenience of the reader. Such use does not constitute official endorsement or approval by the US Department of Agriculture or the Agricultural Research Service of any product or service to the exclusion of others that may be suitable.

Table 3.2: Dates, optical and thermal resolution, point cloud density and phenological stages of the vine and cover crop when the images were captured by the UAV.

Date	Optical Resolution	Thermal Resolution	Point Cloud density (point/m^2)	Vine Phenological Stage	Phenological Stage of Cover Crop
9 August 2014	15 cm	60 cm	37	Veraison towards harvest	Mowed stubble
2 June 2015	10 cm	60 cm	118	Near veraison	Senescent
11 July 2015	10 cm	60 cm	108	Veraison	Mowed stubble
2 May 2016	10 cm	60 cm	120	Bloom to fruit set	Active/green

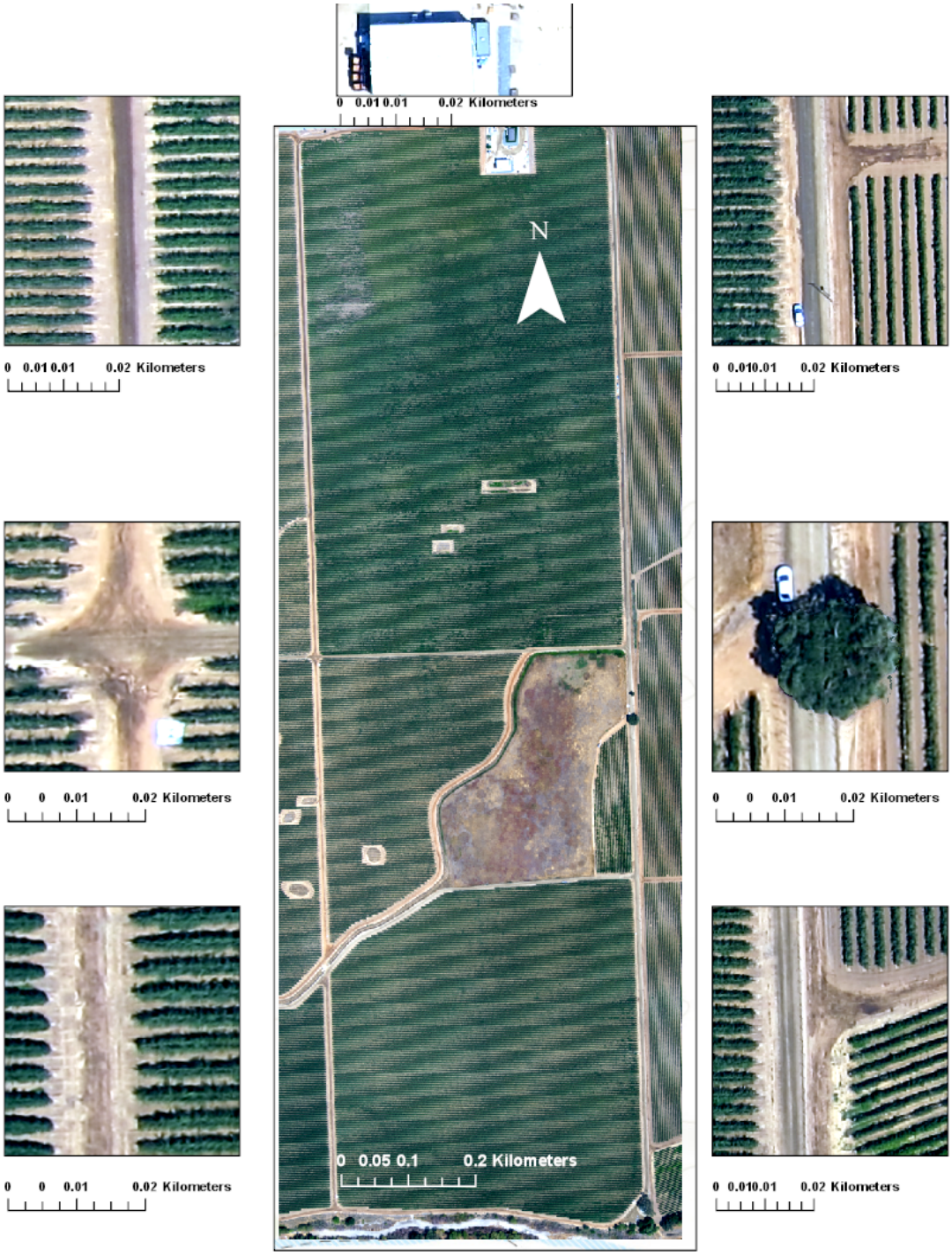

Fig. 3.3: Example of high-resolution imagery captured by AggieAir over the study area in August 2014.

As described in Tables 3.1 and 3.2, the imagery covers all major phenological vineyard stages. The cameras used in the current study ranged from consumer-grade Canon S95 cameras to industrial type Lumenera monochrome cameras fitted with narrowband filters equivalent to Landsat 8 specifications. The thermal resolution for all four flights was 60 cm, and the visible and near-infrared (VNIR) were 10 cm, except for the August flight.

3.3.4 AggieAir UAV Image Processing

A three-step image processing phase followed imagery acquisition. This process included (1) radiometric calibration, (2) image mosaicking and orthorectification, and (3) Landsat harmonization. In the first step, the digital images were converted into a measure of reflectance by estimating the ratio of reference images from pre- and post-flight Labsphere [56]Lambertian panel readings. This conversion method was adapted from Neale and Crowther [65]; Miura and Huete [64]; and Crowther [22] and is based solely on the reference panel readings, which do not require solar zenith angle calculations. This procedure additionally corrected camera vignetting effects that were confounded in the Lambertian panel readings. In the second step, all images were combined into one large mosaic and rectified into a local coordinate system (WGS84 UTM 10N) using Agisoft Photoscan software [8] and survey-grade GPS ground measurements. The software produced hundreds of tie-points between overlapping images by using photogrammetric principles in conjunction with image GPS log file data and UAV orientation information from the on-board IMU to refine the estimate of the position and orientation of individual images. The output of this step is an orthorectified reflectance mosaic [29]. Since different optical sensors with different spectral responses are used to capture high-resolution imagery (Table 3.1) and the spectral information of vegetation will be used to model LAI, a bias correction method is necessary to remove the disagreement of remotely sensed information regardless of pixel resolution and sensor. Thus, in the third step, the UAV optical high-resolution imagery was upscaled to Landsat resolution using the Landsat point spread function. If biased, it was corrected with a linear transformation [5]. For thermal imagery processing, only step 2 was applied. The resulting thermal mosaic consisted of brightness temperature in degrees

Celsius. Moreover, a vicarious calibration for atmospheric correction of microbolometer temperature sensors proposed by Torres-Rua [85] was applied to the thermal images.

3.3.5 Field Measurements, Multi-Spectral Imagery, Point Cloud, and LiDAR Datasets

Photogrammetric point clouds were produced from the multispectral images (Figure 3.4a) with a density of ∼40 (points/m^2) for the 15-cm resolution (2014 imagery) and ∼100 (points/m^2) for the 10-cm resolution (2015 and 2016 imagery), after which a DSM was generated at the same spatial resolution as the original imagery (i.e., 15 cm for 2014 and 10 cm for 2015 and 2016). In addition to UAV point cloud products that describe the surveyed surface, a LiDAR derived bare soil elevation (DTM) product for the same location, collected by the NASA G-LiHT (Goddard's LiDAR, Hyperspectral Thermal Imager) project in 2013, was used [21] (Figure 3.4b).

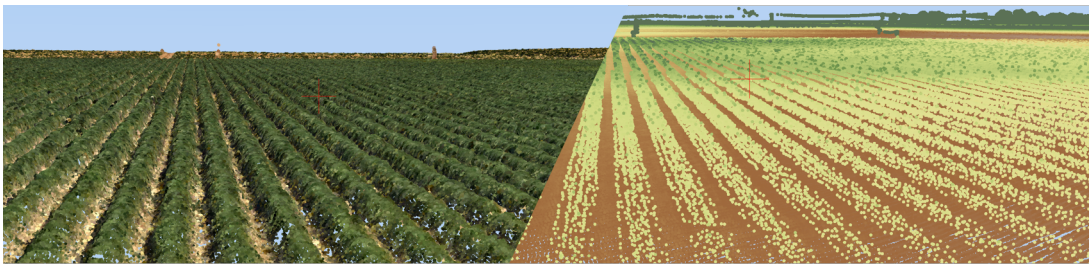

(a) (b)

Fig. 3.4: Example of a point cloud dataset produced by AgiSoft using AggieAir imagery and SfM method (**a**) versus LiDAR dataset collected by NASA G-LiHT (**b**) for the area of study.

In addition, ∼80 LAI measurements for each flight were acquired using the Plant Canopy Analyzer (PCA, LAI2200C, LI-COR, Lincoln, NE, USA) as the indirect in situ LAI measurements (Figure 3.5). These LAI measurements were validated with direct LAI (i.e., destructive sampling) measurements [94].

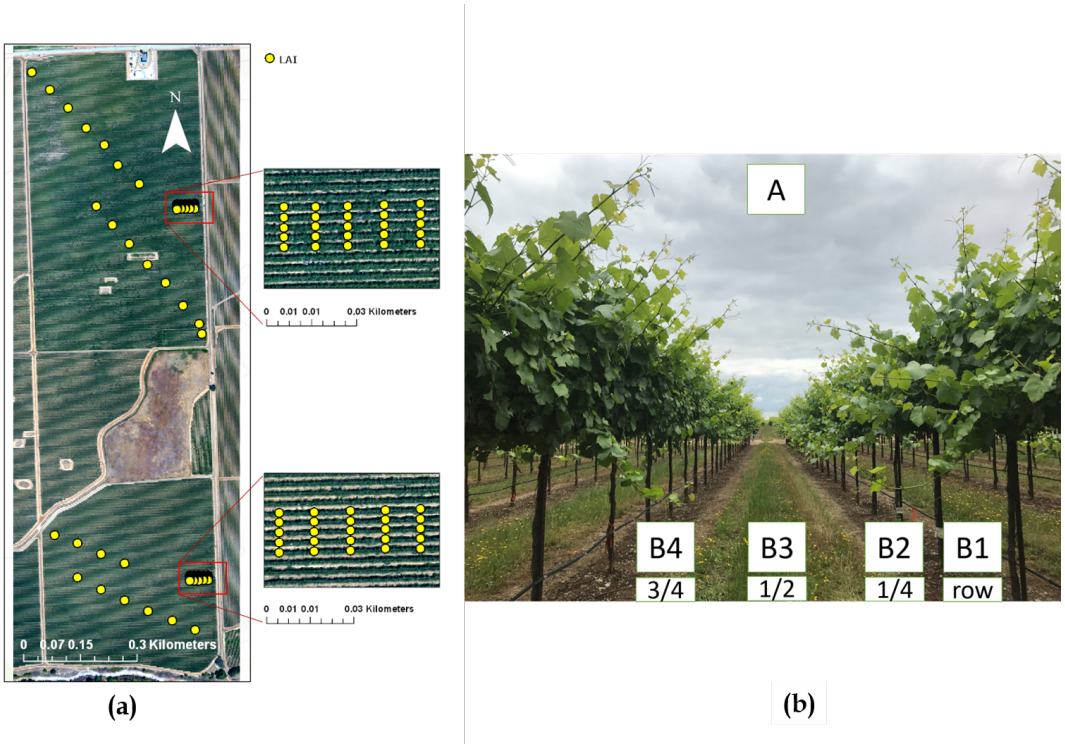

Fig. 3.5: (**a**) leaf area sampling locations, (**b**) measuring LAI according to GRAPEX protocol [94].

The location of each measurement is recorded with a precise Real-time kinematic (RTK) GPS (Figure 3.5). To evaluate the relationship between vine spectral-structural information and in situ LAI measurements, first the footprint of the LICOR-2200C must be defined. According to White et al. [94], it was assumed that the LICOR-2200C was measuring LAI in a rectangle 1 m wide and 3 m long. However, the smallest valid resolution in applying the TSEB model for the study area was determined to be 3.6-m grid [67], which means that all required inputs for the TSEB model must be set to 3.6-m grids. Due to inconsistency between the LICOR-2200C footprint and the TSEB model resolution and its unknown impact on the LAI map, vine spectral-structural information is extracted for both rectangular and square buffers around LAI measurements (Figure 3.6).

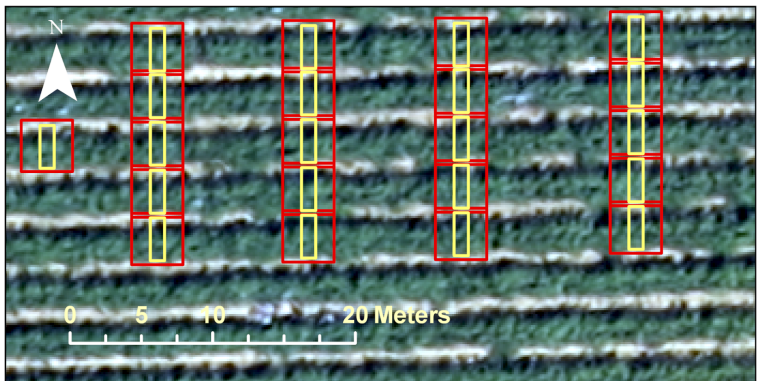

Fig. 3.6: Square and rectangle buffers around LAI measurements.

Eddy covariance and micrometeorological data, surface fluxes, and meteorological conditions are being collected year round at each of the vineyard sites for starting in 2013. The raw high-frequency data have been fully processed and evaluated for quality control and are stored as hourly block-averaged data. Wind speed and wind direction are measured via sonic anemometer (CSAT3, Campbell Scientific) mounted 5 m agl facing due west (270°). Air temperature is measured via a humidity/temperature sensor (HMP45C, Vasaila) mounted at 5 m agl. Water vapor density is measured via a humidity/temperature sensor (HMP45C, Vasaila) mounted at 5 m agl. Atmospheric pressure is measured by a pressure sensor (EC150, Campbell Scientific) mounted 5 m agl facing due west (270°). Incident long-wave radiation and net radiation are measured via a 4-component net radiometer (CNR-1, Kipp & Zonen,) mounted 5 m, agl facing southwest (225°). Sensible and latent heat flux are derived from CSAT and EC150 data. Soil heat flux is the mean of the five measurements collected along a transect across the inter-row.

For the post-processing of the turbulent fluxes, the high-frequency data was screened to identify and remove flagged values (CSAT or infrared gas analyzer (IRGA) diagnostic), physically unrealistic values, and statistical outliers (data spikes). The sonic temperature was converted to air temperature following Schontanus [77] and Lui [58]. The measurements of the wind velocity components were rotated into the mean streamwise flow following the 2D coordinate rotation method described by Tanner and Thurtell [82]. The wind velocity

and the scalar quantities were adjusted in time to account for sensor displacement and optimize the covariance. The frequency response correction of Massman [60] was applied. The turbulent fluxes were calculated. The initial estimates of the latent heat flux and the carbon dioxide flux were then corrected for density effects following the Webb et al. method [92]. The initial estimates of the sensible heat flux were corrected for buoyancy effects [31]. The soil heat flux was corrected for heat storage in the overlying soil layer [69]. The data were quality controlled via visual inspection to remove physically unrealistic values due to rainfall, dew, and similar events. Output of fluxes and ancillary micrometeorological data are stored as hourly block-averaged data.

Traditionally, any imbalance of net radiation (Rn) - soil heat flux (G) versus sensible heat flux (H) + latent heat flux (LE) is considered a lack of energy balance closure. It is often assumed that H and LE have been underestimated by the eddy covariance method, and the level of underestimation is often used to indicate the reliability of the eddy covariance estimates of H + LE [86]. The value of the ratio of (Rn-G)/(H+LE) should ideally be equal to 1, but, generally, values over 0.80 are considered reliable [86, 96]). In this study, for any imbalance between Rn-G and H+LE, closure was forced by assuming that the Bowen ratio H/LE is correct because both are probably underestimated. Moreover, recent studies indicate that flow distortion for non-orthogonal sonics underestimate vertical wind and hence the turbulent fluxes [30, 32, 41, 49]. Therefore, energy is added to H and LE (H_{BR} and LE_{BR}) according to the Bowen ratio (BR) to reach a closure value of 1.0; this is typically called forcing energy balance closure [86]. Therefore, H and LE from eddy covariance are modified by Equations (3.1) and (3.2):

$$H_{BR} = \frac{H}{H + LE} \times (Rn - G - H - LE) + H, \tag{3.1}$$

$$LE_{BR} = \frac{LE}{H + LE} \times (Rn - G - H - LE) + LE. \tag{3.2}$$

3.3.6 Vegetation Structural-Spectral Information Extraction Algorithm (VSSIXA)

To analyze and extract 3D information from the point cloud dataset and spectral information from the high-resolution imagery, a new algorithm called Vegetation Structural-Spectral Information eXtraction Algorithm (VSSIXA), using Python and ArcGIS Pro libraries, was developed. The code of this algorithm is available at [91]. Figure 3.7 shows components of VSSIXA in a flowchart diagram.

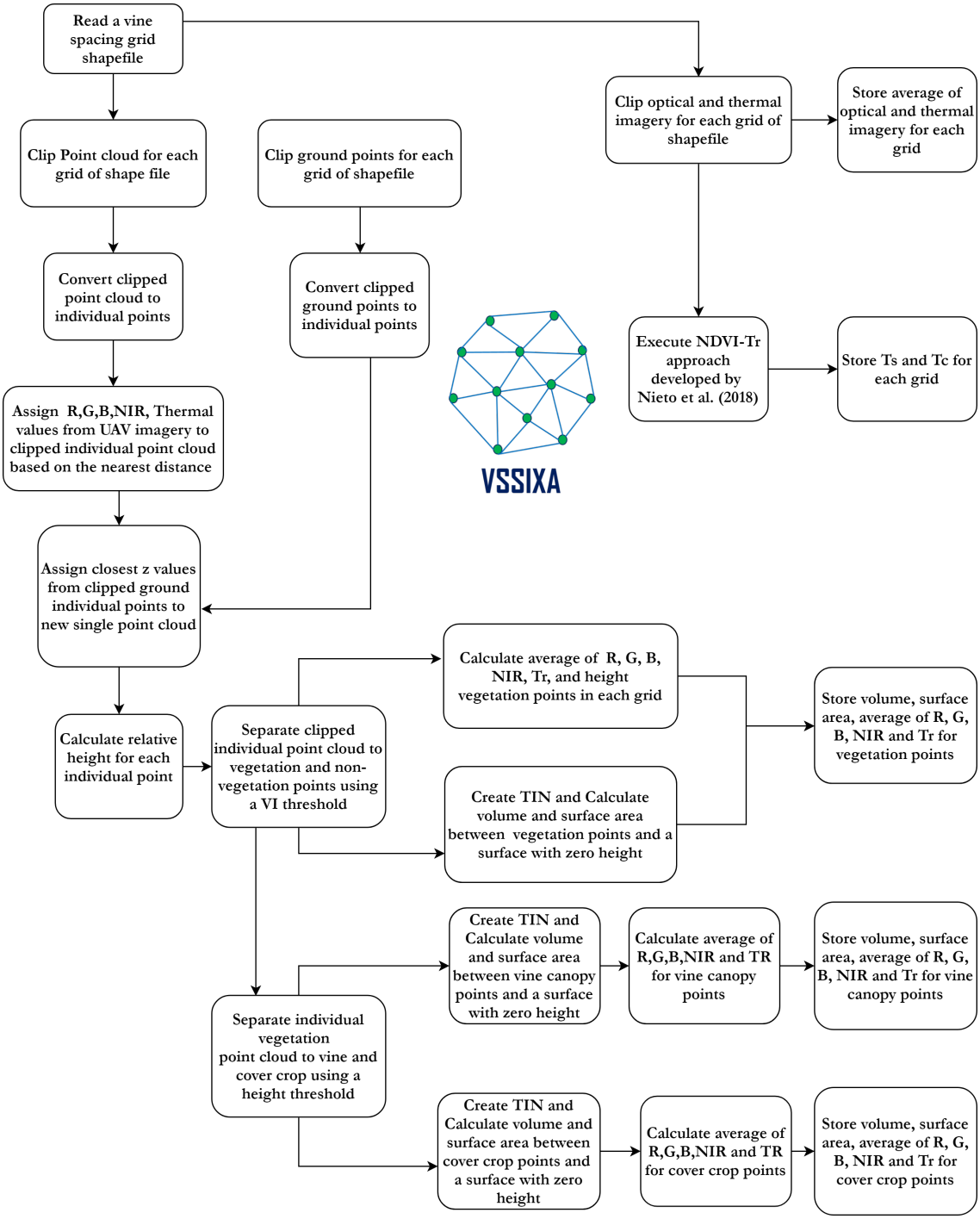

Fig. 3.7: A workflow of proposed VSSIXA algorithm.

As shown in Figure 3.7, the VSSIXA algorithm requires a point cloud dataset as the primary input and a shapefile, optical and thermal imagery, and a ground point as the

secondary inputs. In the first step, a vine spacing grid shapefile is read and point cloud, ground points, and UAV imagery are clipped for each grid of the shapefile. In this step, the average of the UAV imagery for each band and for each grid, and consequently the partitioning of Tr into soil temperature (Ts) and canopy temperature (Tc) are executed and stored. In this step, Ts and Tc estimations are by-products of VSSIXA. Next, clipped ground points and point cloud datasets are converted to individual point datasets, Red (R), Green (G), Blue (B), near-infrared (NIR), and Tr bands from UAV imagery along with z-values from ground points are assigned to each single point cloud based on nearest distance, and relative height (Point cloud z-Ground z) is calculated. Therefore, the Attribute Table of each point constitutes point cloud height, ground height, relative height, RGB, NIR, and thermal information. Next, the individual points are separated into vegetation and non-vegetation points using a VI threshold (e.g., NDVI > 0.6), and volume, surface area, height, and the average of Tr and optical bands for vegetation points using a triangulated irregular network (TIN) are calculated and appended into the Attribute Table. In the last stage, vegetation points are separated into vine canopy and cover crop points based on a relative height threshold (0.5 m in this study) and derived structural and spectral information for vine and cover crop points is separately recalculated. Because structural and spectral information for each point has been extracted and geographical information for those single points has been accessed, a profile of information, such as average height, vine temperature, and VIs, can be extracted. VSSIXA is able to extract and store these profiles in a comma-separated values (CSV) format.

VSSIXA is coded in two different versions, VSSIXA-I and VSSIXA-II. VSSIXA-I requires only a point cloud dataset, while VSSIXA-II requires both point cloud data and LiDAR ground points. In VSSIXA-I, after appending multi-spectral information to each point in each grid, the point cloud is classified into the ground and non-ground classes based on an NDVI threshold. The relative height is calculated based on Point Cloud z and the minimum value of ground point heights. Therefore, the structural information is calculated between TIN created from non-ground points and a surface with height zero. If there are

no multi-spectral data to separate ground points from non-ground points or if a grid has no ground points (e.g., fully covered by vegetation), VSSIXA-I considers the minimum z-value from all points to calculate relative height. In contrast, the classified ground points exist for VSSIXA-II, due to LiDAR penetration into vegetation and detection of ground. Therefore, z-values from LiDAR ground points are affixed to the point cloud from a spatial perspective (e.g., closest distance) to calculate relative height and then, similar to VSSIXA-I, the structural information is calculated. Since VSSIXA-I assigns one value (minimum z value of ground points) to non-ground points in each grid, it assumes that the slope of the ground surface in each grid is close to zero. Thus, VSSIXA-I is appropriate for flat terrain, even though it requires only a point cloud dataset. In contrast, because VSSIXA-II assigns ground z values to each point, the impact of slope is considered, albeit it requires both point cloud and LiDAR ground point datasets (Figure 3.8).

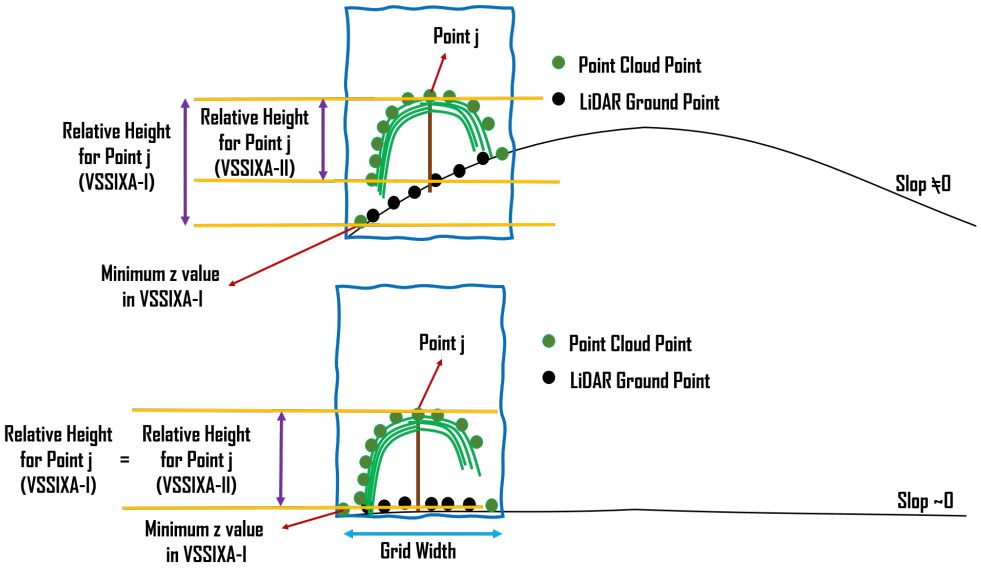

Fig. 3.8: Differences between VSSIXA-I and VSSIXA-II determination of ground elevation and canopy height.

The difference between VSSIXA-I and VSSIXA-II in relative height calculation may lead to differences in the estimation of canopy volume. It is expected that VSSIXA-II estimates higher values for canopy volume compared to VSSIXA-I. In contrast, there should

not be a significant difference between surface area or projected surface area estimated by VSSIXA-I and VSSIXA-II (Figure 3.9). Thus, if all the structural parameters are used to evaluate the relationship between LAI and VSSIXA outputs, either VSSIXA-I or VSSIXA-II must be employed for the entire study area due to inconsistency between canopy volume and height estimated by VSSIXA-I and -II unless the slope of each grid can be considered as zero (similar to the current study area).

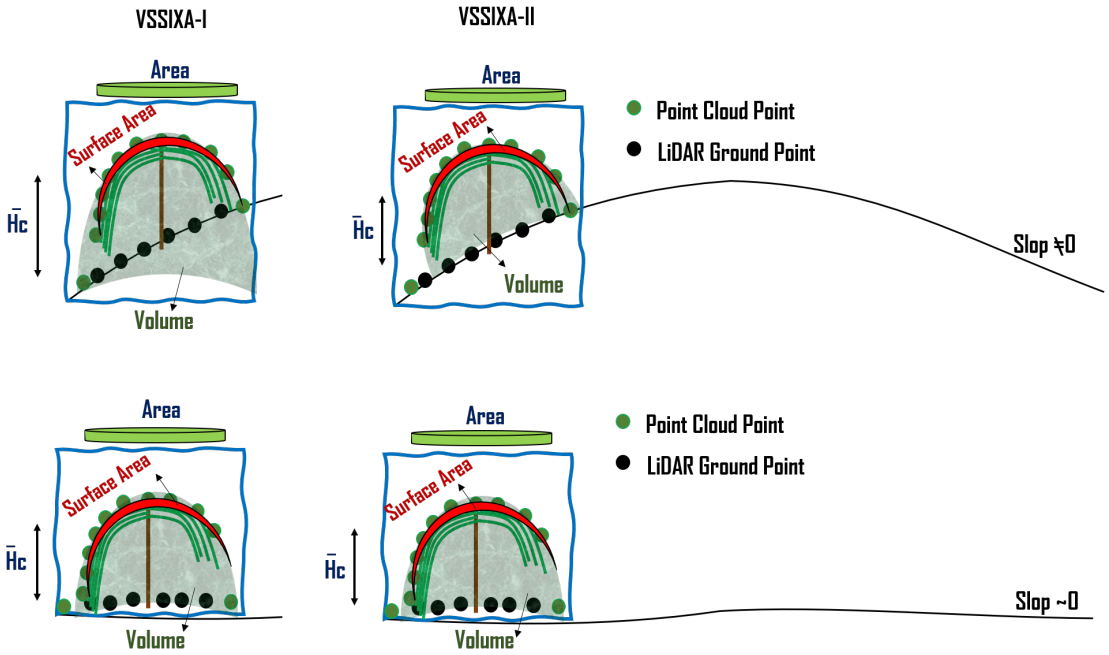

Fig. 3.9: Differences between VSSIXA-I and VSSIXA-II in estimation of canopy surface area, projected surface area, volume, and average height.

Genetic Programming: GP

Genetic Programming (GP) is a machine learning method inspired by the genetic algorithm (GA). In contrast to a trained network with Artificial Neural Network (ANN) and Support Vector Machine (SVM), the output of GP is a trained equation that researchers can simply use and calibrate in different study areas. Similar to GA, GP uses a searching process to solve optimization problems. It starts with many possible solutions in the form of chromosomes, in which each gen could be a function (*sin*, *log*, *cos*, and *exp*), an

operator (+,−, /), an input variable (x_1, $\cdots$, x_n), or a number (1, 2, 3, $\cdots$, n). In iteration 1, chromosomes (equations) are generated by a random initial solution. Then, chromosomes are ranked (from the best to the worst) based on an objective function (e.g., Root Mean Square Error (RMSE)) calculated for each chromosome. In other words, input data ($\vec{X} = x_1, \cdots, x_n$) are input to each chromosome (equation) to calculate outputs ($f_1(\vec{X}), \cdots, f_n(\vec{X})$); the outputs of each chromosome ($f_1(\vec{X}), \cdots, f_n(\vec{X})$) are compared with observed values ($y_1, \cdots, y_n$); an objective function (e.g., RMSE) is calculated for each chromosome (equation); and these initial solutions are sorted based on objective function values. In subsequent iterations, solutions (chromosomes) must be updated. Each chromosome can be modified in each iteration of the search process using cross-over and mutation functions. Cross-over is responsible for interpolation between two chromosomes, and mutation is designed for extrapolation. In each iteration, if the stopping criteria (e.g., number of iterations $<$ 1e6) is satisfied, GP will stop, and the first among the sorted chromosomes, which is a fitted linear or nonlinear equation, is reported as the best solutions. Figure 3.10 shows the evolving process for one chromosome after one iteration using mutation and cross-over functions.

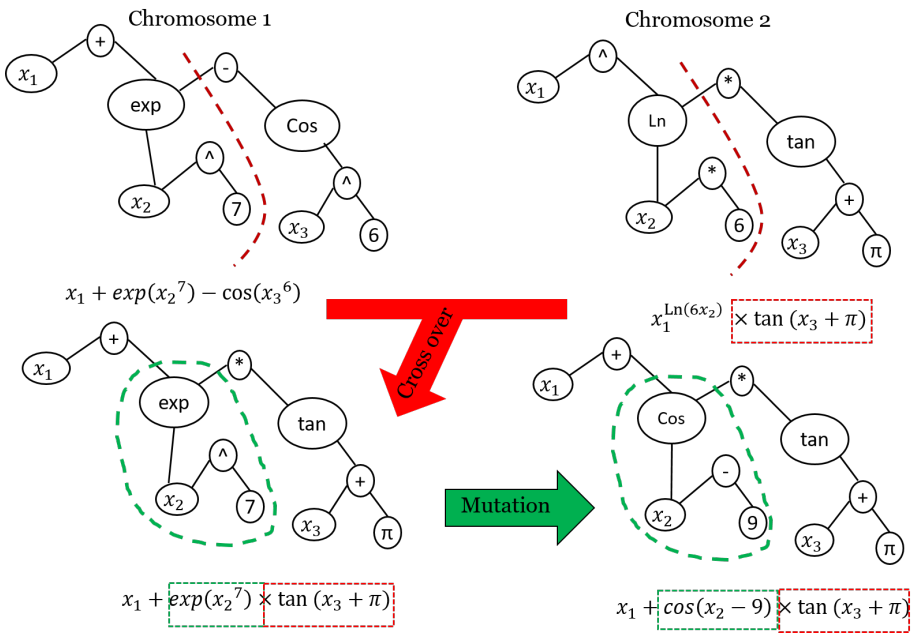

Fig. 3.10: A graphical visualization of the various stages of GP to update solutions (chromosomes).

In this study, spectral-structural information (e.g., canopy volume and surface area) estimated by VSSIXA for each in situ LAI domain (input dataset) and in situ LAI (output dataset) is used train GP. Thus, GP is employed to search possible linear and nonlinear relationships (equations) between VSSIXA outputs (e.g., canopy volume and surface area) and in situ LAI in order to create LAI maps for the TSEB model.

One of the advantages of GP is access to a formula in which inputs are related to outputs, whereas the trained networks of popular machine learning methods such as ANN and SVM do not explicitly provide a formula, only results and performances. Without access to trained networks (weights, bias, and sometimes kernel parameters), reproducing results or evaluation of the performance of the trained network for a different case study is not possible. In contrast, the trained network of GP is reported in the form of an equation (sometimes a complex equation). This feature makes GP a tool [1] with a transferable trained network, although the proposed GP models should be confirmed under different planting geometries, and local calibration may be needed.

A software called "Eureqa" [75, 76] is used to execute GP, wherein 70% of the dataset records are considered for training the network, and 30% are allocated for the testing procedure. To train GP, basic (e.g., +,−,*,/), trigonometric (sin, cos), and exponential formula building-blocks are used, and maximizing R-square is considered the objective function.

3.3.7 TSEB-2T Model

TSEB-2T is a version of the TSEB model that was developed for when both Ts and Tc can be derived from nadir and off nadir Tr viewing angles [54] or by deriving pure vegetation and soil/cover crop pixels in a contextual spatial domain, namely VI-Tr space [67]. The contextual domain is a 3.6 x 3.6 m grid mapping NDVIs versus Tr (Figure 3.11). Next, a linear function via least squares regression is fit to the NDVI-Tr pairs. Pure vegetation and soil/cover crop pixel values are defined using histogram analysis or LAI-NDVI empirical relationships for the entire field. These threshold values are substituted into the fitted linear equation, and two temperatures are retrieved. The lowest and highest temperatures are assigned for Tc and Ts, respectively.

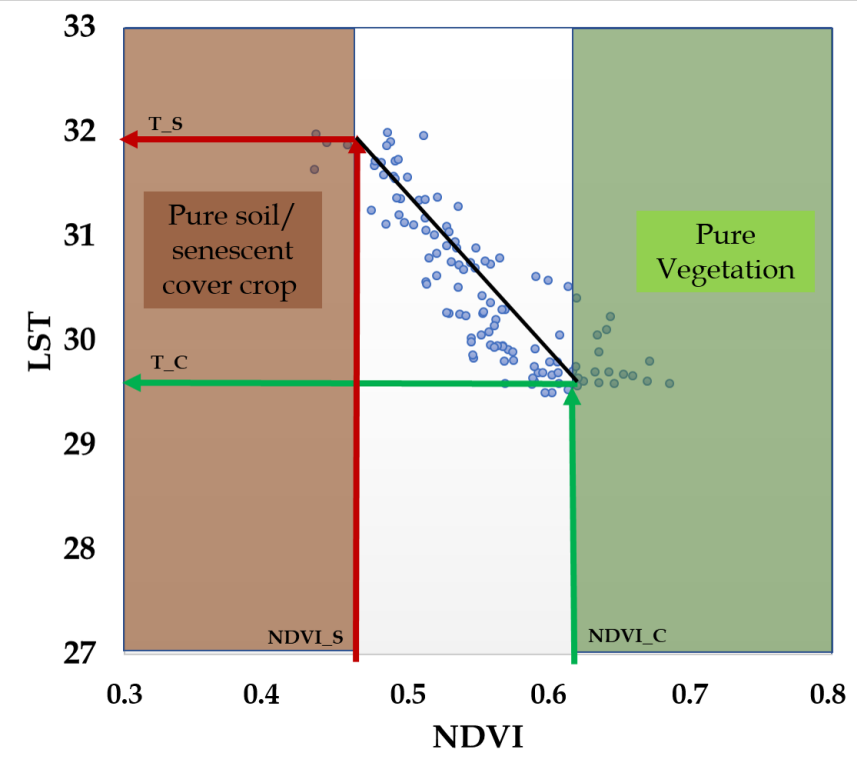

Fig. 3.11: Example of a contextual NDVI-Trad scatterplot used for searching Ts and Tc within a 3.6-m grid.

In addition to Ts and Tc, TSEB requires LAI, fractional cover, soil and canopy emissivity, albedo, information of the canopy structure (leaf width, canopy height), and atmospheric forcing, air temperature (Ta), wind speed coming, solar radiation and vapor pressure. VSSIXA is able to produce LAI, fractional cover, and canopy structure information such as canopy height based on the point cloud information. Without VSSIXA, LAI is estimated based on empirical relationships between VIs and in situ LAIs, and fractional cover and canopy height are fixed values for the entire domain.

In TSEB with Tc and Ts estimates (Figure 3.12) using the TSEB-2T version [54, 67], net shortwave (Sn) and longwave radiation (Ln) are generally calculated at the first steps. Next, net longwave radiation is separated into canopy and soil net longwave radiation (Ln_s and Ln_c) using a formulation developed by Kustas and Norman [55] (Equations (3.3) and

(3.4)):

$$Ln_c = (1 - exp(-k_L \Omega LAI))(L_{sky} + L_s - 2L_c), \tag{3.3}$$

$$Ln_s = exp(-k_L \Omega LAI)L_{sky} + (1 - exp(-k_L \Omega LAI))L_c - L_s, \tag{3.4}$$

where k_L is the long-wave radiation extinction coefficient, Ω is the vegetation clumping factor proposed by [55], and L_s, L_c and L_{sky} $(W/(m^2))$ are the long-wave emissions from soil, canopy and sky, respectively.

In addition, net shortwave radiation is separated into canopy and soil net shortwave radiation (Sn_s and Sn_c) based on the canopy radiative transfer model developed by Campbell and Norman [17]. Then, net radiation at the soil and canopy are calculated based on the summation of net longwave and shortwave radiation for each component (Rn_s and Rn_c; Equations (3.5) and (3.6)):

$$Rn_c = Ln_c + (1 - \tau_s)(1 - \alpha_c)S, \tag{3.5}$$

$$Rn_s = Ln_s + \tau_s(1 - \alpha_s)S, \tag{3.6}$$

where τ_s is solar transmittance through the canopy, S $(W/(m^2))$ is the incoming short-wave radiation, α_c and α_s are the canopy and soil albedo, respectively.

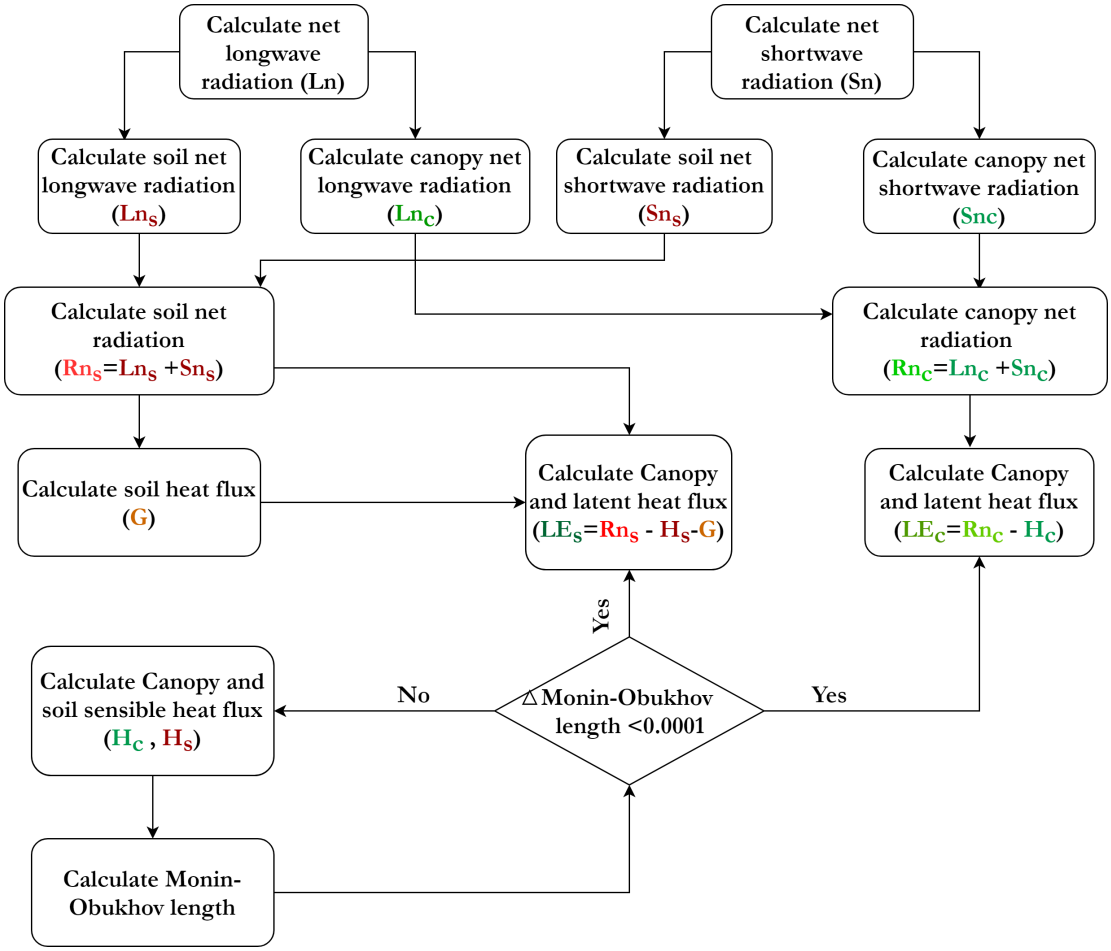

Fig. 3.12: Connections between TSEB model components for the energy fluxes calculation.

Since soil heat flux (G) is assumed to be a portion of Rn_s (e.g., 30%), it is simply computed at this step. Next, sensible heat flux is estimated for the canopy and soil components (H_s and H_c) initially assuming a neutral atmospheric stability, but it is corrected in an iterative loop until changes in the Monin–Obukhov stability length scale reach a minimum (i.e., changes between consecutive calculations of the Monin–Obukhov length is less than 0.00001). Ultimately, latent heat flux for soil and canopy (LE_s and LE_c) are calculated as residuals of the soil and canopy energy balance equations, namely Equations (3.7) and (3.8), respectively:

$$LE_S = Rn_S - G - H_S, \tag{3.7}$$

$$LE_C = Rn_C - H_C. \tag{3.8}$$

3.3.8 Data Analysis

The relationship between VSSIXA outputs and in situ LAI measurements, as well as the accuracy of the TSEB model considering different inputs against eddy covariance measurements, is evaluated using coefficient of determination (R^2), mean absolute error (MAE), RMSE, and relative root mean square error (RRMSE) (Equations (3.9)–(3.12)):

$$R^2 = 1 - \frac{\sum_{i=1}^{n}(M_i - E_i)^2}{\sum_{i=1}^{n}(M_i - \bar{M}_i)^2}, \tag{3.9}$$

$$MAE = \frac{\sum_{i=1}^{n}|M_i - E_i|}{n}, \tag{3.10}$$

$$RMSE = \sqrt{\frac{\sum_{i=1}^{n}(M_i - E_i)^2}{n}}, \tag{3.11}$$

$$RRMSE = \frac{RMSE}{\bar{M}_i} \times 100, \tag{3.12}$$

in which n is the number of observations, M_i is measured value, E_i is estimated value, and $\bar{M}_i$ is the average of measured values. R^2 is often used to estimate the performance of the models and shows the fraction of the estimated values that are closest to measurement data. MAE is an indicator for average model performance error and is less sensitive to outliers [95]. RMSE is designed to show the predictive capability of a model in terms of its absolute deviation [24]. RRMSE is a dimensionless version of RMSE, and model accuracy is connoted excellent when RRMSE $< 10\%$, good if $10\% <$ RMSE $< 20\%$, fair if $20\% <$ RMSE $< 30\%$ and poor if RRMSE $> 30\%$ [57].

3.4 Results

3.4.1 VSSIXA Outputs

VSSIXA is able to provide information such as canopy height, volume, surface area, and projected surface area (PSA) directly from the point cloud data. Due to the presence

of both grass cover crop and grapevine canopy in the study area, a 0.5-m threshold is considered to separate grapevine canopy from grass. After the separation, the vegetation structure information is executed for three categories: (1) vine canopy, (2) cover crop, and (3) vegetation (both vine canopy and cover crop). Examples of this information derived from a 2015 July point cloud dataset is shown in Figure 3.13.

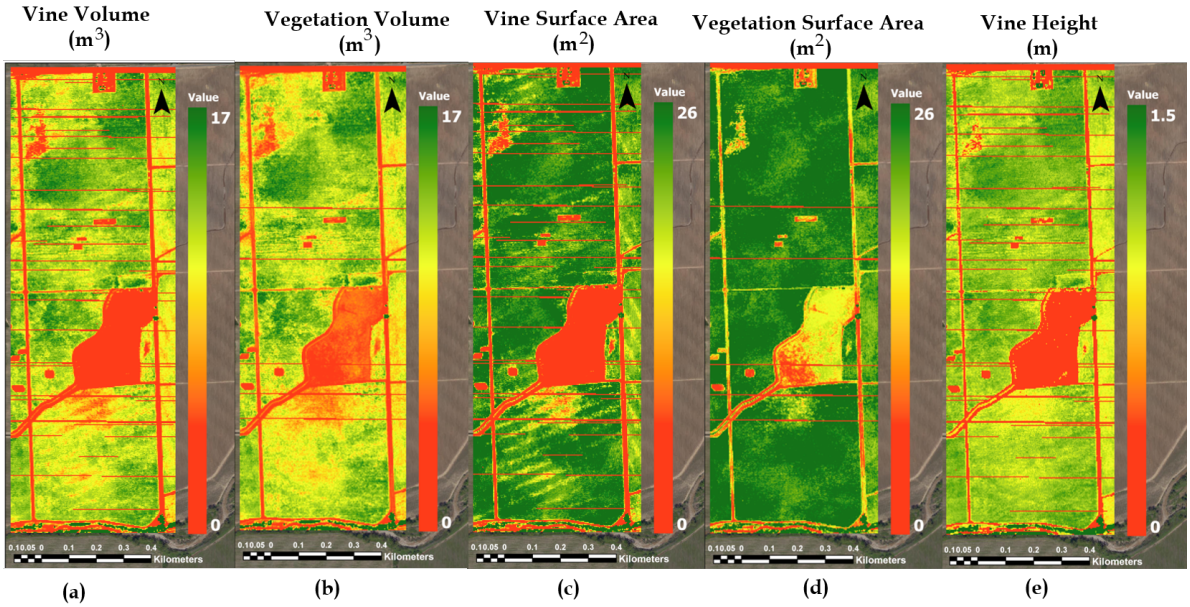

Fig. 3.13: Examples of (**a**) vine volume, (**b**) vegetation volume, (**c**) vine surface area, (**d**) vegetation surface area, (**e**) vine height and (**f**) cover crop height calculated for a 2015 July point cloud dataset using VSSIXA-II (horizontal lines are areas of missing data).

Vegetation volume and vine volume (Figure 3.13) show similar patterns, indicating Site 1 (northern site) clearly has higher biomass compared to Site 2 (southern site). These differences in biomass amount are likely related to the difference in age, with vines at Site 1 more mature than Site 2. The grapevines planted in Site 1 have greater height and surface area versus those planted in Site 2. As expected, canopy volume, height, and surface area values in an area between the north and south blocks and roads are close to zero since these areas contain no grapevine. Although zero plant height regions are not of interest in this study, these zero height values do show the accuracy of the point cloud data since overlaying

the high resolution imagery of Figure 3.3 has a very high correspondence with roads and the non-vineyard field separating north and south vine blocks. Low, dense, and short vegetation in the area separating the two vineyard blocks, which is visible in Figure 3.3, appeared in vegetation volume and vegetation surface area maps (Figure 3.13b,c). The horizontal lines of missing data are due to a lack of sufficient data points in the UAV point cloud acquisition and are probably a result of inadequate overlapping in the UAV imagery. This can be solved by increasing the overlap in adjacent image acquisitions.

As illustrated in Figure 3.13, volume and surface area are separately calculated for vegetation and vine canopy points due to the presence of grass cover crop. In terms of volume and surface area estimation, the main difference between vegetation and vine canopy is that the vegetation TIN file is created based on all non-zero heights, while, in the vine TIN file, points with height less than 0.5 m are excluded (Figure 3.7). As shown in Figure 3.14, this exclusion leads to increasing vegetation surface area and decreasing vegetation volume compared to structural vine information if gaps inside the vines are detected in the photogrammetry process.

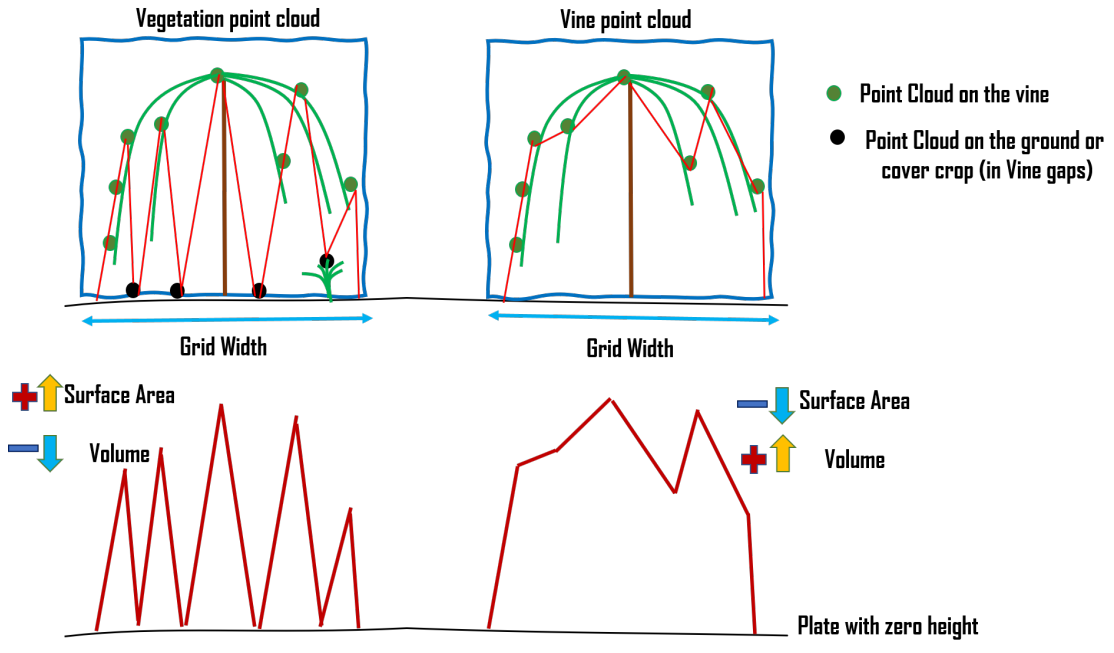

Fig. 3.14: Impact of filtering z < 0.5 m on the vegetation/canopy volume and surface area.

3.4.2 Computation Time of VSSIXA

Although VSSIXA can precisely estimate structural information from point cloud data, the speed of the computational process is relatively slow due to the massive calculations needed to append spectral information into point cloud data and create TIN files. We used a relatively fast computer with a 2-terabyte Solid-state drive (SSD), 12 cores, 24 logical processors, and 128 gigabytes of Double Data Rate 4 (DDR4) RAM to execute VSSIXA over the study area. However, for each 3.6-m grid, both VSSIXA-I and VSSIXA-II require ∼40 s to extract and store spectral-structural information. The study area contains ∼77,000 grids. Therefore, each flight takes 35 days (77,000 × 40/3600 /24) to be processed by VSSIXA. The 2015 July point cloud was processed by four fast computers to decrease the total running time to two weeks. Due to the long computational time of VSSIXA, spectral-structural information of other flights was extracted for footprints of the eddy covariance instrument and in situ LAI domains. It is possible that parallelization can enhance VSSIXA performance, but further investigation is needed.

3.4.3 In-Situ LAI versus VSSIXA Outputs

To evaluate the relationship between VSSIXA outputs and in situ LAI measurements, first the footprint of the LICOR-2200C must be defined. According to [94], it was assumed that the LICOR-2200C is measuring LAI in a rectangle 1 m wide and 3 m long. However, the smallest valid resolution of the TSEB model for the study area is a 3.6-m grid (square), which means that all required inputs for the TSEB model must be set to 3.6-m grids. Due to inconsistency between the LICOR-2200C footprint and the TSEB model resolution and its unknown impact on the LAI map, VSSIXA is executed for both rectangular and square buffers around LAI measurements (Figure 3.6).

To assess the performance of VSSIXA-I and VSSIXA-II, and particularly the importance of precise ground points (ground LiDAR dataset), spectral and structural information of the vegetation and canopy are computed by both versions of VSSIXA (VSSIXA-I and VSSIXA-II) and for both rectangular and square buffers (Figure 3.6). The relationship between in situ LAIs and VSSIXA outputs based on R^2 are illustrated in Table 3.3.

Table 3.3 shows R^2 calculated between in situ LAI and VSSIXA outputs. In general, results showed that structural information is more correlated to LAI compared to UAV spectral information, and among all the structural-spectral information extracted by VSSIXA, nine parameters had stronger correlation with LAI: NDVI, Tr, N_v, $Volume_v$, $SArea_v$, $Area_v$, $Volume_{vc}$, $SArea_{vc}$, $Area_{vc}$. According to the definition of LAI [total one-sided leaf area per unit ground surface area], the strongest correlation was expected to be between LAI and surface areas ($SArea_v$ and $SArea_{vc}$). Table 3.3 shows that, in most cases, the strongest correlations associated with surface areas. The magnitude of those correlations was up to 44% in terms of R^2, whereas vine canopy volume and vegetation volume ($Volume_v$ and $Volume_{vc}$) have reached 51%. Except for the June 2015 flight, no significant correlation was noted between vegetation and canopy height (h_v and h_{vc}) versus LAI. Projected areas ($Area_v$ and $Area_{vc}$) are related to fractional cover, and fractional cover is nonlinearly related to LAI. Table 3.3 shows that the correlation between projected area, specifically vine canopy projected areas ($Area_{vc}$), and LAI is comparable with volume information. In addition, results revealed that NIR and Tr bands, and consequently indices utilizing these two bands, have the potential to be used for LAI prediction for late vine growth stage.

Concerning the buffer shapes (square or rectangular) around LAI measurements, Table 3.3 shows that the correlation between spectral information and LAI is insensitive to the shape of the buffer, which means that the average values of spectral information in both grid sizes are close to each other. In contrast, changing the buffer grids from the rectangular to the square shape, in most cases, improves R^2. For example, in the June 2015 flight at the Landsat time overpass (10:43 a.m.), $Volume_v$, $Volume_{vc}$, and $SArea_{vc}$'s R^2 doubled (16% to 38%, 15% to 36%, and 11% to 25%, respectively). Although the improvement in R^2 with buffer shape change is not significant, VSSIXA-I's performance appears to be more sensitive to the buffer shape. When VSSIXA-I is used along with the square buffer, the chance of ground point detection increases and may lead to improvements in the estimation of structural information. In other words, if narrower buffers are occupied by vine, VSSIXA-

I considers the lowest height values of the vine canopy as the ground points, leading to a bias in structural information, particularly in vegetation and vine volumes ($Volume_v$ and $Volume_{vc}$).

Table 3.3: R^2 calculated between VSSIXA outputs and in situ LAI measurements for 2014, 2015, and 2016 UAV flights over Sierra Loma.

		UAV bands						Sepctral infromation of vegetation					Structrual infromation of vegetation				Sepctral infromation of vine canopy					Structrual infromation of vine canopy			
Date	VSSIXA & buffer type	R	G	B	N	NDVI	Tr	R_v	G_v	B_v	N_v	$NDVI_v$	h_v	$Volume_v$	$SArea_v$	$Area_v$	R_{vc}	G_{vc}	B_{vc}	N_{vc}	$NDVI_{vc}$	h_{vc}	$Volume_{vc}$	$SArea_{vc}$	$Area_{vc}$
20140809 10:41 AM	I, Rectangle	17%	7%	7%	7%	28%	23%	0%	0%	0%	0%	0%	2%	1%	4%	12%	0%	0%	0%	0%	0%	2%	1%	1%	8%
	I, Square	18%	10%	10%	10%	34%	31%	4%	14%	26%	26%	9%	0%	12%	13%	41%	4%	15%	27%	27%	11%	1%	14%	11%	45%
	II, Rectangle	17%	7%	7%	7%	28%	23%	0%	4%	5%	5%	8%	9%	36%	17%	41%	0%	2%	5%	5%	2%	0%	34%	20%	40%
	II, Square	18%	10%	10%	10%	34%	31%	4%	14%	25%	25%	9%	11%	42%	26%	41%	1%	9%	17%	17%	10%	6%	43%	37%	45%
20150602 10:43 AM	I, Rectangle	10%	6%	14%	38%	18%	43%	6%	13%	2%	38%	1%	5%	16%	6%	18%	1%	4%	0%	25%	2%	1%	15%	11%	27%
	I, Square	13%	10%	18%	33%	17%	46%	2%	8%	0%	46%	11%	21%	38%	9%	16%	0%	1%	4%	31%	9%	13%	36%	25%	31%
	II, Rectangle	10%	6%	14%	38%	18%	43%	1%	0%	1%	7%	1%	33%	39%	7%	11%	0%	1%	2%	1%	1%	23%	41%	29%	34%
	II, Square	13%	10%	18%	33%	17%	46%	1%	6%	1%	43%	11%	44%	50%	19%	18%	0%	0%	6%	24%	6%	37%	51%	44%	45%
20150602 14:07 PM	I, Rectangle	18%	14%	22%	No NIR Band		43%	8%	3%	6%	No NIR Band		10%	19%	5%	1%	2%	1%	2%	No NIR Band		3%	22%	18%	21%
	I, Square	12%	10%	17%			41%	9%	5%	14%			29%	34%	5%	2%	10%	6%	14%			30%	30%	10%	10%
	II, Rectangle	18%	14%	22%			43%	8%	4%	13%			31%	40%	19%	15%	2%	1%	7%			25%	40%	28%	37%
	II, Square	12%	10%	17%			41%	8%	4%	13%			35%	40%	15%	8%	2%	0%	7%			28%	41%	29%	31%
20170711 10:35 AM	I, Rectangle	20%	14%	14%	31%	33%	6%	1%	1%	0%	28%	23%	5%	23%	33%	32%	2%	0%	0%	27%	20%	7%	20%	25%	23%
	I, Square	19%	14%	14%	27%	35%	9%	0%	1%	1%	28%	23%	10%	32%	33%	31%	1%	0%	0%	26%	19%	11%	32%	33%	33%
	II, Rectangle	20%	14%	14%	31%	33%	6%	1%	1%	0%	28%	23%	8%	28%	36%	31%	1%	0%	0%	26%	21%	11%	26%	34%	25%
	II, Square	19%	14%	14%	27%	35%	9%	0%	1%	1%	28%	23%	8%	30%	35%	31%	1%	0%	0%	25%	23%	13%	30%	34%	26%
20150711 14:14 PM	I, Rectangle	23%	19%	19%	No NIR Band		9%	5%	1%	2%	No NIR Band		5%	23%	33%	32%	8%	1%	2%	No NIR Band		7%	20%	25%	23%
	I, Square	24%	20%	20%			12%	7%	1%	2%			10%	32%	33%	31%	8%	1%	2%			11%	32%	33%	33%
	II, Rectangle	23%	19%	19%			9%	5%	0%	2%			8%	28%	36%	31%	6%	0%	1%			11%	26%	34%	25%
	II, Square	24%	20%	20%			12%	7%	1%	2%			8%	30%	35%	31%	8%	1%	1%			13%	30%	34%	26%
20160502 12:05 AM	I, Rectangle	1%	No G and B Bands		0%	0%	12%	1%	No G and B Bands		1%	2%	17%	26%	21%	18%	0%	No G and B Bands		1%	3%	13%	26%	26%	22%
	I, Square	4%			1%	3%	8%	0%			0%	0%	15%	22%	9%	6%	0%			0%	0%	7%	23%	20%	20%
	II, Rectangle	1%			0%	0%	12%	0%			0%	0%	9%	8%	12%	3%	2%			1%	3%	3%	7%	15%	4%
	II, Square	4%			1%	3%	8%	0%			4%	1%	9%	11%	8%	5%	2%			0%	1%	3%	12%	19%	12%

R= Average of UAV Red band
G= Average of UAV Green band
B= Average of UAV Blue band
N= Average of UAV NIR band
Tr= Average of UAV thermal band

R_v = Average of R for vegetation
G_v =Average of G for vegetation
B_v = Average of B for vegetation
N_v = Average of N for vegetation
$NDVI_v$ = Average of NDVI for vegetation

h_v = Average of vegetation heights
$Volume_v$ = Volume of vegetation
$SArea_v$ = Surface area of vegetation
$Area_v$ = projected of SArea_V

R_{vc} = Average of R for vine canopy
G_{vc} =Average of G for vine canopy
B_{vc} = Average of B for vine canopy
N_{vc} = Average of N for vine canopy
$NDVI_{vc}$ = Average of NDVI for vine canopy

h_{vc} = Average of vine canopy height
$Volume_{vc}$ = Volume of vine canopy
$SArea_{vc}$ = Surface area of vine canopy
$Area_{vc}$ = projected of SArea_VC

Color Range: 0% 5% 8% 10% 15% 20% 25% 30% 40% 50%

Regarding VSSIXA-I and VSSIXA-II performances, since VSSIXA-II takes advantage of a more accurate ground point dataset (LiDAR ground data), it provides a more accurate estimation of structural information. Except for the May 2016 flight, volumes, surface areas, and projected surface areas calculated by VSSIXA-II are more correlated to in situ LAI. Our preliminary investigation on 2016 ground points extracted by the point cloud and LiDAR data shows that ground point cloud data are significantly lower than LiDAR data, which could be due to generating the point cloud using only two bands (R and NIR) compared to 2014 and 2015 point cloud data generated by four bands (R, G, B, and NIR).

3.4.4 Modeled LAI with Machine Learning Algorithms

Although VSSIXA-II outputs with the square buffers, in general, show higher correlations in terms of R^2, this statistical analysis shows that a simple linear regression model cannot lead to an accurate LAI model across different vine growth stages, and exploring the ability of sophisticated algorithms such as machine learning techniques becomes necessary in modeling LAI. Machine learning techniques are not as simple as the regression models, but they can explore both linear and nonlinear relationships between output and several inputs through training and testing procedures that minimize error functions. Here, GP is employed to model LAI, exploring linear and nonlinear fitting curves between VSSIXA-II outputs extracted in square buffer domains. To remove the dependency of GP LAI models to the grid size, structural information (such as canopy volume and surface area) was divided by the area of the square grid (3.6 $\times$ 3.6 m). To evaluate the importance of structural information in modeled LAI, three different scenarios were defined, including LAI models with only spectral information (Model 1), with only structural information (Model 2), and with both spectral and structural information (Model 3). According to Table 3.3, N, NDVI, Tr, N_v, and N_{vc} are the main inputs in Model 1. In Model 2, $Volume_v$, $SArea_v$, $Area_v$, $Volume_{vc}$, $SArea_{vc}$, and $Area_{vc}$ are considered as the main descriptors for the LAI model. In Model 3, a combination of Model 1 and Model 2 inputs are used to train GP and create the LAI map. Figure 3.15 and Table 3.4 show the results of the LAI modeled by GP and $\sim$310 LAI measurements in the 2014, 2015, and 2016 flights, except for those lacking NIR

or R bands.

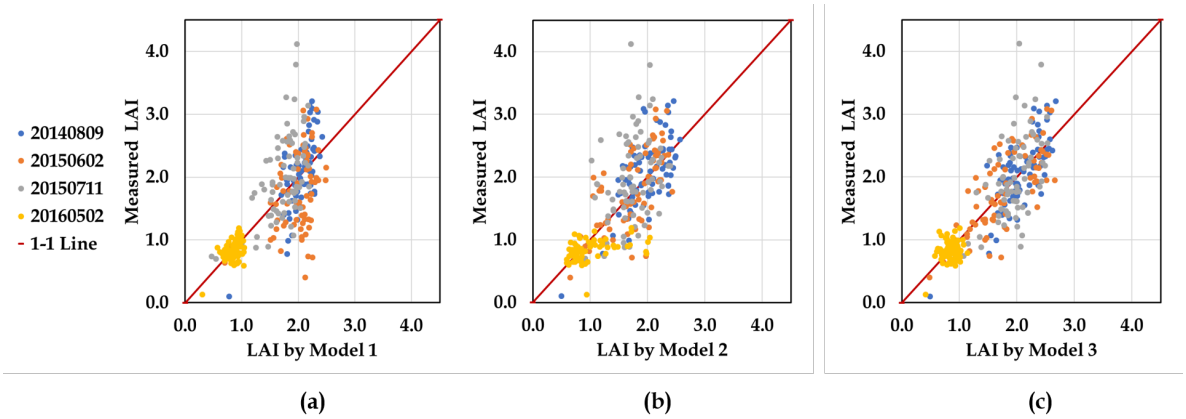

Fig. 3.15: In situ LAI measurements versus modeled LAIs by GP based on Model 1 (**a**), Model 2 (**b**), and Model 3 (**c**).

Table 3.4: Performance of the Models 1, 2 and 3.

Stats	**Model 1**	**Model 2**	**Model 3**
R^2	0.56	0.54	0.70
MAE	0.35	0.37	0.30
RMSE	0.43	0.44	0.32
RRMSE	25%	26%	19%

As shown in Figure 3.15 and Table 3.4, employing GP with both spectral and structural information (Model 3) can significantly increase the accuracy of modeled LAI up to 70% in terms of R^2 and enhance the performance of the models from fair to good (RRMSE of Model 1 and Model 2 $< 30\%$ compared to RRMSE of Model 3 $< 20\%$). Despite flight time and vine phenological stage, GP was able to produce a reliable model if both spectral and structural information are provided. Equations (3.13)–(3.15) show the relationship between inputs and outputs found by GP for Models 1, 2, and 3, respectively:

$$LAI_1 = 5.85 + 17.37 \times N \times N_v + 0.85 \times NDVI \times Tr \\ -0.52 \times Tr - 8.51 \times N_{vc}^2 - 14.96 \times NDVI^2, \tag{3.13}$$

$$LAI_2 = 0.47 + 2.39 \times Area_{vc} - 2.29 \times Area_{vc} \times Area_v^{0.41 \times 43.07^{Volume_v}}, \tag{3.14}$$

$$LAI_3 = 2.69 \times N \times Volume_{vc} + 0.11 \times Tr \times Area_v + \\ -0.67 \times \frac{Area_v}{N_{vc}} - 0.38 \times 1.54^{Tr} \times N^2 \times NDVI^{26.92} \times \frac{N_{vc}^4}{Volume_{vc}}. \tag{3.15}$$

The unit of Tr in Equations (3.13)–(3.15) is Celsius degree, and the unit of structural parameters is m as they are divided by the area of the square grids (m^3/m^2).

3.4.5 TSEB-2T Model versus Eddy Covariance Measurements

To evaluate the importance of point cloud data on the TSEB model, three different scenarios are defined. In scenario 1 (the spectral-based scenario, S1), the LAI map is created with GP Model 1. Canopy height (h_{vc}), fractional cover (f_c), and canopy width (w_c) are set to fixed values. In scenario 2 (the structural-based scenario, S2), GP Model 2 is used to create the LAI map. h_{vc}, f_c (vine projected surface area/the grid area), and w_c maps ($3.35 f_c$ [67]) are estimated by VSSIXA outputs instead of the fixed values used in S1. In Scenario 3 (the spectral-structural-based scenario, S3), the LAI map is created using GP Model 3 and other TSEB inputs the same as S2 (Table 3.5). Considering these three scenarios, the results of the modeled flux components by TSEB (Rn, LE, H, and G) are compared with the surface energy balance measurements from the Eddy Covariance flux tower footprints.

Table 3.5: TSEB Inputs for each scenario.

Scenario	**LAI**	h_{vc} **(Canopy Height)**	f_c **(Fractional Cover)**	w_c **(Canopy Width)**
S1: Spectral-based	GP Model 1	a fixed value	a fixed value	a fixed value
S2: Structural-based	GP Model 2	estimated by VSSIXA	estimated by VSSIXA	$= 3.35 * f_c$
S3: Spectral-Structural-based	GP Model 3	estimated by VSSIXA	estimated by VSSIXA	$= 3.35 * f_c$

To create LAI maps for each scenario at the TSEB resolution, VSIXXA-II with the square buffer is employed to extract spectral and structural information from the 2014, 2015, and 2016 flights. Next, LAI maps for each flight are created based on Models 1, 2 and 3. Due to the computation time of VSSIXA discussed in Section 3.4.2, VSSIXA-II is executed only for the flux tower footprints. As shown in Figure 3.1, the study area includes two flux towers, the footprint of each tower contains $\sim$ 2500 3.6-m grids that requires $\sim$ 24 h (2500 $\times$ 40 s/3600 s) to process. The footprint of the flux tower is produced using a method presented by [48].

The results of the TSEB model compared to the eddy covariance measurements are shown in Figure 3.16 and Table 3.6.

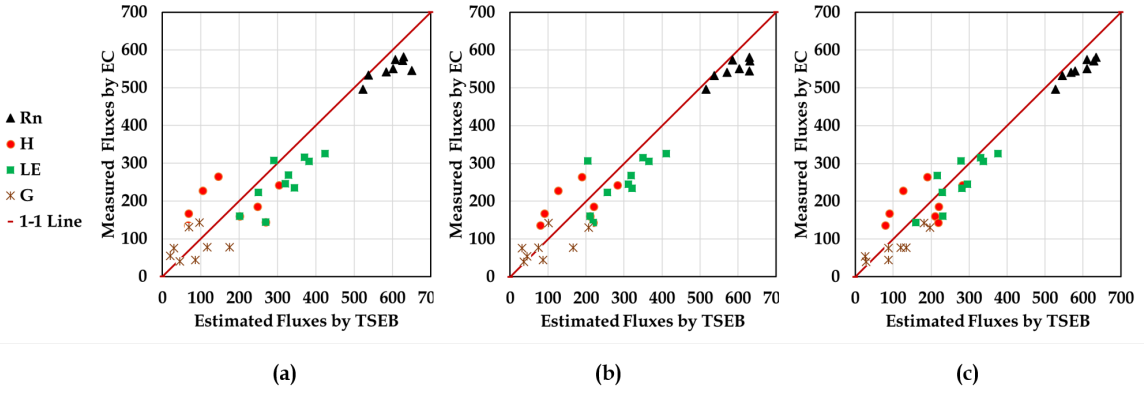

Fig. 3.16: Scatterplot of observed vs. predicted fluxes using the different scenarios. (**a**) S1: LAI Model 1 and fixed values for h_{vc}, f_c, w_c (**b**) S2: LAI Model 2 with the map of h_{vc}, f_c, w_c (**c**) S3 : LAI Model 3 with the map of h_{vc}, f_c, w_c. All fluxes are in W/m^2.

Table 3.6: Performance of the TSEB model based on GP model estimate of LAI using model scenarios 1, 2, and 3 (S1, S2 and S3) for each energy flux component.

Variable	**Scenario**	**MAE**	**RMSE**	**RRMSE**
Rn	S1	46	53	10%
	S2	39	47	8%
	S3	39	42	8%
H	S1	87	93	49%
	S2	64	67	35%
	S3	35	40	21%
LE	S1	65	72	26%
	S2	65	69	25%
	S3	35	39	14%
G	S1	46	52	65%
	S2	38	49	61%
	S3	37	41	51%

Figure 3.16 shows the agreement between TSEB model outputs versus eddy covariance measurements for each scenarios. Each subplot contains 32 pairs of estimated and observed energy fluxes (4 flights $\times$ 2 eddy covariance $\times$ 4 fluxes). From Figure 3.16, the agreement between modeled and observed fluxes improves going from using as LAI input GP Model 1 (S1) to GP Model 3 (S3), with the most significant improvement using S3 versus S1. Since differences between the performance of TSEB using GP Model 1 versus GP Model 2 for estimating LAI was not significant (Figure 3.16 and Table 3.6), it is likely that the improvement is mainly attributed to the use of a spatially-distributed map of the fractional cover, canopy height, and canopy width instead of using a fixed value. Using the spatially-distributed maps of the fractional cover, canopy height, and canopy width appears to have the largest effect on modeled H, with marginal impact on Rn, G, and LE. Comparing TSEB

model results using S3 versus S2 and S1 reveals how a more accurate LAI map can affect the TSEB model output, particularly H and LE. The differences between TSEB output using S3 versus S2 illustrates the impact of the LAI maps, as the only difference between these two scenarios is related to the estimated LAI (LAI_2 via Equation (3.13) and LAI_3 via Equation (3.14)). According to Table 3.6, using GP Model 3 estimates of LAI in the TSEB model yields the best agreement with the observed H and LE fluxes. In terms of the RRMSE statistic for accuracy or performance of the TSEB model changes from "fair" to "good" rating for LE and "poor" to "fair" rating for H (i.e., poor rating is if RRMSE $> 30\%$, fair rating if RRMSE $< 30\%$, and a good rating if RRMSE $< 20\%$). For Rn, all three GP model inputs of LAI produce an RRMSE value with "excellent" accuracy rating. On the other hand, the RRMSE value for G using all three GP models results in a "poor" rating. This "poor" performance is due in part to the assumption that G is a simple fraction of modeled soil net radiation (e.g., $G = 0.30Rn_s$), but also the large spatial and temporal variability in measured G due to a nonuniform vine canopy cover [6] and the fact that the source area/flux footprint contributing to the tower fluxes and the area used in aggregating the TSEB model flux output is much greater than the sampling area used for the flux tower.

3.5 Discussion

In this study, a new algorithm, called VSSIXA, is developed to extract canopy spectral and structural information from multi-spectral UAV imagery and point cloud data. Although the computation time of VSSIXA is long (40 s for each 3.6-m grid), several aspects of this algorithm make it an efficient tool for improving remote sensing-based ET models, particularly the TSEB model. First, VSSIXA is able to separately extract vine canopy and cover crop canopy spectral and structural information, which cannot be achieved with solely spectral information. In other words, at the early phenological stage of the vine (April, May), when the presence of the cover crop is dominant, the spectral-based analysis cannot assign a unique class for vine and cover crop classes separately as their spectral responses are similar to one another. However, the structural information, particularly canopy height, can be an efficient measure for separation. This feature of VSSIXA can be

useful for partitioning total flux into vine and interrow flux. Second, although vegetation indices (such as NDVI) are popular and well-known inputs for modeling LAI, these indices by themselves cannot fully describe the variability in LAI when the amount of active cover crop in the inter row is significant [67]. Therefore, 3D structural metrics can be used as other sources of information to derive spatial maps of LAI. The dominancy of the cover crop is more pronounced in the flights in May 2016 in which the active cover crop was present. In addition, several studies have indicated that satellite or UAV-derived LAI solely based on VIs may lead to the saturation situation that occurs within the relationship between VIs and LAI for well-developed canopies [2, 12, 25, 78]. The saturation issue resulted from modeling a non-scaled parameter, namely LAI using scaled parameters such as VIs. However, as VSSIXA computed non-scaled structural metrics such as canopy height, surface area, and volume, the saturation issue does not occur in LAI estimated by Model 2 and Model 3, whereas most LAI values estimated by Model 1 ranged between 1 and 2 (Figure 3.15). Third, this study showed that, compared to using fixed-values, spatially-distributed structural metrics such as hvc, f_c, and w_c can be more effective. However, a question may arise on how canopy structural properties can be re-generated or integrated into satellite imageries for estimation of daily canopy properties when no point cloud data exist for that coarse of pixel resolution or even for other dates. One approach is to fit empirical curves between in situ LAI values collected during different canopy phenological stages (bloom to harvest, Table 3.2) and structural information estimated by VSSIXA. Next, Landsat LAI obtained by fusing the MODIS LAI (MCD15A3H) product and Landsat surface reflectance [34, 35] are trained with upscale structural canopy parameters (e.g., Landsat LAI vs. hvc at 30-m resolution). Ultimately, for each of the Landsat LAI products, spatially-distributed maps of canopy structural information at the satellite scale can be estimated based on satellite LAI products [66].

Although sensitivity analysis of canopy 3D metrics in remote sensing-based ET models, and particularly the TSEB model, require a further investigation, the authors in [89] performed a sensitivity analysis of the vegetation structural information (hc, LAI, fc, etc.)

that is used in estimating soil resistance to heat transfer in sparse semiarid stands. Their results showed that the turbulent bulk heat transfer model for the sensible heat flux was sensitive to variations in crop height. The authors in [11]) conducted a simple model sensitivity analysis of TSEB to LAI and found that a variation on the LAI value of 30% would increase the final TSEB model error on a range of 4% and 7%. Thus, an error in LAI could significantly impact the accuracy of ET [18], which is compatible with the results presented in this study (decreasing LE from 72 (S2) to 39 (s3) in terms of RMSE). Generally, in the TSEB model, LAI is a key input for partitioning Tr into Ts and Tc and canopy and soil net radiation.

In TSEB-2T, the selection criterion for determining bare soil/cover crop stubble NDVI is based on the empirical relationship between NDVI and LAI [67]. In other words, $NDVI_S$ in Figure 3.13 corresponds to the extrapolation of the NDVI-LAI curve for $LAI = 0$. Moreover, the spatial map of LAI is an input in the canopy radiative transfer model [17] to estimate soil and canopy net radiation (Equations (3.3)–(3.6)). Therefore, the partitioning of Rn between Rn_s and Rn_c is controlled by the LAI estimates. These equations (Equations (3.3) and (3.4)) indicate how and why the temporal trend in transpiration of the canopy (LE_C) over LE follows the temporal variation in LAI [52]. In addition, LAI is inversely related to the boundary layer resistance of the canopy of leaves (Equation (3.16)):

$$R_x = \frac{C}{LAI} \times (\frac{l_w}{U_{d_0+Z_{0m}}}), \tag{3.16}$$

in which d_0 is the zero-plane displacement height, and z_{0M} is the roughness length for momentum. C is assumed to be $90\frac{s^{\frac{1}{2}}}{m}$, and l_w is the average leaf width (m). Equation (3.16) indicates that overestimation of LAI leads to underestimation of R_x then overestimation of H_c and possibly an overestimation of H assuming a relatively small change in H_s ($H = H_s + H_c$). As LE is calculated as a residual term of the land surface energy balance ($LE = R_n - G - H$), a lower R_x likely yields lower LE, assuming R_n and G are not highly sensitive to LAI.

In addition to relating LAI to NDVI thresholds of vegetation and bare soil/cover crop

stubble, partitioning Rn into Rn_s and Rn_c and the boundary layer resistance of the canopy in the TSEB model, LAI is used to indirectly (through the partitioning of Rn into Rn_s and Rn_c) estimate G via the expression $G = 0.3Rn_s$. This resulted in estimated G from TSEB to be in relatively poor agreement with observed G (see Table 3.6). However, modifications to this simple expression have been proposed (Nieto et al. [67]), which considers empirically the effect of the cover crop on G.

3.6 Conclusions

This paper explored the utility of incorporating UAV point cloud products into the remote sensing-based TSEB model. A new algorithm called VSSIXA in Python and ArcGIS Pro was developed to extract both spectral and structural information for a vineyard. VSSIXA is developed in two modes, VSSIXA-I and VSSIXA-II. VSSIXA-I only requires point cloud data to calculate vegetation structural information, while VSSIXA-II requires a precise and separate ground point data (e.g., LiDAR data). In this study, both versions of VSSIXA along with different buffer shapes around in situ LAI measurements are employed to create LAI maps. Three different estimates of LAI using Genetic Programming (GP) machine learning are considered to evaluate the impact of structural information for computing LAI. First, results indicated that VSSIXA-II with wider buffers is more efficient for calculating vegetation structural information. Among the three GP-based models for estimating LAI, Model scenario 1 (S1) and Model scenario 2 (S2), which require only spectral and structural information, respectively, had similar performance, while Model scenario 3 (S3), which takes advantage of both spectral and structural information, could estimate LAI with 70% accuracy in terms of R^2.

To assess the impact of the structural information in modeling fluxes, the remote sensing-based TSEB model was applied using the three LAI modeling scenarios, S1–S3 and using fixed values versus a spatially-distributed map of canopy height, width, and fractional cover. The TSEB model output of the fluxes using derived soil and canopy temperatures (TSEB-2T), which avoids the need for the Priestley–Taylor assumption for canopy transpiration, are compared with eddy covariance flux tower measurements. Results

indicated that significant improvement in the agreement of modeled output with the flux tower observations is achieved by using a reliable LAI map, more so than a map of spatially-distributed canopy structure parameters. The statistical results suggest that a more robust LAI map derived from both spectral and structural information can lead to significant improvement in TSEB model performance in estimating the turbulent fluxes H and LE. There was much less of an impact from the three different model estimates of LAI in TSEB output of Rn and G. In particular, the relatively poor performance rating given by the RRMSE statistic for G has to do with both the simple model assumption that G is a constant fraction of Rn_s and the significant spatial and temporal variation in individual G measurements observed by [6]. Improvements on this simple formulation for estimating G have been proposed by Nieto et al. [67].

Bibliography

[1] Aboutalebi, M.; Allen, L.N.; Torres-Rua, A.F.; McKee, M.; Coopmans, C. "Estimation of soil moisture at different soil levels using machine learning techniques and unmanned aerial vehicle (UAV) multispectral imagery". In Proceedings of the Autonomous Air and Ground Sensing Systems for Agricultural Optimization and Phenotyping IV, Baltimore, MD, USA, 14–18 April 2019; Volume 11008.

[2] Aboutalebi, M.; Torres-Rua, A.F.; Allen, N. "Multispectral remote sensing for yield estimation using high-resolution imagery from an unmanned aerial vehicle". In Proceedings of the Autonomous Air and Ground Sensing Systems for Agricultural Optimization and Phenotyping III, Orlando, FL, USA, 15–19 April 2018; Volume 10664.

[3] Aboutalebi, M.; Torres-Rua, A.F.; Kustas, W.P.; Nieto, H.; Coopmans, C.; McKee, M. "Assessment of different methods for shadow detection in high-resolution optical imagery and evaluation of shadow impact on calculation of NDVI, and evapotranspiration".*Irrig. Sci.* **2019**, *37*, 407–429.

[4] Aboutalebi, M.; Torres-Rua, A.F.; McKee, M.; Kustas, W.; Nieto, H.; Coopmans, C. "Validation of digital surface models (DSMs) retrieved from unmanned aerial vehicle (UAV) point clouds using geometrical information from shadows". In Proceedings of the Autonomous Air and Ground Sensing Systems for Agricultural Optimization and Phenotyping IV, Baltimore, MD, USA, 14–18 April 2019; Volume 11008.

[5] Aboutalebi, M.; Torres-Rua, A.F.; McKee, M.; Nieto, H.; Kustas, W.P.; Prueger, J.H.; McKee, L.; Alfieri, J.G.; Hipps, L.; Coopmans, C. "Assessment of Landsat Harmonized sUAS Reflectance Products Using Point Spread Function (PSF) on Vegetation Indices (VIs) and Evapotranspiration (ET) Using the Two-Source Energy Balance (TSEB) Model". *AGU Fall Meet. Abstr.* **2018**.

[6] Agam, N.; Kustas, W.P.; Alfieri, J.G.; Gao, F.; McKee, L.M.; Prueger, J.H.; Hipps, L.E. "Micro-scale spatial variability in soil heat flux (SHF) in a wine-grape vineyard". *Irrig. Sci.* **2019**, *37*, 253–268.

[7] `https://uwrl.usu.edu/aggieair/`

[8] Agisoft, L.L.; St Petersburg, R. *Agisoft Photoscan*; Professional ed.; 2014.

[9] Amrullah, C.; Suwardhi, D.; Meilano, I. "Product Accuracy Effect of Oblique and Vertical Non-Metric Digital Camera Utilization in Uav-Photogrammetry to Determine Fault Plane". *ISPRS Ann. Photogramm. Remote Sens. Spat. Inf. Sci.* **2016**, *III-6*, 41–48.

[10] Anderson, M.C.; Norman, J.M.; Kustas, W.P.; Li, F.; Prueger, J.H.; Mecikalski, J.R. "Effects of Vegetation Clumping on Two–Source Model Estimates of Surface Energy Fluxes from an Agricultural Landscape during SMACEX". *J. Hydrometeorol.* **2005**, *6*, 892–909.

[11] Andreu, A.; Kustas, W.P.; Polo, M.J.; Carrara, A.; González-Dugo, M.P. "Modeling Surface Energy Fluxes over a Dehesa (Oak Savanna) Ecosystem Using a Thermal Based Two-Source Energy Balance Model (TSEB)". *Remote Sens.* **2018**, *10*, 567.

[12] Asrar, G.; Fuchs, M.; Kanemasu, E.T.; Hatfield, J.L. "Estimating Absorbed Photosynthetic Radiation and Leaf Area Index from Spectral Reflectance in Wheat". *Agron. J.* **1989**, *76*, 300–306.

[13] Bendig, J.; Bolten, A.; Bennertz, S.; Broscheit, J.; Eichfuss, S.; Bareth, G. "Estimating Biomass of Barley Using Crop Surface Models (CSMs) Derived from UAV-Based RGB Imaging". *Remote Sens.* **2014**, *6*, 10395–10412.

[14] Bendig, J.; Willkomm, M.; Tilly, N.; Gnyp, M.L.; Bennertz, S.; Qiang, C.; Miao, Y.; Lenz-Wiedemann, V.I.S.; Bareth, G. "Very high resolution crop surface models (CSMs) from UAV-based stereo images for rice growth monitoring In Northeast

China". *ISPRS-Int. Arch. Photogramm. Remote Sens. Spat. Inf. Sci.* **2013**, *XL-1/W2*, 45–50.

[15] Bendig, J.; Yu, K.; Aasen, H.; Bolten, A.; Bennertz, S.; Broscheit, J.; Gnyp, M.L.; Bareth, G. "Combining UAV-based plant height from crop surface models, visible, and near infrared vegetation indices for biomass monitoring in barley". *Int. J. Appl. Earth Obs. Geoinf.* **2015**, *39*, 79–87.

[16] Calera, A.; Martínez, C.; Melia, J. "A procedure for obtaining green plant cover: Relation to NDVI in a case study for barley". *Int. J. Remote Sens.* **2001**, *22*, 3357–3362".

[17] Campbell, G.; Norman, J. "An Introduction to Environmental Biophysics"; Modern Acoustics and Signal; Springer: New York, NY, USA, 2000.

[18] Chávez, J.L.; Gowda, P.H.; Howell, T.A.; Neale, C.M.U.; Copeland, K.S. "Estimating hourly crop ET using a two-source energy balance model and multispectral airborne imagery". *Irrig. Sci.* **2009**, *28*, 79–91.

[19] Colaizzi, P.D.; Kustas, W.P.; Anderson, M.C.; Agam, N.; Tolk, J.A.; Evett, S.R.; Howell, T.A.; Gowda, P.H.; O'Shaughnessy, S.A. "Two-source energy balance model estimates of evapotranspiration using component and composite surface temperatures". *Adv. Water Resour.* **2012**, *50*, 134–151.

[20] Comba, L.; Biglia, A.; Aimonino, D.R.; Gay, P. "Unsupervised detection of vineyards by 3D point-cloud UAV photogrammetry for precision agriculture". *Comput. Electron. Agric.* **2018**, *155*, 84–95.

[21] Cook, B.; Corp, L.W.; Nelson, R.F.; Middleton, E.M.; Morton, D.C.; McCorkel, J.T.; Masek, J.G.; Ranson, K.J.; Ly, V.; Montesano, P.M. "NASA Goddard's Lidar, Hyperspectral and Thermal (G-LiHT) airborne imager". *Remote Sens.* **2013**, *5*, 4045–4066.

[22] Crowther, B. "Radiometric Calibration of Multispectral Video Imagery". Ph.D. Thesis, Utah State University, Logan, UT, USA, 1992.

[23] Dandois, J.P.; Olano, M.; Ellis, E.C. "Optimal Altitude, Overlap, and Weather Conditions for Computer Vision UAV Estimates of Forest Structure". *Remote Sens.* **2015**, *7*, 13895–13920.

[24] Despotovic, M.; Nedic, V.; Despotovic, D.; Cvetanovic, S. "Evaluation of empirical models for predicting monthly mean horizontal diffuse solar radiation". *Renew. Sustain. Energy Rev.* **2016**, *56*, 246–260.

[25] Diarra, A.; Jarlan, L.; Er-Raki, S.; Page, M.L.; Aouade, G.; Tavernier, A.; Boulet, G.; Ezzahar, J.; Merlin, O.; Khabba, S. "Performance of the two-source energy budget (TSEB) model for the monitoring of evapotranspiration over irrigated annual crops in North Africa".*Agric. Water Manag.* **2017**, *193*, 71–88.

[26] Díaz-Varela, R.A.; De la Rosa, R.; León, L.; Zarco-Tejada, P.J. "High-Resolution Airborne UAV Imagery to Assess Olive Tree Crown Parameters Using 3D Photo Reconstruction: Application in Breeding Trials".*Remote Sens.* **2015**, *7*, 4213–4232.

[27] Du, M.; Noguchi, N. "Monitoring of Wheat Growth Status and Mapping of Wheat Yield's within-Field Spatial Variations Using Color Images Acquired from UAV-camera System". *Remote Sens.* **2017**, *9*, 289.

[28] Duan, T.; Zheng, B.; Guo, W.; Ninomiya, S.; Guo, Y.; Chapman, S.C. "Comparison of ground cover estimates from experiment plots in cotton, sorghum and sugarcane based on images and ortho-mosaics captured by UAV". *Funct. Plant Biol.* **2017**, *44*, 169–183.

[29] Elarab, M.; Ticlavilca, A.M.; Torres-Rua, A.F.; Maslova, I.; McKee, M. "Estimating chlorophyll with thermal and broadband multispectral high resolution imagery from an unmanned aerial system using relevance vector machines for precision agriculture". *Int. J. Appl. Earth Obs. Geoinf.* **2015**, *43*, 32–42.

[30] Frank, J.M.; Massman, W.J.; Ewers, B.E. "Underestimates of sensible heat flux due to vertical velocity measurement errors in non-orthogonal sonic anemometers". *Agric. For. Meteorol.* **2013**, *171–172*, 72–81.

[31] Foken, T. "The Energy Balance Closure Problem: An Overview". *Ecol. Appl.* **2008**, *18*, 1351–1367.

[32] Frank, J.M.; Massman, W.J.; Ewers, B.E. "A Bayesian model to correct underestimated 3-D wind speeds from sonic anemometers increases turbulent components of the surface energy balance". *Atmos. Meas. Tech.* **2016**, *9*, 5933–5953.

[33] Fraser, R.H.; Olthof, I.; Lantz, T.C.; Schmitt, C. "UAV photogrammetry for mapping vegetation in the low-Arctic". *Arct. Sci.* **2016**, *2*, 79–102.

[34] Gao, F.; Anderson, M.C.; Kustas, W.P.; Houborg, R. "Retrieving Leaf Area Index From Landsat Using MODIS LAI Products and Field Measurements". *IEEE Geosci. Remote Sens. Lett.* **2014**, *11*, 773–777.

[35] Gao, F.; Kustas, W.P.; Anderson, M.C. "A Data Mining Approach for Sharpening Thermal Satellite Imagery over Land". *Remote Sens.* **2012**, *4*, 3287–3319.

[36] Garousi-Nejad, I.; Tarboton, D.; Aboutalebi, M.; Torres-Rua, A. "Terrain Analysis Enhancements to the Height Above Nearest Drainage Flood Inundation Mapping Method". *Water Resour. Res.* **2019**, *55*, 7983—8009

[37] Gitelson, A.A.; Viña, A.; Arkebauer, T.J.; Rundquist, D.C.; Keydan, G.; Leavitt, B. "Remote estimation of leaf area index and green leaf biomass in maize canopies". *Geophys. Res. Lett.* **2003**, *30*.

[38] Hassan-Esfahani, L.; Torres-Rua, A.; Jensen, A.; McKee, M. "Assessment of Surface Soil Moisture Using High-Resolution Multi-Spectral Imagery and Artificial Neural Networks". *Remote Sens.* **2015**, *7*, 2627–2646.

[39] Holman, F.H.; Riche, A.B.; Michalski, A.; Castle, M.; Wooster, M.J.; Hawkesford, M.J. "High Throughput Field Phenotyping of Wheat Plant Height and Growth Rate in Field Plot Trials Using UAV Based Remote Sensing". *Remote Sens.* **2016**, *8*, 1031.

[40] Honkavaara, E.; Kaivosoja, J.; Mäkynen, J.; Pellikka, I.; Pesonen, L.; Saari, H.; Salo, H.; Hakala, T.; Marklelin, L.; Rosnell, T. "Hyperspectral Reflectance Signatures and Point Clouds for Precision Agriculture by Light Weight Uav Imaging System". *ISPRS Ann. Photogramm. Remote Sens. Spat. Inf. Sci.* **2012**, *I-7*, 353–358.

[41] Horst, T.W.; Semmer, S.R.; Maclean, G. "Correction of a Non-orthogonal, Three-Component Sonic Anemometer for Flow Distortion by Transducer Shadowing". *Bound.-Layer Meteorol.* **2015**, *155*, 371–395.

[42] Hu, X.; Zhang, Z.; Duan, Y.; Zhang, Y.; Zhu, J.; Long, H. "Lidar Photogrammetry and Its Data Organization". *ISPRS-Int. Arch. Photogramm. Remote Sens. Spat. Inf. Sci.* **2011**, *XXXVIII-5/W12*, 181–184".

[43] Jaud, M.; Passot, S.; Le Bivic, R.; Delacourt, C.; Grandjean, P.; Le Dantec, N. "Assessing the Accuracy of High Resolution Digital Surface Models Computed by PhotoScan® and MicMac® in Sub-Optimal Survey Conditions". *Remote Sens.* **2016**, *8*, 465.

[44] Jensen, J.L.R.; Mathews, A.J. "Assessment of Image-Based Point Cloud Products to Generate a Bare Earth Surface and Estimate Canopy Heights in a Woodland Ecosystem". *Remote Sens.* **2016**, *8*, 50.

[45] Jiménez-Bello, M.A.; Royuela, A.; Manzano, J.; Zarco-Tejada, P.J.; Intrigliolo, D. "Assessment of drip irrigation sub-units using airborne thermal imagery acquired with an Unmanned Aerial Vehicle (UAV)".In *Precision Agriculture '13*; Stafford, J.V., Ed.; Wageningen Academic Publishers: Wageningen, The Netherlands, 2013; pp. 705–711.

[46] Karpina, M.; Jarzabek-Rychard, M.; Tymków, P.; Borkowski, A. "Uav-Based Automatic Tree Growth Measurement for Biomass Estimation". *ISPRS-Int. Arch. Photogramm. Remote Sens. Spat. Inf. Sci.* **2016**, *XLI-B8*, 685–688.

[47] Kattenborn, T.; Sperlich, M.; Bataua, K.; Koch, B. "Automatic Single Tree Detection in Plantations using UAV-based Photogrammetric Point clouds". *ISPRS-Int. Arch. Photogramm. Remote Sens. Spat. Inf. Sci.* **2014**, *XL-3*, 139–144.

[48] Kljun, N.; Calanca, P.; Rotach, M.W.; Schmid, H.P. "A simple two-dimensional parameterisation for Flux Footprint Prediction (FFP)". *Geosci. Model Dev.* **2015**, *8*, 3695–3713.

[49] Kochendorfer, J.; Meyers, T.P.; Frank, J.; Massman, W.J.; Heuer, M.W. "How Well Can We Measure the Vertical Wind Speed? Implications for Fluxes of Energy and Mass". *Bound.-Layer Meteorol.* **2012**, *145*, 383–398.

[50] Kumar, L.; Schmidt, K.; Dury, S.; Skidmore, A. "Imaging Spectrometry and Vegetation Science". In *Imaging Spectrometry: Basic Principles and Prospective Applications*; Meer, F.D.v.d., Jong, S.M.D., Eds.; Springer: Dordrecht, The Netherlands, 2001; pp. 111–155.

[51] Küng, O.; Strecha, C.; Beyeler, A.; Zufferey, J.C.; Floreano, D.; Fua, P.; Gervaix, F. "The accuracy of automatic photogrammetric techniques on ultra-light UAV imagery". *Int. Arch. Photogramm. Remote Sens. Spat. Inf. Sci.-ISPRS Arch.* **2011**, *38*, 125–130.

[52] Kustas, W.P.; Alfieri, J.G.; Nieto, H.; Wilson, T.G.; Gao, F.; Anderson, M.C. "Utility of the two-source energy balance (TSEB) model in vine and interrow flux partitioning over the growing season". *Irrig. Sci.* **2019**, *37*, 375–388.

[53] Kustas, W.P.; Anderson, M.C.; Alfieri, J.G.; Knipper, K.; Torres-Rua, A.; Parry, C.K.; Nieto, H.; Agam, N.; White, A.; Gao, F.; et al. "The Grape Remote Sensing

Atmospheric Profile and Evapotranspiration Experiment (GRAPEX)". *Bull. Amer. Meteorol. Soc.* **2018**, *99*, 1791–1812.

[54] Kustas, W.P.; Norman, J.M. "A two-source approach for estimating turbulent fluxes using multiple angle thermal infrared observations". *Water Resour. Res.* **1997**, *33*, 1495–1508.

[55] Kustas, W.P.; Norman, J.M. "Evaluation of soil and vegetation heat flux predictions using a simple two-source model with radiometric temperatures for partial canopy cover".*Agric. For. Meteorol.* **1999**, *94*, 13–29.

[56] `https://www.labsphere.com`

[57] Li, M.F.; Tang, X.P.; Wu, W.; Liu, H.B. "General models for estimating daily global solar radiation for different solar radiation zones in mainland China". *Energy Convers. Manag.* **2013**, *70*, 139–148.

[58] Liu, H.; Peters, G.; Foken, T. "New equations for sonic temperature variance And buoyancy heat flux with an omnidirectional sonic anemometer".*Bound.-Layer Meteorol.* **2001**, *100*, 459–468.

[59] Martínez-Carricondo, P.; Agüera-Vega, F.; Carvajal-Ramírez, F.; Mesas-Carrascosa, F.J.; García-Ferrer, A.; Pérez-Porras, F.J. "Assessment of UAV-photogrammetric mapping accuracy based on variation of ground control points". *Int. J. Appl. Earth Obs. Geoinf.* **2018**, *72*, 1–10.

[60] Massman, W. "A simple method for estimating frequency response corrections for eddy covariance systems". *Agric. For. Meteorol.* **2000**, *104*, 185–198.

[61] Matese, A.; Gennaro, S.F.D.; Berton, A. "Assessment of a canopy height model (CHM) in a vineyard using UAV-based multispectral imaging". *Int. J. Remote Sens.* **2017**, *38*, 2150–2160.

[62] Mathews, A.J.; Jensen, J.L.R. "Visualizing and Quantifying Vineyard Canopy LAI Using an Unmanned Aerial Vehicle (UAV) Collected High Density Structure from Motion Point Cloud". *Remote Sens.* **2013**, *5*, 2164–2183.

[63] Mesas-Carrascosa, F.J.; Notario García, M.D.; Meroño de Larriva, J.E.; García-Ferrer, A. "An Analysis of the Influence of Flight Parameters in the Generation of Unmanned Aerial Vehicle (UAV) Orthomosaicks to Survey Archaeological Areas". *Sensors* **2016**, *16*, 1838.

[64] Miura, T.; Huete, A. "Performance of three reflectance calibration methods for airborne hyperspectral spectrometer data". *Sensors* **2009**, *9*, 794–813.

[65] Neale, C.M.; Crowther, B.G. "An airborne multispectral video/radiometer remote sensing system: Development and calibration".*Remote Sens. Environ.* **1994**, *49*, 187–194.

[66] Nieto, H.; Kustas, W.P.; Alfieri, J.G.; Gao, F.; Hipps, L.E.; Los, S.; Prueger, J.H.; McKee, L.G.; Anderson, M.C. "Impact of different within-canopy wind attenuation formulations on modelling sensible heat flux using TSEB". *Irrig. Sci.* **2019**, *37*, 315–331.

[67] Nieto, H.; Kustas, W.P.; Torres-Rúa, A.; Alfieri, J.G.; Gao, F.; Anderson, M.C.; White, W.A.; Song, L.; Alsina, M.d.M.; Prueger, J.H.; et al. "Evaluation of TSEB turbulent fluxes using different methods for the retrieval of soil and canopy component temperatures from UAV thermal and multispectral imagery". *Irrig. Sci.* **2019**, *37*, 389–406.

[68] Norman, J.; Kustas, W.; Humes, K. "Source approach for estimating soil and vegetation energy fluxes in observations of directional radiometric surface temperature". *Agric. For. Meteorol.* **1995**, *77*, 263–293.

[69] Oke, T. *Boundary Layer Climates*, 2nd ed.; Cambridge University Press: Cambridge, UK, 1987.

[70] Panagiotidis, D.; Abdollahnejad, A.; Surový, P.; Chiteculo, V. "Determining Tree Height and Crown Diameter from High-resolution UAV Imagery". *Int. J. Remote Sens.* **2017**, *38*, 2392–2410.

[71] Rasmussen, J.; Nielsen, J.; Garcia-Ruiz, F.; Christensen, S.; Streibig, J.C. "Potential uses of small unmanned aircraft systems (UAS) in weed research". *Weed Res.* **2013**, *53*, 242–248.

[72] Rock, G.; Ries, J.B.; Udelhoven, T. "Sensitivity Analysis of Uav-Photogrammetry for Creating Digital Elevation Models (DEM)". *ISPRS-Int. Arch. Photogramm. Remote Sens. Spat. Inf. Sci.* **2011**, *XXXVIII-1/C22*, 69–73.

[73] Rokhmana, C.A. "The Potential of UAV-based Remote Sensing for Supporting Precision Agriculture in Indonesia". *Procedia Environ. Sci.* **2015**, *24*, 245–253.

[74] Santesteban, L.; Gennaro, S.D.; Herrero-Langreo, A.; Miranda, C.; Royo, J.; Matese, A. "High-resolution UAV-based thermal imaging to estimate the instantaneous and seasonal variability of plant water status within a vineyard". *Agric. Water Manag.* **2017**, *183*, 49–59.

[75] Schmidt, M.; Lipson, H. "Distilling free-form natural laws from experimental data". *Science* **2009**, *324*, 81–85.

[76] Schmidt, M.; Lipson, H. Eureqa (Version 0.98 beta) [Software]. 2014. Available online: `www.nutonian.com` (accessed on 15 December 2019).

[77] Schotanus, P.; Nieuwstadt, F.; De Bruin, H. "Temperature measurement with a sonic anemometer and its application to heat and moisture fluxes". *Bound.-Layer Meteorol.* **1983**, *26*, 81–93.

[78] Serrano, L.; Filella, I.; Peñuelas, J. "Remote sensing of biomass and yield of winter wheat under different nitrogen supplies". *Crop. Sci.* **2000**, *40*, 723–731.

[79] Sun, L.; Gao, F.; Anderson, M.C.; Kustas, W.P.; Alsina, M.M.; Sanchez, L.; Sams, B.; McKee, L.; Dulaney, W.; White, W.A.; et al. "Daily Mapping of 30 m LAI and

NDVI for Grape Yield Prediction in California Vineyards". *Remote Sens.* **2017**, *9*, 317.

[80] Tahar, K.N.; Ahmad, A. "An Evaluation on Fixed Wing and Multi-Rotor UAV Images Using Photogrammetric Image Processing". *Int. J. Comput. Electr. Autom. Control. Inf. Eng.* **2013**, *7*, 48–52.

[81] Tang, R.; Li, Z.L.; Jia, Y.; Li, C.; Sun, X.; Kustas, W.P.; Anderson, M.C. "An intercomparison of three remote sensing-based energy balance models using Large Aperture Scintillometer measurements over a wheat–corn production region".*Remote Sens. Environ.* **2011**, *115*, 3187–3202.

[82] Tanner, C.B.; Thurtell, G.W.T. "Anemoclinometer measurements of reynolds stress and heat transport in the atmospheric surface layer". *Dept. of Soil Science, Univ. of Wisconsin, Madison, WI, Research and Development Technical Report ECOM 66-G22-F to the US Army Electronics Command* **1969**

[83] Thiel, C.; Schmullius, C. "Comparison of UAV photograph-based and airborne lidar-based point clouds over forest from a forestry application perspective". *Int. J. Remote Sens.* **2017**, *38*, 2411–2426.

[84] Timmermans, W.J.; Kustas, W.P.; Anderson, M.C.; French, A.N. "An intercomparison of the Surface Energy Balance Algorithm for Land (SEBAL) and the Two-Source Energy Balance (TSEB) modeling schemes". *Remote Sens. Environ.* **2007**, *108*, 369–384.

[85] Torres-Rua, A. "Vicarious Calibration of sUAS Microbolometer Temperature Imagery for Estimation of Radiometric Land Surface Temperature". *Sensors* **2017**, *17*, 1499.

[86] Twine, T.; Kustas, W.; Norman, J.; Cook, D.; Houser, P.; Meyers, T.; Prueger, J.; Starks, P.; Wesely, M. "Correcting eddy-covariance flux underestimates over a grassland". *Agric. For. Meteorol.* **2000**, *103*, 279–300.

[87] Vanegas, F.; Bratanov, D.; Powell, K.; Weiss, J.; Gonzalez, F. "A Novel Methodology for Improving Plant Pest Surveillance in Vineyards and Crops Using UAV-Based Hyperspectral and Spatial Data". *Sensors* **2018**, *18*, 260.

[88] Verhoeven, G. "Taking computer vision aloft—Archaeological three-dimensional reconstructions from aerial photographs with photoscan". *Archaeol. Prospect.* **2011**, *18*, 67–73.

[89] Villagarcía, L.; Were, A.; Domingo, F.; García, M.; Alados-Arboledas, L. "Estimation of soil boundary-layer resistance in sparse semiarid stands for evapotranspiration modelling". *J. Hydrol.* **2007**, *342*, 173–183.

[90] Yilmaz, V.; Konakoglu, B.; Serifoglu, C.; Gungor, O.; Gökalp, E. "Image classification-based ground filtering of point clouds extracted from UAV-based aerial photos". *Geocarto Int.* **2018**, *33*, 310–320.

[91] `https://github.com/Mahyarona/VSSIXA`

[92] Webb, E.K.; Pearman, G.I.; Leuning, R. "Correction of flux measurements for density effects due to heat and water vapour transfer". *Q. J. R. Meteorol. Soc.* **1980**, *106*, 85–100.

[93] Weiss, M.; Baret, F. "Using 3D Point Clouds Derived from UAV RGB Imagery to Describe Vineyard 3D Macro-Structure". *Remote Sens.* **2017**, *9*, 111.

[94] White, W.A.; Alsina, M.M.; Nieto, H.; McKee, L.G.; Gao, F.; Kustas, W.P. "Determining a robust indirect measurement of leaf area index in California vineyards for validating remote sensing-based retrievals". *Irrig. Sci.* **2018**, *37*, 269–280.

[95] Willmott, C.J.; Matsuura, K. "Advantages of the mean absolute error (MAE) over the root mean square error (RMSE) in assessing average model performance". *Clim. Res.* **2005**, *30*, 79–82.

[96] Wilson, K.; Goldstein, A.; Falge, E.; Aubinet, M.; Baldocchi, D.; Berbigier, P.; Bernhofer, C.; Ceulemans, R.; Dolman, H.; Field, C.; et al. "Energy balance closure at FLUXNET sites". *Agric. For. Meteorol.* **2002**, *113*, 223–243.

[97] Xue, J.; Su, B. "Significant Remote Sensing Vegetation Indices: A Review of Developments and Applications". *J. Sensors* **2017**, *2017*.

[98] Zarco-Tejada, P.; Diaz-Varela, R.; Angileri, V.; Loudjani, P. "Tree height quantification using very high resolution imagery acquired from an unmanned aerial vehicle (UAV) and automatic 3D photo-reconstruction methods". *Eur. J. Agron.* **2014**, *55*, 89–99.

[99] Zermas, D.; Teng, D.; Stanitsas, P.; Bazakos, M.; Kaiser, D.; Morellas, V.; Mulla, D.; Papanikolopoulos, N. "Automation solutions for the evaluation of plan health in corn fields". In Proceedings of the 2015 IEEE/RSJ International Conference on Intelligent Robots and Systems (IROS), Hamburg, Germany, 28 September–2 October 2015; pp. 6521–6527.

CHAPTER 4

Downscaling UAV Land Surface Temperature using a Coupled Wavelet-Machine Learning-Optimization Algorithm and Its Impact on Evapotranspiration and Energy Balance Components Estimated by the TSEB Model

4.1 Abstract

Monitoring evapotranspiration (ET) is possible through land surface temperature (LST) measured by satellites and unmanned aerial vehicles (UAVs). The assumption that the higher resolution of LST may improve the performance of remote sensing ET models was verified in a recently published article showing that higher resolution LST led to increased performance of the Two-source Energy Balance Model (TSEB)—one of the well-known ET models. However, because of technology limitations, the spatial resolutions of satellites and UAVs in thermal wavelengths are coarser than those in optical and near-infrared (NIR) bands. Therefore, developing thermal sharpening techniques and assessing their impacts on ET models performance are imperative. Although previous studies have developed and evaluated downscaling LST methods for satellite imagery, implementation of those methods on UAV imagery is limited. In this study, a coupled wavelet, machine learning, and optimization algorithm was implemented for downscaling UAV thermal imagery from 60 cm to UAV optical imagery (15 cm) because 60 cm pixel resolution can still incorporate mixed temperatures from the soil, vine canopy, active cover crop and shaded regions. A 2D discrete wavelet transform (2-D DWT) was employed for the decomposition of inputs to 60 cm and inverse transformation of low thermal resolution to higher resolution. Four machine-learning-based algorithms (Decision Tree Regression (DTR), Ensemble Decision Tree (DTER), Support Vector Machine (SVM), and Gaussian process regression (GPR)) along with four linear regression-based models (linear, interactions linear, robust linear and stepwise linear) are used as the potential fitting models, and a grid search algorithm

is used for auto-tuning parameters of the machine learning algorithms. Additionally, a novel sampling technique was designed to provide more representative samples for training steps in the regressing models. Four sets of high-resolution images were provided by the Utah State University AggieAir sUAS Program as part of the ARS-USDA GRAPEX Project collected since 2014 over multiple vineyards located in California. After applying the proposed downscaling algorithm, a separation method was used for estimation of canopy and soil temperatures from the original and sharpened thermal imagery. Ultimately, the TSEB model was executed for these pairs of temperature components, and its performance compared to eddy covariance measurements. Results demonstrated that the proposed sampling algorithm can significantly accelerate the computation time for the UAV temperature sharpening efforts. Among all the fitting models, GPR, SVM and DTER were the most accurate in terms of R-square. The correlation between NDVI and radiometric temperature (Tr) was significantly improved when the downscaled Tr (DTr) was used in the NDVI-Tr domain for the separation procedure. Compared to additional IRT sensors temperatures, Tc and particularly Ts derived from the DTr were closer to the observed measurements. After feeding the TSEB model with DTr products, results demonstrated that estimations of soil heat flux (G) were significantly improved, while large LE differences were reduced.

4.2 Introduction

Land surface temperature (LST) is required for various applications such as wildfire ([18]), urban heat island ([48], [53]), land cover types ([55]), and retrieving surface soil moisture ([41]). Compared to vegetation parameters and the surface albedo, LST is more responsive to surface energy fluxes ([10]) and is a key input for remote sensing evapotranspiration (ET) models to modulate energy fluxes over extensive areas (Zhan et al. 2013 [54]). Nowadays, estimation of Evapotranspiration (ET) at farm and plant scale is possible using high-resolution (i.e., 10^1–10^2 m) and super-high-resolution (i.e., less than 1 m) land surface temperature (LST) from satellites and unmanned aerial vehicles (UAVs), respectively. However, the trade-off between temporal and spatial resolution leads to a platform with either high-spatial/low-temporal resolution or low-spatial/high-temporal resolution (Agam et al.

2007 [6], Essa et al. 2013 [22]). In addition to this trade-off, even within the same platform, the spatial resolution of thermal infrared sensors is coarser than that of shortwave spectral band imagery (Gao et al. (2012) [23]). For example, the ratio of the spatial resolution of Landsat TM sensor in the thermal band (120 m) to the shortwave band (30 m) is 4. In the AggieAir UAV platform (`https://aggieair.usu.edu`) at 450m agl, the typical resolution of visible and NIR bands is mostly about 10 cm, while thermal band resolution is 60 cm. Thus, this ratio increases to 6. Although the spatial resolution of the thermal band provided by high-resolution satellites such as Landsat 8 is enough for monitoring crop conditions at the farm level, the long repeat cycle of satellite data is not suitable for routine ET estimation (Gao et al. (2012) [23], Kustas et al. 2003 [30]). This deficiency has been addressed by development of several downscaling and desegregation methods applied on higher temporal frequency – coarser resolution thermal-infrared data from the Moderate Resolution Imaging Spectroradiometer (MODIS), Geostationary Orbiting Environmental Satellite (GOES) ([25], [24]), and the Advanced Very High Resolution Radiometer (AVHRR) ([52]).

Nonetheless, the higher-resolution thermal imagery provided by UAVs is still more desirable due to the thermal mixture effect (TME), defined as a blending of thermal information in a large thermal pixel where the resolution is coarser than the thermal elements (Zhan et al. 2013 [54], Strahler et al., 1986 [42]). For example, the highest resolution of AggieAir UAV thermal imagery at 450 m agl (above ground level) is 60 cm, which is a mixture of the soil, vegetation, and shaded and sunlit regions. This mixture of information has an effect on ET models working with high-resolution imagery such as the two-source energy balance (TSEB) model. For instance, partitioning radiometric surface temperature (T_r) to the canopy and soil temperature (T_C and T_S) using TSEB-2T requires the T_r and normalized difference vegetation index (NDVI) at the same scale (Nieto et al. (2019) [37]). Since NDVI is available at a higher resolution compared to Tr, one way to use this approach is up-scaling NDVI to the T_r resolution (10 cm to 60 cm), fitting a linear regression model on the NDVI-Tr domain, and estimating T_S and T_C by substituting NDVI soil and canopy thresholds ($NDVI_S$ and $NDVI_C$) in the fitted model. In this approach, a strong

linear correlation is assumed between Tr and NDVI if both are available at high resolution. However, upscaling NDVI to Tr resolution (10 cm to 60 cm) lead to an NDVI with the mixed effect of different elements (e.g., soil and vegetation). Although one recent publication demonstrated that the sharpened temperature would allow a better discrimination between Tc and Ts [37], comprehensive changes in NDVI-Tr correlation at different scales (10 cm, 30 cm, 60 cm) have not yet been examined. One of the specific applications of higher resolution Tr is related to extraction of only vine canopy temperature when an active cover crop is also present in vineyards (in the early growing season). Due to active interrow cover crops and vines having the same spectral responses in the R, G, B and NIR wavelengths, separation of pure vine pixels from active cover crop using popular VIs such as NDVI is not possible. However, histogram analysis of temperature can be an alternative if the temperature is available at VNIR pixel resolution. The consequences of the TME in different applications result in increasing demand for disaggregation, downscaling, or sharpening techniques, although few studies are focusing on sharpening techniques for UAV thermal imagery.

During the last twenty years, two types of thermal sharpening techniques have been developed: physical downscaling methods (PDMs) and statistical downscaling methods (SDMs) ([22]). These are the most common approaches for LST downscaling ([9]), and they are based on the assumption that, if a unique and strong relationships between T_r and aggregated predictors (e.g., VIs) exists, it can be valid across multiple resolutions (Agam et al. 2007, [6]). However, the PDMs are based on establishing a physically functional relationship between LST and aggregated predictors, such as the disTrad method developed by Kustas et al. 2003 ([30]) and employed by Anderson et al. 2004 ([8]). Whereas the SDMs mostly rely on exploring a strong linear or non-linear relationship between LST and upscaled predictors without referring to physical meaning. ([22]). One of the popular approaches to statistically downscale LST is to explore the relationship between the aggregated NDVI and LST to be applied to the original resolution of NDVI (higher spatial resolution). However, NDVI cannot explain all variations in LST in heterogeneous land covers ([11]). Nemani et

al. 1993 ([36]) showed that the slope of LST-NDVI could be controlled by a wide range of factors such as fractional vegetation cover, crop type, and surface moisture availability.

2D-wavelet is a mathematical algorithm that decomposes an image into different frequency components. Many studies investigated the application of 2D-wavelet transform algorithm in scaling problems to determine the surface heterogeneity and appropriate scale for different physical processes. For instance, Pelgrum et al. ([38]) employed wavelet variance with auto-correlation analysis to infer length scales of land surface characteristic using remote sensing data. Brunsell and Gillies ([13]) used wavelet analysis to determine the scaling characteristics of AVHRR radiometric temperature images in a homogeneous area. They found that both NDVI and radiometric temperature show similar scaling behaviors. However, scaling problems become more complicated when degree of spatial heterogeneity and model non-linearity increase. Although wavelet transform algorithms are popular methods to describe the spatial surface heterogeneity, machine learning algorithms have been used extensively to model systems with nonlinear behavior.

With the advent of machine learning algorithms and advanced versions such as Deep Learning, various types of these algorithms have been employed to consider non-linear relationships between aggregated high-resolution variables such as vegetation indices (VIs) at courser resolution and LST ([51], [52]). Although machine learning methods have been reported to be satisfactory in downscaling temperature, they are site- and time-specific and require re-calibration for different datasets as they are trained for a specific set of input variables. In addition, current downscaling versions are mostly developed for satellite pixel resolutions ($<10^2$ m).

To the best of the authors' knowledge, the performance of downscaling methods has not been evaluated for UAV super-high-resolution imagery (less than 1 m), whereas topographical information such as the digital surface model and slopes derived from UAV point cloud data also can be possible predictors in downscaling techniques. To bridge this gap, a coupled wavelet-machine learning-optimization algorithm is proposed to explore non-linear relationships between possible predictors and LST over a heterogeneous area. The first ver-

sion of this model is presented by Kaheil et al. (2008 [26]) to downscale ET from NOAA LST with 960-m resolution to 15 m. In that model, (1) finer resolution inputs are decomposed to approximation and detail coefficients at coarser resolution using a wavelet decomposition method; (2) a support vector machine (SVM) as the machine learning tool is trained by approximation coefficients of inputs and output; (3) detail coefficients for coarse resolution output are generated by the trained SVM; and (4) output at finer resolution is generated by applying the inverse wavelet transform. Despite the statistical methods, this method explores a unique relationship between variables at the decomposition level (different pixel resolutions).

In this study, we hypothesized that downscaled LST can improve the accuracy of LST separation between Ts and Tc and consequently can result in a better estimation of energy fluxes by the TSEB model. This is due to the fact that the TSEB model is highly sensitive to Ts and Tc estimates. To test this hypothesis, a 2-D DWT is used to decompose high-resolution imagery to LST resolution and to inverse transform LST to higher LST resolution. A new sampling training method has been designed to select more representative records for fitting regression models in each decomposition level. Instead of SVM, four different machine learning algorithms, along with four linear-based models, are considered to find the relationship between possible predictors and LST. The parameters of machine learning methods are tuned with a grid search method. The proposed method is employed to sharpen UAV thermal imagery captured over a commercial vineyard located in California as a part of the GRAPEX project ([28]) from 60 cm to 15 cm . To take advantage of 3D UAV point cloud information, in addition to multi-spectral information and VIs, DSM and slope derived from the UAV point cloud data are considered in the set of possible predictors. Ultimately, The impact of downscaled LST (DTr) on Ts and Tc derivation from the NDVI-Tr domain and consequently on energy fluxes estimated by the TSEB model are presented. TSEB is executed with Ts-Tc pairs before and after applying the downscaling algorithm, and TSEB outputs are compared with eddy covariance measurements.

4.3 Study of Area

This study was conducted over a commercial vineyard located near the town of Galt in California's Central Valley as a part of the GRAPEX project ([28]); hereafter it is referred to the Lodi site. This site consisted of two blocks: the northern block (Block 1) and the southern block (Block 2). Block 1 was planted with the Pinot Noir variety in 2009 and Block 2 was planted with the same variety in 2011. The age differences resulted in older, taller, more mature grapevines along with higher biomass and leaf area at Block 1 compared to Block 2. In each block, an eddy covariance tower is installed half-way North–South along the Eastern edge because the dominant wind direction is mostly from west to east during daylight hours from March to October (Fig 4.1).

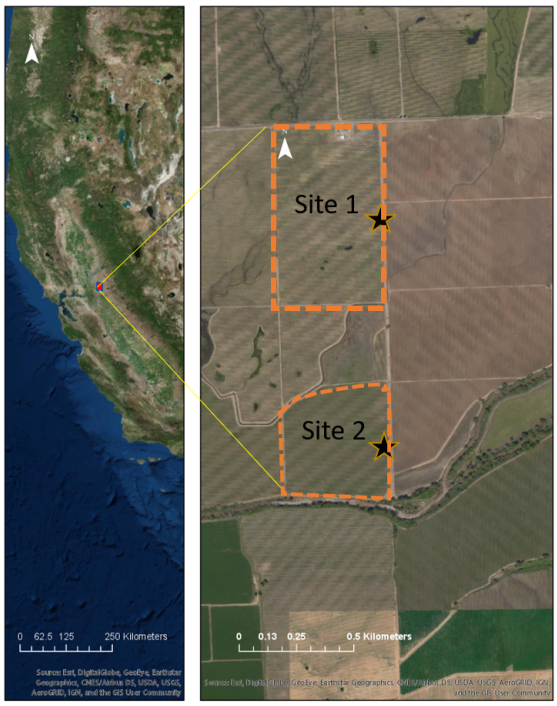

Fig. 4.1: The study area boundaries along with the locations of the eddy covariance towers installed in the area of study

In both blocks, a "U" shaped trellises is employed for the training system in which canes are trained upwards, and the height to first and second cordons is about 1.30 m (4' 4", Fig 4.2c) and 1.9 m, respectively. Canopy vine heights ranged from 2 to 2.5 m, and

in-row vine spacing was about 1.5 m (4’ 8”) (Fig 4.2b) and an East–West row orientation. A drip irrigation system is installed at 35 cm (14”) agl (Fig 4.2a).

Inter-row cover crops can be used to manage vineyard growth and increase yields. Particularly in winter, cover crops like peas and clover can significantly increase nitrogen content in the soil. In order to control water content in soil surface layer and regulate vine vigor early in the growing season, inter-row grass cover crops are planted in both blocks (Block 1 and Block 2) and is mowed in either late April or early May.

(a) (b) (c)

Fig. 4.2: (a) A drip irrigation system, (b) space between vines, (c) height to first and second cordons measured by the “Measure app” using Apple’s ARKit 2

4.3.1 AggieAir Remote Sensing Platform

AggieAir UAVs operated by the AggieAir UAV Research Group at the Utah Water Research Laboratory at USU (`https://aggieair.usu.edu`) are designed to acquire high-resolution imagery (less than 20 cm at 1000 m agl) using multi-spectral and thermal cameras. In this study, A fixed-wing small AggieAir UAV called Minion was used to capture high-resolution multi-spectral and thermal imagery over the Lodi site from 2014 to 2016. The battery capacity of this platform provides sufficient power for an hour at a speed of 48 Km

per hour. Minion consists of two cameras (one for multi-spectral imagery and the other one for thermal), a computer, a GPS module, an IMU, a radio controller, and flight control. This platform has the capability to store the coordinates and sensor view of aircraft for each image ([21]).

Fig. 4.3: AggieAir UAV capturing high-resolution imagery over the vineyard

4.3.2 AggieAir UAV High-resolution Imagery

In this study, four sets of high-resolution images (15 cm or finer in the multi spectral-bands and 60 cm in the thermal spectrum) collected by the Minion UAV over the GRAPEX Pinot Noir vineyard in 2014, 2015, and 2016 are used to assess the proposed downscaling method and the TSEB model. An example of the high-resolution imagery recorded by Minion over the commercial vineyard is shown in Figure 4.4, and the properties of the UAV images and products are summarized in Table 4.1.

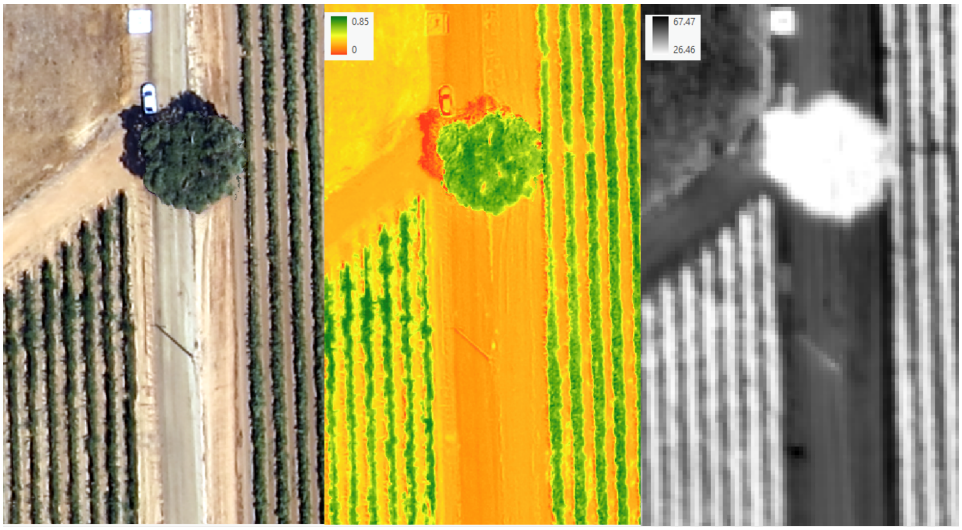

RGB at 15 cm resolution NDVI at 15 cm resolution Tr at 60 cm resolution

Fig. 4.4: A subset of imagery captured by AggieAir in August 2014

Flight dates, configurations of cameras and sensors, growth stages, and pixel resolution are summarized in Tables 4.1 and 4.2.

Table 4.1: Flight time, sensors and filters used in Minion to capture images

Date	UAV Flight Time (PDT)		UAV elevation	Bands		Cameras and Optical Filters		Spectral Response
	Launch Time	Landing Time	(agl) meters	RGB	NIR	Radiometric Response	MegaPixels	
August 9, 2014	11:30 AM	11:50 AM	450	Cannon S95	Cannon S95 modified (Manufacturer NIR block filter removed)	8-bit	10	RGB: typical CMOS NIR: extended CMOS NIR Kodak Wratten 750 nm LongPass filter
June 2, 2015	11:21 AM	12:06 PM	450	Lumenera Lt65R Color	Lumenera Lt65R Monochrome	14-bit	9	RGB: typical CMOS NIR: Schneider 820 nm LongPass filter
July 11, 2015	11:26 AM	12:00 PM	450	Lumenera Lt65R Color	Lumenera Lt65R Monochrome	14-bit	12	RGB: typical CMOS NIR: Schneider 820 nm LongPass filter
May 2, 2016	12:53 PM	1:17 PM	450	Lumenera Lt65R Mono	Lumenera Lt65R Mono	14-bit	12	RED: Landsat 8 Red Filter equivalent NIR: Landsat 8 NIR Filter equivalent

Table 4.2: Flight dates, spatial resolution, point cloud, and phenological stages when the images were captured by Minion

Date	Optical resolution	Thermal resolution	Point Cloud density (point/m^2)	Vine Phenological Stage	Phenological Stage of Cover Crop
August 9, 2014	15 cm	60 cm	37	Veraison towards harvest	Mowed stubble
June 2, 2015	10 cm	60 cm	118	Near veraison	Senescent
July 11, 2015	10 cm	60 cm	108	Veraison	Mowed stubble
May 2, 2016	10 cm	60 cm	120	Bloom to fruit set	Active/green

As described in Tables 4.1 and 4.2, all the main growth stages (Bloom to fruit set, near veraison, veraison and veraison towards harvest) are covered by the imagery captured from May to August. Except for 2014 that a consumer-grade camera (Canon S95) is used to capture imagery, the industrial type of Lumenera monochrome cameras with narrowband filters in red and near-infrared bands (equivalent to Landsat 8 sensor specifications) are used in 2015 and 2016. The resolution of VNIR images was 10 cm, except for the August flight while the resolution of thermal images was 60 cm for all the flight.

4.3.3 AggieAir Image Processing

After imagery acquisition, image processing steps are required to prepare the imagery for further analysis: (1) radiometric calibration, (2) image mosaicking and orthorectification, and (3) satellite (Landsat-8) harmonization. In the radiometric calibration, which was based on the method developed by Neale and Crowther, 1994 [35]; Miura and Huete, 2009 [34]; and Crowther, 1992 [17]), the digital numbers of images were calibrated to reflectance using pre- and post-flight Labsphere (`https://www.labsphere.com`) Lambertian panel readings. The effect of vignetting is additionally corrected in the radiometric calibration step. In the image mosaicking and orthorectification step, UAV images were merged into a single scene and linked into the WGS84 UTM 10N coordinate system using Agisoft Photoscan software [7] and GPS control points. Since various types of multi-spectral sensors were used between 2014 and 2016, a harmonization technique was employed to reduce the bias of remotely sensed information captured at different pixel resolutions and by different sensors ([5]). In the harmonization technique, the UAV multi-spectral imagery is aggregated to the Landsat-

8 scale using a point spread function (PSF); its bias is corrected with a linear transformation ([5]). For UAV thermal imagery, after the image mosaicking and orthorectification steps, a vicarious calibration was applied. More information on the vicarious calibration can be found in Torres 2017 [44].

4.3.4 Field Measurements, Point cloud and DTM

For each flight, ∼80 LAI records were acquired using the LAI-2200c sensor, and those measurements were corrected with direct LAI measurements ([49]). Aboutalebi et al. 2020 ([4]) evaluated vegetation spectral and structural information derived from point cloud information versus these in-situ LAIs and proposed three LAI models. The LAI maps for each flight, estimated from that study based on the Vegetation Spectral-Structural Information eXtraction Algorithm (VSSIXA), are inputs to the TSEB model. In addition to the LAI map, a DSM was generated using point clouds that were produced from the multispectral images. The DSM's spatial resolution was the same as the multispectral imagery. The slope and aspect from DSM raster files were generated using the Aspect-Slope function from the ArcGIS Pro toolbox.

Eddy covariance and micrometeorological data were collected for each of the vineyard blocks (Block 1 and Block 2) in 2013. The data were quality controlled and were stored as hourly block-averaged data. More information about the measured parameters, quality procedure, and post-processing of the turbulent fluxes are addressed in Aboutalebi et al. 2020 [4]. In addition to quality control of eddy covariance measurements, the concept of energy balance closure is used to correct any imbalance between available energy (Rn-G) and H + LE by assuming that the Bowen ratio (BR) H/LE is correct. In this method, the adjusted H and LE (H_{BR} and LE_{BR}) are calculated by Eqs (4.1–4.2) ([45]). .

$$H_{BR} = \frac{H}{H + LE} \times (Rn - G - H - LE) + H \tag{4.1}$$

$$LE_{BR} = \frac{LE}{H + LE} \times (Rn - G - H - LE) + LE \tag{4.2}$$

4.4 Methods

The proposed downscaling method is a combination of four sub-modules; (1) the wavelet module for the decomposition of high-resolution imagery inputs to LST resolution and reconstruction of LST approximation and detail coefficients to high-resolution imagery; (2) the regression module for generation of LST detail coefficients; (3) the sampling module for training the regression module with more representative grids; and (4) the optimization modules for auto-tuning the regression module's parameters. In the following section, the framework of the proposed downscaling method, along with a short description of each of these sub-modules, is presented. In the end, a brief description of the TSEB model and temperature component estimation and the effect of the downscaling method on the performance of the TSEB model are presented.

4.4.1 The Proposed Downscaling Algorithm

The principle of this proposed algorithm is based on the fact that a higher resolution of every image can be reconstructed using an inverse wavelet transform if the approximation image and detail coefficients of a decomposed image are available. Therefore, the main goal in each level is to estimate the detail coefficients for the coarser image (i.e., the thermal imagery) and then apply inverse wavelet transform to produce higher resolution imagery. The first idea of this algorithm is presented by Kaheil et al. 2008 [26] for downscaling and forecasting of evapotranspiration using a synthetic model of wavelets and SVM. That model is enhanced in this investigation, and the workflow of the proposed downscaling algorithm is illustrated in Fig 4.5.

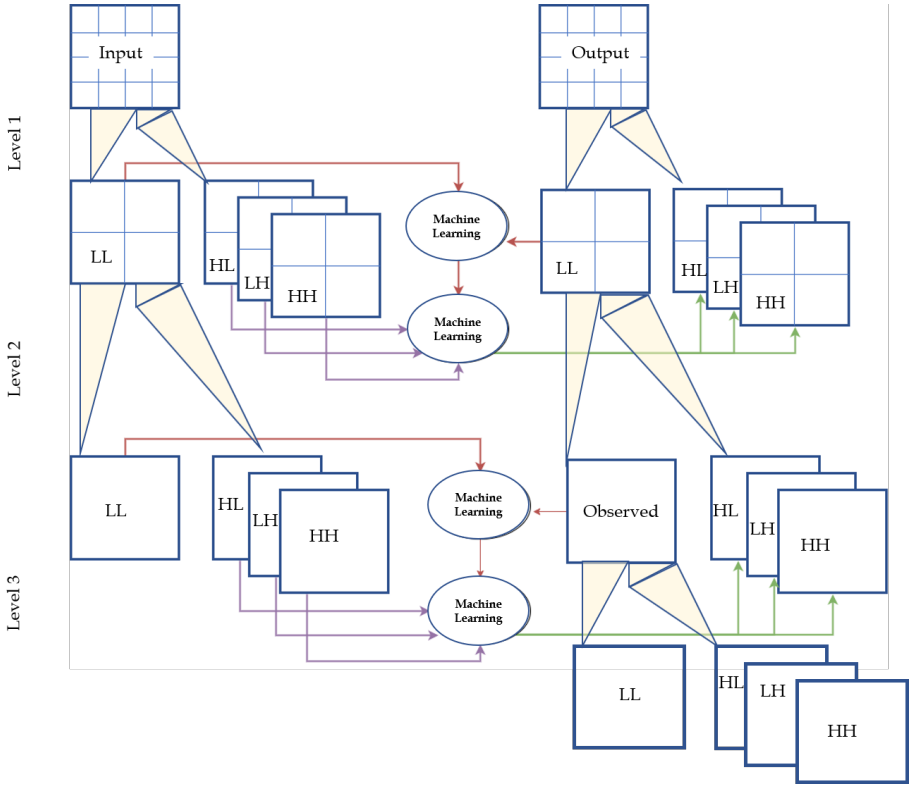

Fig. 4.5: Flowchart of the proposed downscaling algorithm (Level 1: the 1st decomposition level, Level 2: the 2nd decomposition level, Level 3: the 3rd decomposition level).

As shown in Fig 4.5, the higher resolution images (i.e. VNIR bands imagery and DTM) are first decomposed using a wavelet transform and a wavelet basis function (a two-coefficient Haar function, which resembles a step function) to approximation [low-low (LL)] and detail coefficients [high-low (HL), low-high (LH), and high-high (HH)] until the size of approximation and detail coefficients is equal to the observed image (i.e., LST). Next, the regression module will be trained with the approximation coefficients (i.e. approximation coefficients of VNIR versus LST). In this study, four types of machine learning algorithms and four types of the linear regression model are used to train LL-observed pairs (approximation coefficients) and then applied on HL, LH, and HH matrices of inputs to generate detail coefficients for the output (e.g., LST). To maximize the performance of the machine learning algorithms, their parameters are tuned with a grid search algorithm. Due to the very high number of pixels in each training level (in this study, 457x157 pixels in level 2 and

914 x 314 in level 1), an efficient sampling algorithm is needed to accelerate the training procedure speed; therefore, a new sampling technique was designed to select more representative pixels for each training step. Due to convolution processes performed at the training step, the estimated detail coefficients (HL, LH and HH of the testing step) have an inherent linear bias ([26]). The linear bias corrector can be found by fitting a linear regression model between the detail coefficients of the observed image and its detail coefficients at the next level (Level 3 in Fig 4.5). By applying an inverse wavelet transform, a higher resolution of the observed image will be achieved. This process must continue until the size of the new target matrix is equal to the size of the input matrices. In this method, the number of wavelet levels depends on the resolution of the inputs and the target imagery. For example, if the input imagery is captured at 15 cm and the target imagery resolution is 60 cm, only two levels of decomposition are enough to reach the target resolution and vice versa ($\frac{60}{15} = 4 = 2^2$).

4.4.2 Wavelet Decomposition and Reconstruction

Wavelet transformation is a powerful tool for the decomposition of a signal into a different frequency scale. Among various applications, it is an effective tool in remote sensing to analyze the variability of the geophysically distributed variables across different resolutions ([27]), edge detection ([43], [33]), dimensionality reduction ([12], [31]), image fusion ([56], [15]) and downscaling ([26]). In the wavelet decomposition technique, a signal is separated into multi-resolution components in which the high-resolution and low-resolution components represent the fine and coarse scale features, respectively ([16]). The properties of wavelets are valid for both 1-D signal and 2-D datasets such as images and matrices. In the 2-D discrete wavelet transform (2-D DWT) used in this investigation, low- and high-pass filters are recursively applied on the finest scale for capturing the variability information ([26]). 2-D DWT is an expanded version of the Mallat's forward pyramid algorithm, where 1-D low and high-pass filters are passed through the rows and columns, respectively, generating two sets of wavelet coefficients of the original image: approximation [low-low (LL)] and detail [high-low(HL), low-high (LH), and high-high (HH)]. Moreover,

these approximation and detail coefficients can be used for reverse 2-D DWT (inverse wavelet transform) to reconstruct and obtain the higher-resolution on each scale. Fig 4.6 shows one level decomposition and reconstruction of sub-imagery captured by Minion over the study area.

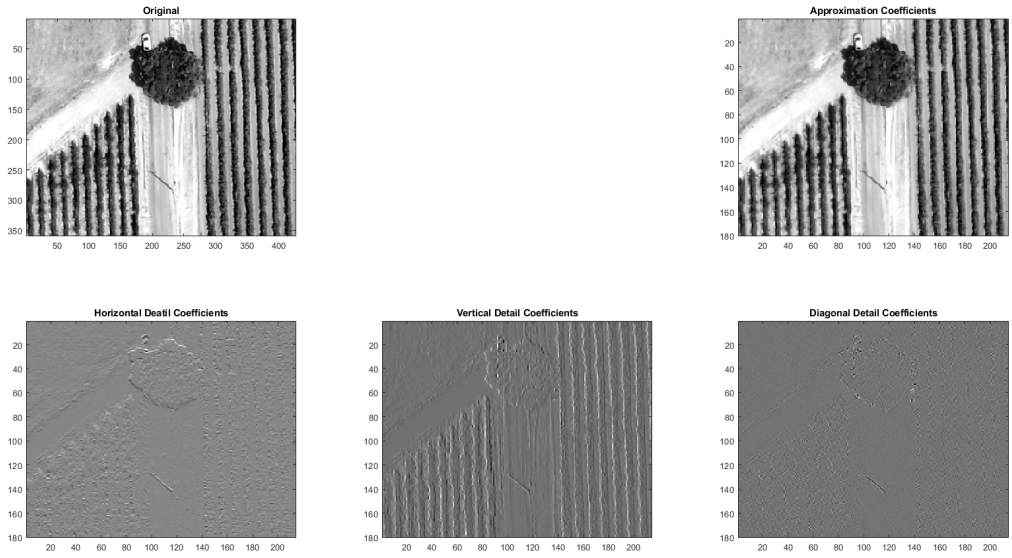

Fig. 4.6: Example of wavelet output coefficients for a single-level discrete 2-D wavelet transform applied on sub-UAV imagery captured in the red band

As shown in Fig 4.6, the approximation coefficients show the smooth version of the original image (without noise), whereas detail horizontal, vertical, and diagonal coefficients captured horizontal, vertical, and diagonal edges, respectively.

4.4.3 The regression module

In the proposed downscaling algorithm, the regression model contains two categories of regression models: machine learning algorithms and linear-based models. The machine learning algorithms are decision tree regression (DTR), decision tree ensemble regression (DTER), support vector machine (SVM), and Gaussian process regression (GPR) models,

and linear-based models are linear regression (LR), robust linear regression (RLR), interactions linear regression (ILR), and step-wise linear regression (SLR).

Similar to any linear-fitted problem, machine learning-based models are designed to find weights and bias values in a regression model (Eq. 4.3) by means of solving an optimization problem over training datasets while considering a specific objective function.

$$y = f(x) = w^T \times x + b\,, \tag{4.3}$$

in which, y = an output vector, $f(x)$ = a linear regression model connecting input vectors to the output vector, w = weighting vector, x = input vectors, T = the transpose sign, and b = bias. Analogous to machine learning-based models, Eq. (4.3) will be solved for w and b over training datasets (i.e., a subset of the input-output space) by minimizing an error function. The machine learning-based algorithms can be modified to be used as a non-linear fitting model by means of a non-linear kernel function ($K(x, x_i)$ in Eq. 4.4).

$$y_i = f(x_i) = w^T \times K(x, x_i) + b. \tag{4.4}$$

In general, non-linear kernel functions are developed and used when inputs are not linearly related to outputs. In other words, kernel functions evaluate the correlation between inputs and the output in a new space where inputs can be linearly related to the output. Various kernel functions for machine learning algorithms have been developed and polynomial, sigmoid, and radial basis function (RBF) are popular kernel functions among them.

DTRs are constructed by recursive partitioning. They are starting from a root node that then is split into two nodes. The root node is known as the parent, and the two nodes in the next layer are called child nodes. Each child node can be split again and generates two more nodes. In DTRs, Eq. 4.5 is solved for each node by minimizing the weighted mean squared error (WMSE in Eq. 4.3).

$$WMSE(t) = 1/N_t \sum_{i=1}^{n} (y_i - y_t)^2 \tag{4.5}$$

in which N_t is the number of training records at node t, n is the training subset at node t, and y_t is the true observed value. Ensemble DTRs combines a few DTRs to enhance the prediction accuracy compared to a single decision tree using two techniques: bagging and boosting. In the bagging approach, several subsets from the training records are randomly selected for training DTRs and the average of all the outputs from the different trees is reported, which is more robust compared to a single decision tree. In the boosting approach, consecutive trees are fitted on the training records and at the end of each tree, the error from the prior tree is analyzed.

The support vector machine (SVM) presented by Vapnik (1995 [46]) is for clustering, classification, and regression analysis. To design SVR, Vapnik (1998 [47]) presented a new error function, which is called the epsilon intensive (e-intensive) function (Eq. 4.6).

$$|\hat{y} - f(x)| = \begin{Bmatrix} 0 & if|\hat{y} - f(x))| \leq \kappa \\ |\hat{y} - f(x))| - \kappa = \xi & otherwise \end{Bmatrix}, \tag{4.6}$$

in which, $\hat{y}$ = predicted/estimated y (the SVR output), κ = maximum allowed errors threshold so that an error between zero and κ is considered as zero and an error greater than κ is actual absolute error minus maximum allowed errors threshold (ξ). Therefore, κ plays an important role in the sensitivity of the error function. κ is a parameter defined by users and makes the absolute error function insensitive when the error ($\hat{y} - f(x)$) falls within [-κ, +κ]. In addition to the e-intensive function, Vapnik (1998 [47]) added two more terms (1) a coefficient (C) to adjust the weight of the insensitive range of error and (2) a regularization term ($\frac{1}{2}||w||^2$ in Eq. 4.7) to prevent the over-fitting (Aboutalebi, 2018 [1]).

$$\begin{aligned} &Minimize\ \tfrac{1}{2}\|w\|^2 + C\sum_{i=1}^{m}(\xi_i) \\ &subject\ to\ |y_i - f(x_i))| - \kappa < \xi_i. \end{aligned} \tag{4.7}$$

$$\begin{gathered} Minimize\ \tfrac{1}{2}\left\|w\right\|^2 + C\sum_{i=1}^{m}(\xi_i) \\ subject\ to\ |y_i - \hat{y}_i)| - \kappa < \xi_i. \\ where\ \hat{y}_i = f(x_i) = w^T \times K(x, x_i) + b. \end{gathered} \tag{4.8}$$

The non-linear form of SVR (Eq. 4.8) possesses at least three user-defined parameters, including κ, C, and kernel function parameter(s). In addition, SVR does not employ the input selection feature to efficiently select the main descriptors among possible inputs, which leads to a decrease in the SVR training speed ([2], [3]).

Similar to Gaussian distribution that is specified by its mean and variance, GPR is defined by a mean function $m(x)$ indicating the mean of estimations at observation input points and a covariance function that relates one observation to another (the covariance between the target input point and other input points ($K(x, x')$)). One of the popular covariance functions ranging from 0 and σ_f^2 is the "squared exponential":

$$k(x, x') = \sigma_f^2 exp\frac{-(x - x')^2}{2l^2} \tag{4.9}$$

in which l is the length parameter governing the impact of distant observation at new x values during interpolation, and σ_f are hyperparameters defining the covariance function. To apply GPR, the covariance function is calculated for all observed points (K), between new input points and the observed points (K_*), and between new input points K_{**} [40]:

$$K = \begin{bmatrix} k\left(x_1, x_1\right) & k\left(x_1, x_2\right) & \dots & k\left(x_1, x_n\right) \\ k\left(x_2, x_1\right) & k\left(x_2, x_2\right) & \dots & k\left(x_2, x_n\right) \\ \vdots & \vdots & \ddots & \vdots \\ k\left(x_n, x_1\right) & k\left(x_n, x_2\right) & \cdots & k\left(x_n, x_n\right) \end{bmatrix} \tag{4.10}$$

$$K_* = \begin{bmatrix} k\left(x_*, x_1\right) & k\left(x_*, x_2\right) & \cdots & k\left(x_*, x_n\right) \end{bmatrix} \tag{4.11}$$

$$K_{**} = k\left(x_*, x_*\right) \tag{4.12}$$

In GPR, by definition, the joint (multivariate) normal distribution of observed output values (y) and estimated output values for new input points (y_*) is as follows:

$$\begin{bmatrix} \mathbf{y} \\ y_* \end{bmatrix} \sim \mathcal{N}\left(\mathbf{0}, \begin{bmatrix} K + \sigma_\epsilon^2 I & K_*^{\mathrm{T}} \\ K_* & K_{**} \end{bmatrix}\right) \tag{4.13}$$

in which I is an identity matrix and σ_ϵ^2 is the assumed noise level of observations. The conditional probability of Eq. 4.13 can be written as:

$$y_*|\mathbf{y} \sim \mathcal{N}\left(K_* K^{-1}\mathbf{y}, K_{**} - K_* K^{-1} K_*^{\mathrm{T}}\right) \tag{4.14}$$

in which, the first term in the distribution ($K_* K^{-1}\mathbf{y}$) is the best estimation for new input points, and the second term ($K_{**} - K_* K^{-1} K_*^{\mathrm{T}}$) is the uncertainty in the GPR estimations [20]. The performance of GPR is highly dependent on the covariance function's parameters θ (e.g. l, σ_f,σ_ϵ). A common practice to obtain reliable estimations of GPR's hyperparameters is to maximize marginal (log) likelihood ([39]) that can be implemented by means of the partial derivatives of Eq. 4.15 with respect to θ.

$$\log p(y|X, \boldsymbol{\theta}) = -\frac{1}{2} y^\top K_y^{-1}\mathbf{y} - \frac{1}{2}\log|K_y| - \frac{n}{2}\log 2\pi \tag{4.15}$$

in which $K_y = K + \sigma_\epsilon^2 I$.

4.4.4 Grid search

As discussed in the regression module section, except for the linear-based models, each of the regression methods employed in this study has its own hyperparameters, and an optimizer called "grid search" embedded in the "MATLAB regression learner" is used to tune those hyperparameters. In each iteration, the grid search algorithm starts searching and evaluating the model based on an objective function (maximizing accuracy in this case) using uniform sampling without replacement from a range of values allowed in each parameter. More information about this optimization algorithm, the optimizable hyperparameters and

the range considered for each hyperparameter is available at (`https://www.mathworks.com/help/stats/hyperparameter-optimization-in-regression-learner-app.html`)

4.4.5 Sampling technique for training the regression modules

As shown in Fig 4.5, for each level, the regression modules are trained with LL inputs and LL observed pairs. Since the size of LL matrices is quite large and may lead to an increase in the computation time of the machine learning-based regression algorithms, a sampling technique is required to extract a subset of LL pairs and accelerate the training procedure. In this study, a new sampling technique was designed wherein 20% of LL matrices are randomly selected and clustered to k groups by means of the k-means clustering algorithm. For each cluster, a simple index is calculated based on Eq. 4.16. This index considers high weights for clusters with a small number of members and low weights for clusters having more members.

$$Index_i = (1 - (Nm_i/N))^p \tag{4.16}$$

in which Nm_i is the number of members in Cluster i, N is the subset size (e.g. 20% of the LL matrix), and p is an integer parameter (larger than 1) to accentuate the importance of small size clusters and underemphasize the importance of large size clusters. After calculating this index for each cluster, training samples are randomly selected with the size of $\lceil Index_i * N \rceil$ from each cluster without replacement. In general, this sampling technique involves special records from LL pairs (e.g. extreme values) in the training sample, leading to an increment of accuracy in the machine learning-based algorithms.

4.4.6 Two-source Energy Balance (TSEB) Model

The TSEB model with Tc and Ts estimates based on contextual NDVI-Tr domain (TSEB-2T [37]) first calculates net shortwave (Sn) and longwave radiation (Ln). In the next step, soil and canopy net longwave radiation (Ln_s and Ln_c) is calculated based on Eqs. 4.17–4.18) developed by Kustas and Norman 1999 [29]. .

$$Ln_c = (1 - exp(-k_L \Omega LAI))(L_{sky} + L_s - 2L_c) \tag{4.17}$$

$$Ln_s = exp(-k_L \Omega LAI) L_{sky} + (1 - exp(-k_L \Omega LAI)) L_c - L_s \tag{4.18}$$

where L_s, L_c and L_{sky} $(W/(m^2))$ are the longwave emissions from soil, canopy, and sky, respectively; k_L is the longwave radiation extinction coefficient; and Ω is the clumping factor presented by [29].

Similar to net longwave radiation, canopy and soil net shortwave radiation (Sn_c and Sn_s) are calculated in a canopy radiative transfer model presented by Campbell and Norman (1998) [14]). Then canopy and soil net radiation (Rn_c, Rn_s) are calculated using Eqs. 4.19-4.20.

$$Rn_c = Ln_c + Sn_c = Ln_c + (1 - \tau_s)(1 - \alpha_c) S \tag{4.19}$$

$$Rn_s = Ln_s + Sn_s = Ln_s + \tau_s (1 - \alpha_s) S \tag{4.20}$$

where S $(W/(m^2))$ is the incoming shortwave radiation, τ_s is solar transmittance through the canopy, and α_s and α_c are the soil and canopy albedo, respectively.

Soil heat flux (G) is considered to be a portion of Rn_s (e.g. 20% to 30%). The model computes the sensible heat flux for the canopy and soil layers separately (H_s and H_c). It first assumes having a neutral atmospheric stability condition. Then, the sensible heat flux is corrected through an iterative method until Monin-Obukhov length changes reach a minimum. Next, canopy and soil latent heat fluxes (LE_c and LE_s) are calculated as residuals in the canopy and soil energy balance equations (Eqs. 4.21 and 4.22), respectively.

$$LE_S = Rn_S - G - H_S \,, \tag{4.21}$$

$$LE_C = Rn_C - H_C. \tag{4.22}$$

4.4.7 Temperature Components Estimation

In the TSEB-2T (a special implemented of TSEB), Ts and Tc are derived from fitting a linear function over the NDVI-Tr pairs in a contextual spatial domain, namely VI-Tr space, and exploring pure vegetation and soil/cover crop pixel values. Due to inconsistency between NDVI and Tr pixel resolutions (i.e., 15 cm vs. 60 cm), downscaling Tr from its original resolution into higher resolution would allow better estimations of Ts and Tc ([37]). Soil and canopy emissivity, LAI, albedo, fractional cover, measurement of canopy geometry characteristics (leaf width, canopy height), solar radiation, air temperature (Ta), wind speed, and vapor pressure are the other required inputs for the TSEB model. In this study, LAI, canopy height and fractional cover are estimated by VSSIXA ([4]). Other parameters either are internally calculated in the TSEB, such as albedo, or measured by instruments installed in the experimental field.

4.4.8 Data Analysis

The TSEB model is executed with both original Tr and DTr. Estimated fluxes by TSEB are evaluated using eddy covariance towers measurements based on evaluation metrics including: (1) coefficient of determination (R^2), (2) mean absolute error (MAE), (3) root mean square error (RMSE), and (4) relative root mean square error (RRMSE) (Eqs. 4.23–4.26).

$$R^2 = 1 - \frac{\sum_{i=1}^{n}(M_i - E_i)^2}{\sum_{i=1}^{n}(M_i - \bar{M_i})^2} \tag{4.23}$$

$$MAE = \frac{\sum_{i=1}^{n}|M_i - E_i|}{n} \tag{4.24}$$

$$RMSE = \sqrt{\frac{\sum_{i=1}^{n}(M_i - E_i)^2}{n}} \tag{4.25}$$

$$RRMSE = \frac{RMSE}{\bar{M}_i} \times 100 \tag{4.26}$$

in which, n is the number of records, M_i is an observation, E_i is estimated or predicted value, and $\bar{M}_i$ is the average of observations. R^2 is often used to estimate model performance and indicates how much variation of an output is explained by inputs. MAE is an indicator of average bias between observations and estimated values. MAE is less sensitive to outliers in outputs ([50]). RMSE is developed to show how concentrated the data points is around the fitted line ([19]). RRMSE as a dimensionless version of RMSE indicates excellent performance when $RRMSE < 10\%$, good performance if $10\% < RMSE < 20\%$, fair performance if $20\% < RMSE < 30\%$ and poor performance if $RRMSE > 30\%$ ([32]).

4.5 Results and Discussion

4.5.1 Sampling Method

Figure 4.7 shows the histogram of the thermal imagery (blue line), the histogram of 20% samples selected randomly from the thermal imagery (dashed red line), and the histogram of training data selected by the sampling algorithm (yellow line). In other words, the yellow line shows the histogram of training data based on the method developed in this study (clustering 20% samples and applying weights to each cluster). Sampling data (dashed red line) clearly follow the histogram pattern of the original Tr (blue line) since those samples are randomly selected from the entire image. Although random sampling techniques are more representative of the whole population, they select more samples from the classes with high frequency, which is not an efficient method for training the network of the machine learning algorithms or regression based models. In contrast, the new sampling approach significantly improves the sample size issue in low dense clusters by clustering multi-dimension input space to a one-dimensional input space and assigning weights to clusters based on the number of members in each cluster (higher weights for lower density clusters). This approach helped the sampling algorithm keep the important records that

are located in the left and right tails. In other words, instead of taking many samples (for example between 25 to 40 degrees Celsius) and overtraining the model, the sampling algorithm can adjust the number of samples and keep the important information that usually located at tails.

In training machine learning algorithms, overtraining the network with high-frequent samples can be avoided by keeping extreme values. Although the sampling pattern ends up similar to a uniform sampling method based on Tr, it should be noted that training samples in Fig 4.7 are not selected solely based on Tr. In other words, spikes and valleys in the yellow histogram indicate very low and very high sample size in clusters selected by the k-means approach based on the set of possible predictors in the downscaling algorithm.

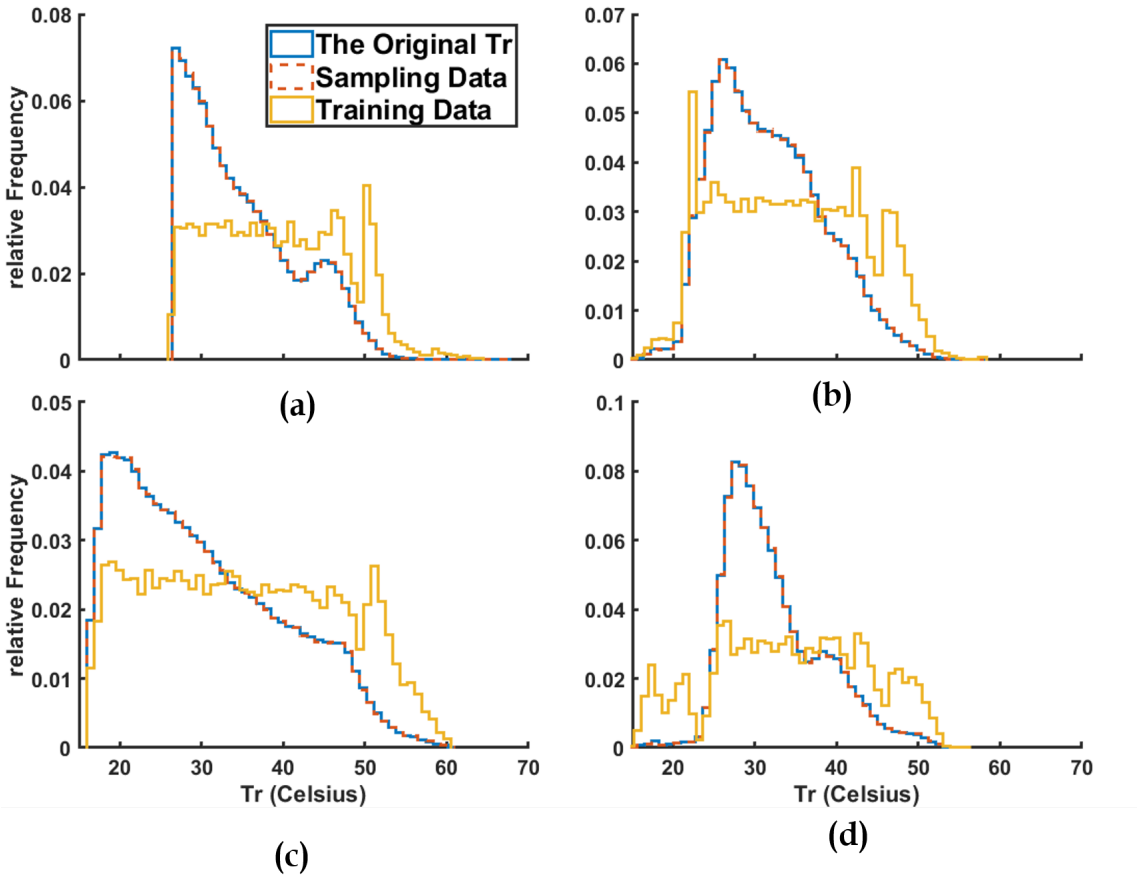

Fig. 4.7: Histograms of Tr for the original thermal image, sampling pixels, and training pixels

4.5.2 Downscaling Method

As discussed in the regression modules section, two types of regression models (linear-based and machine learning-based) are considered to simulate detail coefficients in Fig 4.5. The linear regression based models were LR, RLR, SLR, and ILR. The machine learning algorithms were DTR, DTER, SVM, and GPR, the hyper-parameters of which are tuned using a grid-search optimization algorithm. The performance of these eight models at both level 1 (L1) and level 2 (L2) over sampling points for each flight with 5-fold cross-validation are summarized in Table 4.3 -4.6.

Table 4.3: Performance of the models at two levels of decomposition for August 2014 flight

Model	**RMSE (°C)**		**R-squared**		**MSE (°C)**		**MAE (°C)**		**Prediction Speed (obs/sec)**		**Training time (second)**	
	L2	L1	L2	L1	L2	L1	L2	L1	L2	L1	L2	L1
LR	4.69	2.84	0.70	0.84	22.08	8.08	3.54	2.16	76,000	78,000	4.2	3.7
ILR	4.43	2.63	0.73	0.86	19.62	6.93	3.38	1.96	71,000	70,000	5.3	3.5
RLR	4.70	2.85	0.70	0.84	22.14	8.13	3.53	2.15	71,000	75,000	**5.1**	**4.4**
SLR	4.43	2.63	0.73	0.86	19.66	6.94	3.38	1.96	110,000	110,000	17.4	17.3
DTR	3.83	2.05	0.80	0.91	14.66	4.23	2.84	1.48	**550,000**	**550,000**	158.2	120.5
DTER	3.43	1.69	0.84	0.94	11.77	2.88	2.54	1.19	3,100	3,200	718.8	856.7
SVM	3.51	1.61	0.83	0.95	12.32	2.59	2.56	1.14	84,000	18,000	273.6	300.5
GPR	**3.35**	**1.43**	**0.85**	**0.96**	**11.27**	**2.05**	**2.48**	**1.01**	4,700	5,700	184.5	248.9

Table 4.4: Performance of the models at two levels of decomposition for June 2015 flight

Model	**RMSE (°C)**		**R-squared**		**MSE (°C)**		**MAE (°C)**		**Prediction Speed (obs/sec)**		**Training time (second)**	
	L2	L1	L2	L1	L2	L1	L2	L1	L2	L1	L2	L1
LR	4.88	3.14	0.68	0.79	23.84	9.86	3.59	2.25	78,000	300,000	4.8	0.8
ILR	5.16	3.35	0.64	0.76	26.66	11.22	3.35	2.02	72,000	180,000	4.9	0.6
RLR	5.04	3.34	0.65	0.76	25.45	11.17	3.51	2.18	78,000	310,000	**4.7**	**0.5**
SLR	4.66	3.35	0.7	0.76	21.79	11.24	3.33	2.02	120,000	230,000	17.9	15.9
DTR	4.00	2.29	0.78	0.89	16.06	5.27	2.95	1.68	**560,000**	**600,000**	152.9	138.2
DTER	3.56	1.92	0.83	0.92	12.70	3.68	2.62	1.43	2,900	2,900	869.51	717.1
SVM	3.61	1.83	0.82	0.93	13.06	3.37	2.60	1.34	13,000	16,000	293.6	14.6
GPR	**3.47**	**1.79**	**0.82**	**0.93**	**12.10**	**3.22**	**2.56**	**1.32**	5,400	5,700	169.47	187

Table 4.5: Performance of the models at two levels of decomposition for July 2015 flight

Model	**RMSE (°C)**		**R-squared**		**MSE (°C)**		**MAE (°C)**		**Prediction Speed (obs/sec)**		**Training time (second)**	
	L2	L1	L2	L1	L2	L1	L2	L1	L2	L1	L2	L1
LR	7.08	4.08	0.61	0.8	50.12	16.67	5.18	2.99	110,000	77,000	3.2	3.6
ILR	6.85	3.33	0.64	0.87	46.93	11.11	4.7	2.55	70,000	71,000	3.8	4.4
RLR	7.11	4.71	0.61	0.74	50.59	22.22	5.00	2.85	75,000	76,000	**3.7**	**4.2**
SLR	6.52	3.34	0.67	0.87	42.52	11.17	4.7	2.55	120,000	110,000	18.0	18.3
DTR	5.77	2.88	0.74	0.90	33.35	8.31	4.42	2.12	**580,000**	**540,000**	157.5	139.9
DTER	5.21	2.40	0.79	0.93	27.20	5.79	3.94	1.74	3,100	32,000	800.4	464.9
SVM	5.12	2.09	0.80	0.95	26.31	4.40	3.83	1.51	11,000	43,000	17.1	14.04
GPR	**4.96**	**2.01**	**0.81**	**0.95**	**24.64**	**4.05**	**3.78**	**1.44**	5,500	5,600	175.41	199.5

Table 4.6: Performance of the models at two levels of decomposition for May 2016 flight

Model	**RMSE (°C)**		**R-squared**		**MSE (°C)**		**MAE (°C)**		**Prediction Speed (obs/sec)**		**Training time (second)**	
	L2	L1	L2	L1	L2	L1	L2	L1	L2	L1	L2	L1
LR	6.29	5.31	0.55	0.58	39.56	28.24	4.93	4.09	80,000	80,000	4.9	4.8
ILR	4.00	3.06	0.82	0.86	16.05	9.40	2.90	2.22	81,000	79,000	**4.2**	**4.1**
RLR	6.38	9.58	0.53	0.38	40.76	91.92	4.88	4.00	80,000	79,000	5.3	4.4
SLR	4.00	3.06	0.82	0.86	16.06	9.40	2.91	2.22	120,000	120,000	6.4	6.8
DTR	2.85	1.54	0.91	0.96	8.17	2.39	2.07	1.06	**580,000**	**630,000**	134.8	118.4
DTER	2.62	1.31	0.92	0.97	6.83	1.73	1.89	0.91	3,200	87,000	699.3	122.73
SVM	2.68	1.28	0.92	0.98	7.18	1.66	1.94	0.93	14,000	23,000	14.2	12.14
GPR	**2.61**	**1.23**	**0.93**	**0.98**	**6.82**	**1.53**	**1.90**	**0.86**	5,500	5,700	186.5	182.95

According to Tables 4.3–4.6, LR and RLR models cannot be potential models for simulating Tr at different levels of wavelet decomposition since R-square is less than 70%. In terms of R-square, the performance of the other two linear based models are close to machine learning based algorithms. However, considering other statistics such as MSE, machine learning based algorithms provide closer values to observed Tr values. Linear regression based models can process 100,000 observations per second at each level, and they are faster than machine learning-based models. However, among all evaluated models, DTR with a processing speed of $\tilde{5}$00,000 per second was the fastest model. In terms of training time, linear regression-based models can be trained in less than 10 seconds, while the computation time for training machine learning networks with the same number of training samples, varies between 14 seconds (SVM) and more than 10 minutes (DTER). However, the training time of the SVM network in most cases is comparable to linear regression based models. GPR outperformed other models in all four flights, although, considering all statistics, no significant differences exist between DTER, SVM, and GPR.

Figs 4.8–4.9 shows scatter plots of simulated Tr using machine learning algorithms

against the original Tr. Compared to Level 2 (Fig 4.8, the first level of the simulation), the correlation between simulated and observed Tr in Level 1 is significantly more robust. A stronger correlation in Level 1 could be due to training and testing the models with the estimations of Tr generated by the inverse wavelet transform. In other words, some part of the Tr in Level 1 originated from detail coefficients of Tr at level 2 that are already trained with descriptors (Fig 4.5). Among these four algorithms in Level 2, DTR provides constant values for a different range of observed Tr, and scatterings around the 1–1 line of DTER and GPR are much less than DTR and SVM. However, at Level 2, the strip pattern of DTER disappears, and the performances of DTER, SVM and GPR are significantly improved, while different flight dates indicate significant differences between DTER, SVM and GPR .

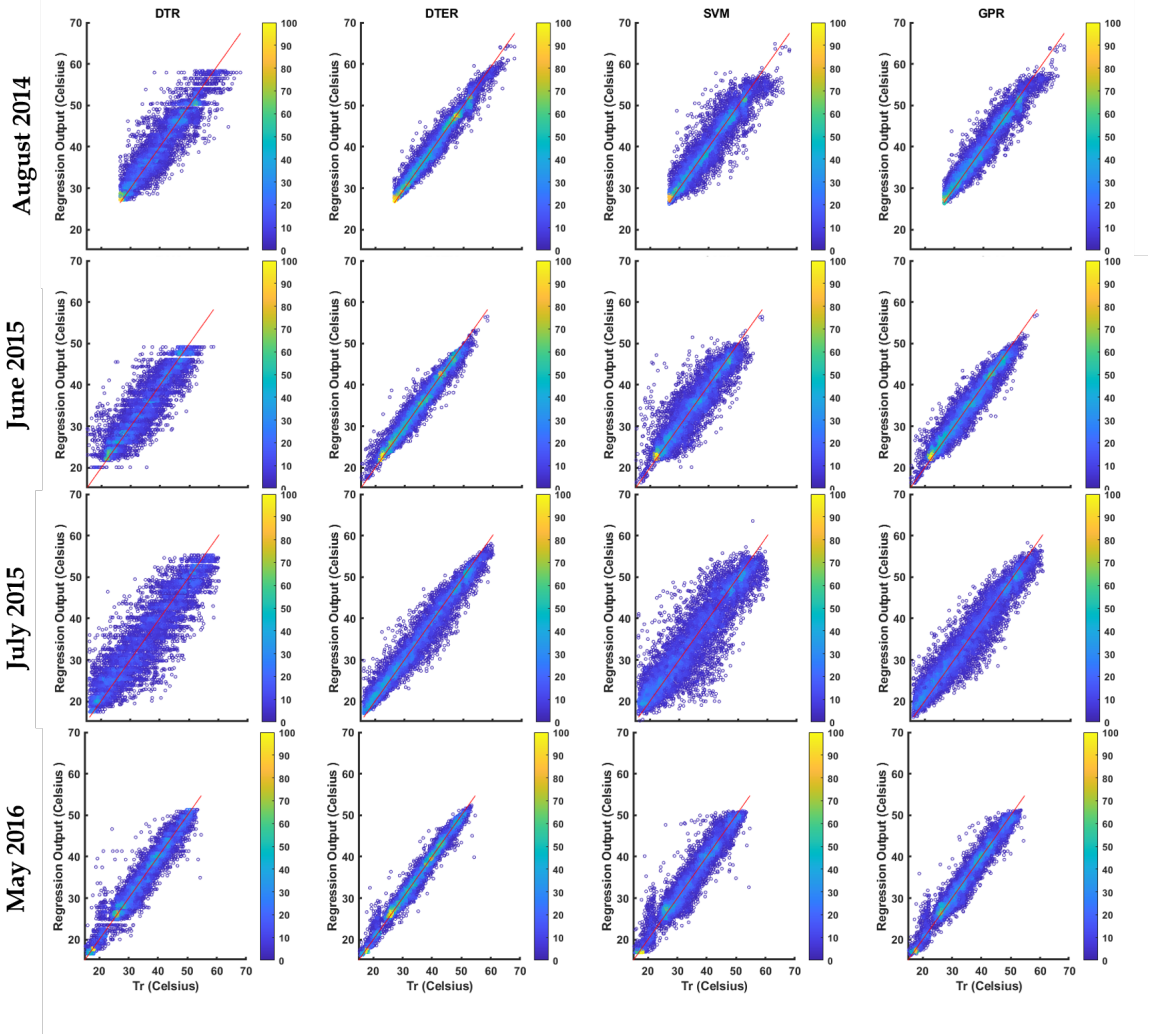

Fig. 4.8: Scatter plots of estimated Tr versus the original Tr at Level 2 for sampling records. Right colorbar indicates the Tr density, and the red line is 1–1 line

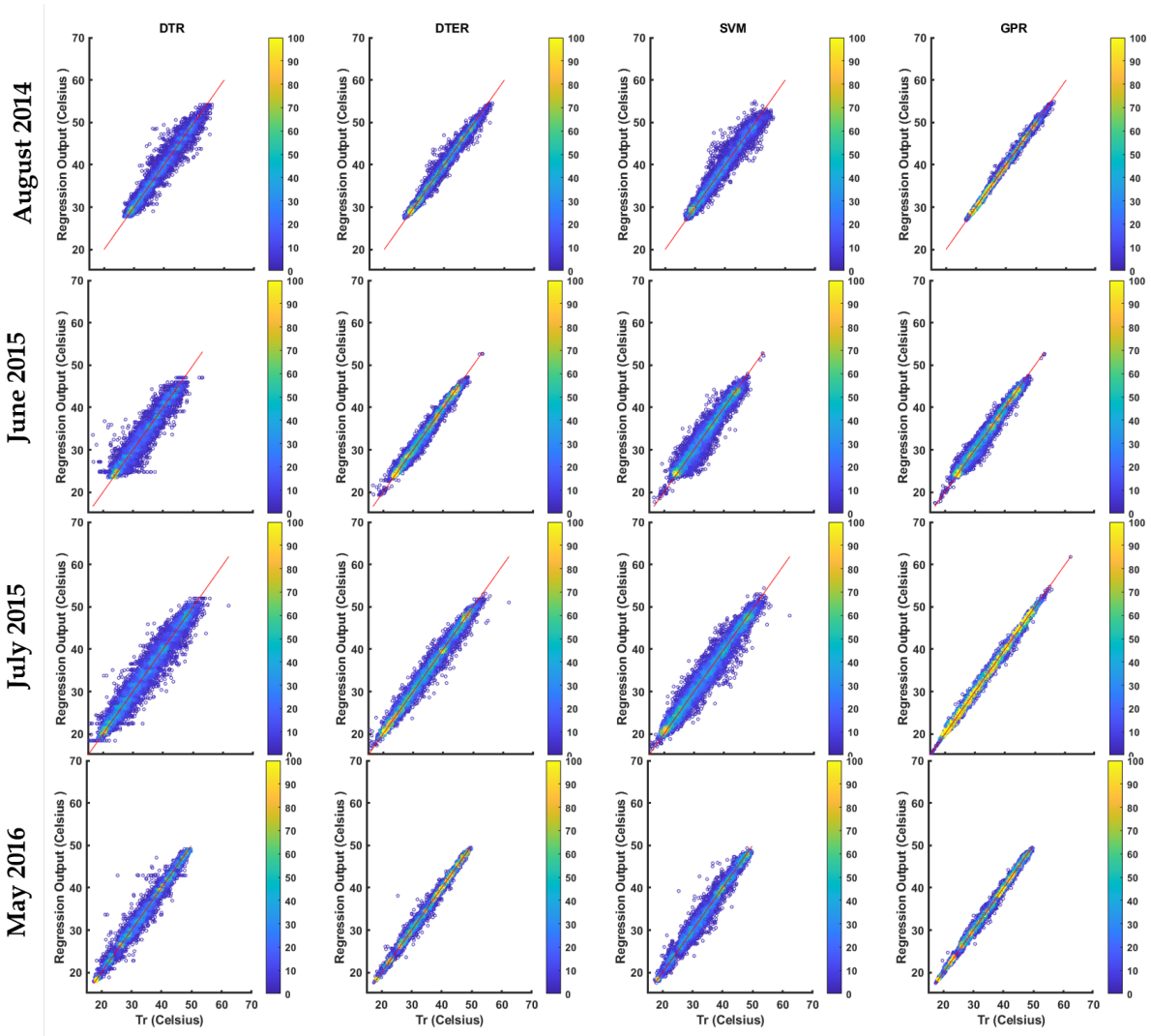

Fig. 4.9: Scatter plots of estimated Tr versus the original Tr at Level 1 for sampling records. Right colorbar indicates the Tr density and the red line is 1–1 line

According to Tables 4.3-4.6, GRP was slightly better than DTER and SVM in both levels based on the evaluation metrics. Thus, GPR is used in the downscaling algorithm, described in fig 4.5, to estimate DTr in each level. As Tr imagery at optical resolution does not exist in the study area, two figures illustrate the comparisons of the downscaling Tr algorithm's performance. In Fig 4.10, the DTr and the original Tr are aggregated in the footprint of IRT sensors, and then the aggregated values are compared with the in-situ Tr measurements by IRT sensors. Since the IRT sensors measure canopy and soil temperatures

separately, for this comparison, both original Tr and downscaled Tr must be separated into Ts and Tc. To derive Ts and Tc from Tr, the NDVI-Tr domain proposed by Nieto et al. (2019 [37]) is employed.

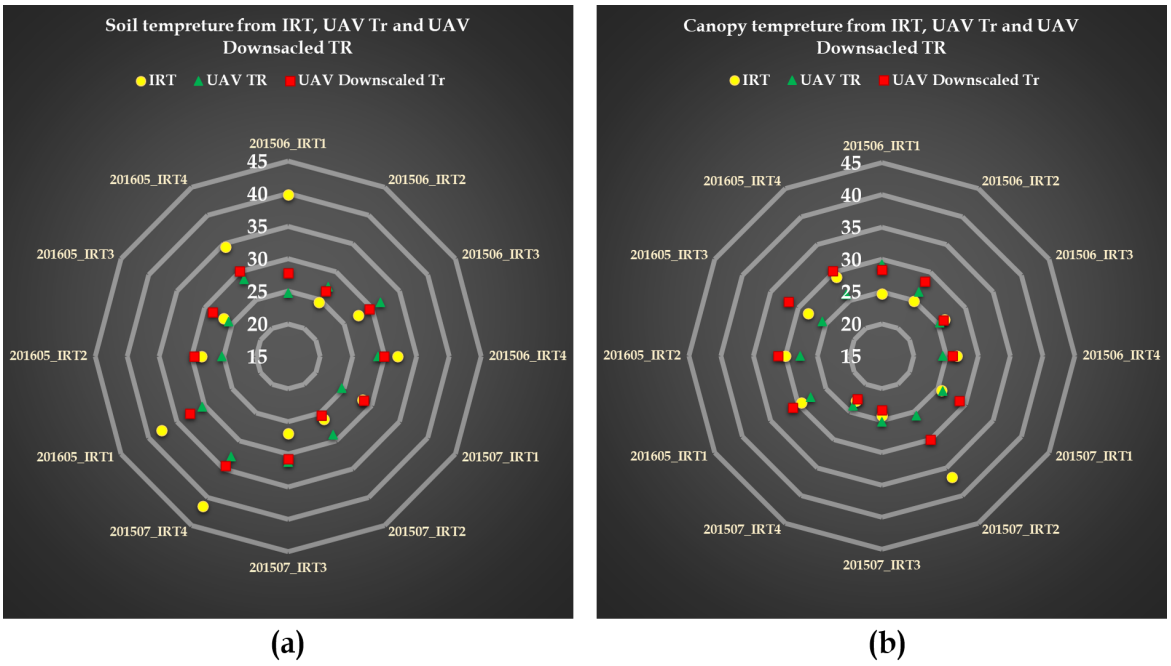

Fig. 4.10: The comparison between (a) soil and (b) canopy temperature measured by IRT against UAV Tr and UAV DTr within the IRT footprints for 2015 and 2016 flights

On average, the differences between IRT temperatures and UAV temperatures is about 1.5 and 5 degrees in soil and canopy components, respectively. In comparison with the original UAV Tr, downscaled UAV temperatures are, in general, closer to the measured IRT sensors, and the agreement between DTr points and IRT records is higher compared to the original Tr, which could be due to more accurate separation of Tr into Ts and Tc when DTr is used. In other words, if the correlation between DTr and NDVI is higher than that between the original Tr and NDVI, the temperature components estimated by the separation model are more accurate, and they should be closer to the IRT measurements. The impact of the DTr on Ts and Tc separation is discussed in the following section.

4.5.3 Impact of Downscaling Method on Ts and Tc

As discussed in the methodology, the TSEB model will start calculating fluxes for each canopy and soil component separately based on Ts and Tc estimated from a fitting regression model in an NDVI-Tr domain proposed by Nieto et al. (2019 [37]). The first assumption in this approach is that a linear relationship exists between NDVI and Tr if both are available at high-resolution (less than a meter). Since NDVI and Tr are not in the same resolution, increasing the resolution provides the opportunity to estimate Ts and Tc from the NDVI-Tr domain model without resampling and missing NDVI information. Fig 4.11 illustrates the role of the proposed downscaling method in the relationship between NDVI and Tr at different resolution and its impact on Ts and Tc, which are the key inputs for the TSEB model.

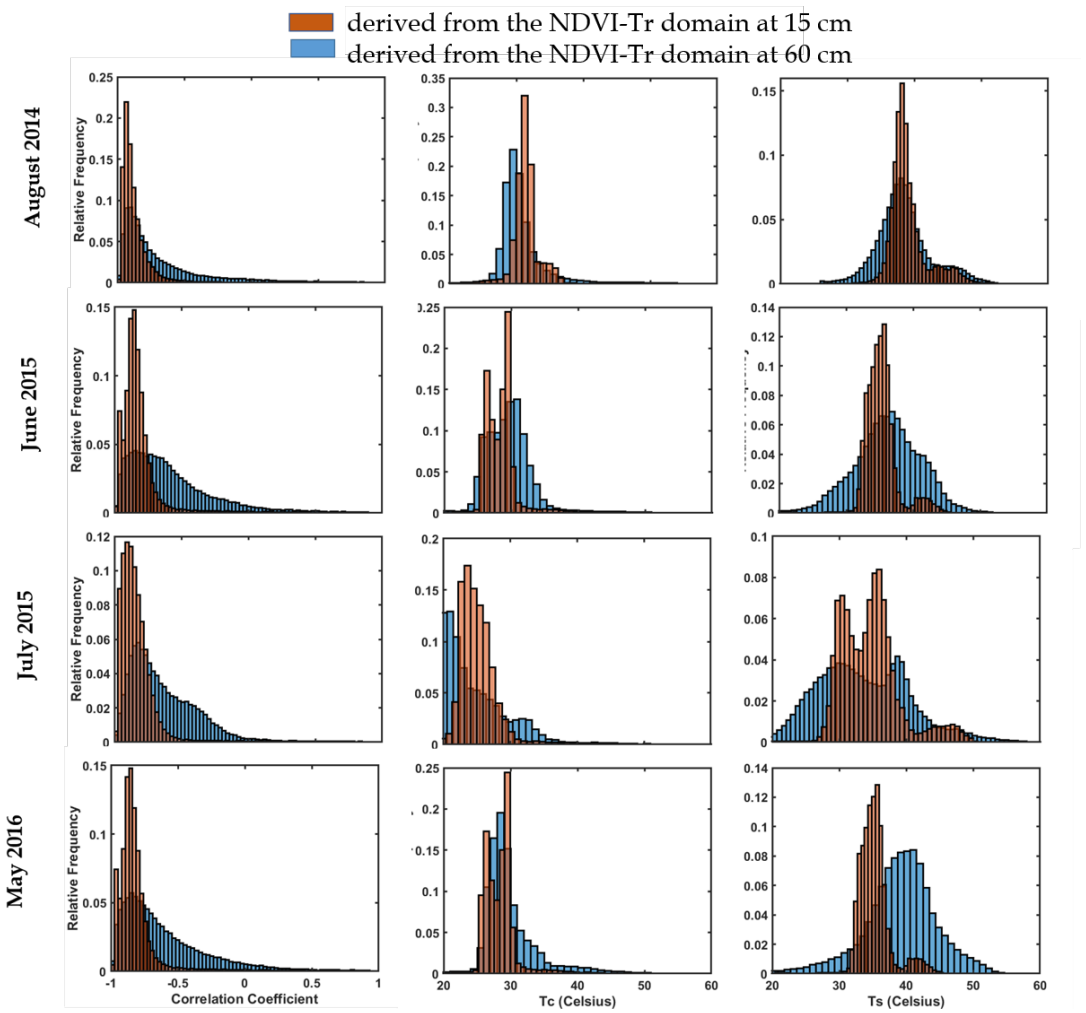

Fig. 4.11: The histogram of correlation coefficient between NDVI and original/DTr, and Ts and Tc estimated from NDVI and the original/DTr domain

In Fig 4.11, the histograms of correlation coefficient, along with Ts and Tc, are extracted for all NDVI-Tr domains (457x157 grids in this study). Fig 4.11 reveals that the correlation coefficient between NDVI and the DTr is significantly stronger than upscaled NDVI and the original Tr, confirming the assumption that higher resolution Tr leads to a stronger correlation between VIs and Tr. Changing the correlation coefficient in the NDVI-Tr domain may lead to a change in temperature components (Ts and Tc) extraction. In other words, by changing the slope and bias in the fitted linear equation, different Ts and Tc are estimated by the model. In all images, the correlation coefficients between NDVI and

DTr are less than -0.8. In contrast, this correlation ranges from 0 to -1 when it is computed between upscaled NDVI and the original Tr. Surprisingly, in some NDVI-Tr domains at the original Tr resolution in May 2016, positive correlations were found between NDVI and Tr that are likely due to growing cover crops in the interrows. In other words, if no pure soil pixels exist in the NDVI-Tr domain, all NDVI-Tr pairs belong to vegetation pixels (active cover crops and vines), and the inverse relationship between NDVI and Tr can change to a positive correlation. This positive relationship resulted in estimating higher temperatures for higher NDVI (vegetation pixel) and, consequently, lower temperatures for lower NDVI (soil pixels), which cannot be correct.

In contrast, the histograms indicate no positive correlation in NDVI and downscaling Tr, not only for May 2016 but for all flights. Applying the downscaling algorithm, it turns out that the NDVI-Tr domain contains enough soil pixels to keep the inverse relationship. Comparing Ts and Tc, the histogram shows less variation in temperatures estimated from NDVI-DTr domain. Additionally, it seems that, in the first two months of the growing season (May and June), Ts and Tc estimated from the DTr are respectively lower and higher than Ts and Tc from the original Tr resolution, whereas this pattern is not followed in July and August. In July and August, the peaks of the Ts histograms derived from the original Tr and DTr are close to one another, while Tc estimated from the DTr is slightly higher than Tc derived from the original NDVI-Tr domain.

4.5.4 TSEB Outputs

In addition to developing an efficient sampling algorithm for fitting models on big data, assessing the performance of a 2D wavelet transform with different machine learning algorithms for downscaling Tr, and analyzing the temperature separation algorithm at two different resolutions, the other objective of this study was to evaluate the impact of new DTr on remote sensing ET models. As described in the methodology, TSEB, one of the popular ET models, was selected as the base ET model for such evaluation because it is highly sensitive to temperature components and takes advantage of Ts and Tc for distributing energy fluxes between two different components. However, the sensitivity of the TSEB

model to higher Tr resolution is still untested. Therefore, two scenarios are defined to evaluate the performance of the TSEB model. In the first scenario, Ts and Tc estimated at the original Tr resolution are fed to the TSEB. In other words, NDVI is aggregated at Tr resolution (from 15 cm to 60 cm) and Ts and Tc in each grid (3.6 m by 3.6 m) are estimated from a regression model fitted over 36 points, whereas, in the second scenario, Ts and Tc are estimated using the same approach but from a domain populated with 576 NDVI-DTr pairs [(3.6×3.6) /(0.15×0.15) = 24 × 24 = 576]. TSEB is executed with Ts and Tc components derived from NDVI-Tr and NDVI-DTr domains and its outputs are compared with the fluxes measured by ECs installed in northern and southern blocks of the study area (Fig 4.2). The outputs of the TSEB model for those scenarios against EC are illustrated in Fig 4.12, and the statistics of this comparison are summarized in Table 4.7.

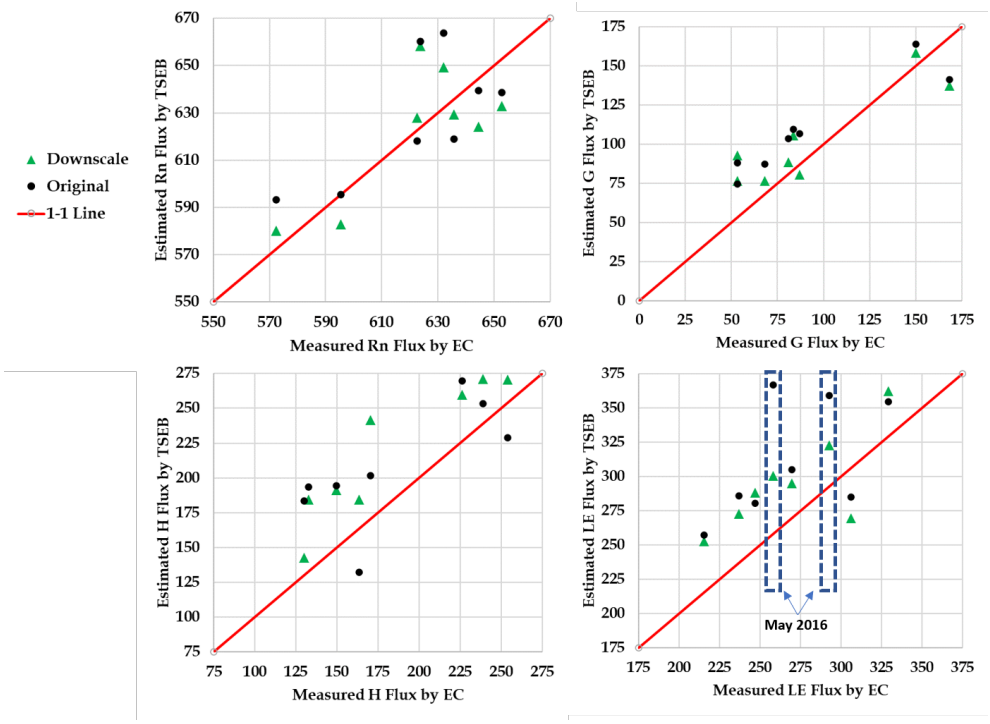

Fig. 4.12: Scatterplot of observed vs. estimated fluxes using the different scenarios. All fluxes are in W/m^2

Table 4.7: Performance of the TSEB model based on the original Tr (S1) and DTr (S2) for each energy flux component (units in W/m^2)

Variable	Scenario	MAE	RMSE	RRMSE
Rn	S1	16.29	20.54	3.30
	S2	16.18	18.62	2.99
G	S1	22.52	23.41	25.21
	S2	18.53	21.69	23.35
H	S1	38.29	40.95	22.41
	S2	36.77	40.97	22.42
LE	S1	47.61	54.51	20.26
	S2	35.84	36.31	13.50

Although results show an overestimation in H and LE and an underestimation in Rn, there is a good agreement between measured fluxes from ECs and TSEB outputs. As shown in Fig 4.12 and Table 4.7, the impact of downscaling Tr is more apparent in G and LE. In general, the biases in G for S1 could be due to TSEB implementing a non-calibrated empirical equation between net radiation reaching to the soil (Rns) and G ($G = 0.35 * R_{ns}$). However, it turns out that the biases in G for S2 are slightly improved when DTr is fed to the model. In the TSEB model, Rns is computed based on net longwave and shortwave radiation reaching the soil (Lns and Sns, respectively). LAI is the most important component in Sns, and using DTr instead of Tr may not affect this parameter. However, Lns is estimated based on long emissions from canopy and soil that both are a function of Ts and Tc to the power of 4. Therefore, seeing the impact of DTr in G and consequently in Rn is expected since total Rn is a summation of net radiation separately estimated for soil and canopy. Since Rn estimates were acceptable with using both DTr and Tr as inputs, the improvements in G led to a better estimation of the total available energy

($Rn - G$). Although using DTr instead of Tr did not lead to a significant improvement in H estimates, the better $Rn - G$ estimates resulted in more accurate LE estimates. Since G affects only LE_S (4.21), improvements in LE should be due to LE_S estimates not LE_C. Interestingly, we found better LE_S estimates at periods when there was an active cover crop in the inter-rows (4.12, see arrows to green points which are results for May 2016.) Therefore, the impact of DTr in the TSEB model would be more pronounced in separation of LE estimates into LE_S and LE_C, specifically when there is an active cover in inter-rows.

4.6 Conclusions

In this study, a coupled 2D wavelet and machine learning algorithm is used to downscale Tr from its original resolution to optical band resolutions. Since training and testing the machine learning algorithm with the entire image was not possible, a new sampling algorithm was developed. In the sampling algorithm, the entire image with all bands is clustered to several classes using the k-means approach. Samples are selected from each cluster using a weighted approach. The sampling algorithm can significantly increase the speed of internal computations since the speed of training of the machine learning algorithms is sensitive to the size of training data sets. Although the coupled 2D wavelet and machine learning algorithm is still a computationally expensive algorithm compared to fitting regression models between VIs and Tr at lower resolutions, it is a practical method that can be automated and implemented on remotely sensed thermal images after applying image processing steps. Similar to VIs-Tr fitting models, however, the wavelet-machine learning algorithm only requires higher resolution of visible and near-infrared bands.

Results confirmed that the proposed sampling algorithm could keep most extreme members from the population while minimizing the training size. Among all machine learning algorithms tested for exploring the relationship between optical-band-derived information and Tr, the GPR, SVM, and DTER algorithms are more accurate than the others, while DTR was the fastest model in terms of prediction speed, and linear-based models were the fastest in terms of the training time. Original Tr and DTr are compared with the IRT sensors installed in the field, and results indicated a higher agreement between DTr and

IRT measurements for soil component.

Results revealed that the correlation between NDVI and DTr in the 3.6-m grid is significantly higher than the correlation between the original Tr and NDVI. Stronger correlation may lead to more accurate Ts and Tc estimates. Two scenarios are defined to assess the impact of the DTr on the TSEB outputs. In the first scenario, TSEB is executed with Ts and Tc estimated from the NDVI-Tr domain, and in the second scenario, DTr is used for the separation of temperature components. Comparing the TSEB outputs based on these two scenarios against EC measurements showed that Rn and H are less sensitive to DTr while DTr can affect G and consequently LE_S. The improvements in LE_S resulted in a better estimation of LE, specifically when there is an active cover crop in inter-rows (May 2016).

Bibliography

[1] Aboutalebi, M. Discussion of Equation to Predict Riverine Transport of Suddenly Discharged Pollutants by Mostafa Farhadian, Omid Bozorg-Haddad, Samaneh Seifollahi-Aghmiuini, and Hugo A. Loiciga. *Journal of Irrigation and Drainage Engineering*, 144(4):07018010, 2018.

[2] Aboutalebi, M., Bozorg Haddad, O., and Loáiciga, H. A. Optimal Monthly Reservoir Operation Rules for Hydropower Generation Derived with SVR-NSGAII. *Journal of Water Resources Planning and Management*, 141(11):04015029, 2015.

[3] Aboutalebi, M., Bozorg Haddad, O., and Loáiciga, H. A. Application of the SVR-NSGAII to Hydrograph Routing in Open Channels. *Journal of Irrigation and Drainage Engineering*, 142(3):04015061, 2016.

[4] Aboutalebi, M., Torres-Rua, A. F., McKee, M., Kustas, W. P., Nieto, H., Alsina, M. M., White, A., Prueger, J., McKee, L., Alfieri, J., Hipps, L., Coopmans, C., and Dokoozlian, N. Incorporation of Unmanned Aerial Vehicle (UAV) Point Cloud Products into Remote Sensing Evapotranspiration Models. *Remote Sensing*, 12(1), 2019.

[5] Aboutalebi, M., Torres-Rua, A. F., McKee, M., Nieto, H., Kustas, W. P., Prueger, J. H., McKee, L., Alfieri, J. G., Hipps, L., and Coopmans, C. Assessment of Landsat Harmonized sUAS Reflectance Products Using Point Spread Function (PSF) on Vegetation Indices (VIs) and Evapotranspiration (ET) Using the Two-Source Energy Balance (TSEB) Model. *AGU Fall Meeting Abstracts*, 2018.

[6] Agam, N., Kustas, W. P., Anderson, M. C., Li, F., and Neale, C. M.U. A Vegetation Index Based Technique for Spatial Sharpening of Thermal Imagery. *Remote Sensing of Environment*, 107(4):545 – 558, 2007.

[7] AgiSoft, L. L. C., and Russia St Petersburg. Agisoft photoscan.

[8] Anderson, M. C., Norman, J. M., Mecikalski, J. R., Torn, R. D., Kustas, W. P., and Basara, J. B. A Multiscale Remote Sensing Model for Disaggregating Regional Fluxes to Micrometeorological Scales. *Journal of Hydrometeorology*, 5(2):343–363, 2004.

[9] Bechtel, B., Zakšek, K., and Hoshyaripour, G. Downscaling Land Surface Temperature in an Urban Area: A Case Study for Hamburg, Germany. *Remote Sensing*, 4(10):3184–3200, 2012.

[10] Bindhu, V.M., Narasimhan, B., and Sudheer, K.P. Development and Verification of a Non-linear Disaggregation Method (NL-DisTrad) to Downscale MODIS Land Surface Temperature to the Spatial Scale of Landsat Thermal Data to Estimate Evapotranspiration. *Remote Sensing of Environment*, 135:118 – 129, 2013.

[11] Bonafoni, S. Downscaling of Landsat and MODIS Land Surface Temperature Over the Heterogeneous Urban Area of Milan. *IEEE Journal of Selected Topics in Applied Earth Observations and Remote Sensing*, 9(5):2019–2027, May 2016.

[12] Bruce, L. M., Koger, C. H., and Jiang Li. Dimensionality Reduction of Hyperspectral Data Using Discrete Wavelet Transform Feature Extraction. *IEEE Transactions on Geoscience and Remote Sensing*, 40(10):2331–2338, Oct 2002.

[13] Brunsell, N. A. and Gillies, R. R. Determination of Scaling Characteristics of AVHRR Data With Wavelets: Application to SGP97. *International Journal of Remote Sensing*, 24(14):2945–2957, 2003.

[14] Campbell, G.S. and Norman, J.M. *An Introduction to Environmental Biophysics*. Modern Acoustics and Signal. Springer New York, 2000.

[15] Chen, S., Su, H., Zhang, R., and Tian, J. Fusing Remote Sensing Images Using À Trous Wavelet Transform and Empirical Mode Decomposition. *Pattern Recognition Letters*, 29(3):330 – 342, 2008.

[16] Cohen, A. Ten Lectures on Wavelets, CBMS-NSF Regional Conference Series in Applied Mathematics. *Journal of Approximation Theory*, 78(3):460 – 461, 1994.

[17] Crowther, B.G. *Radiometric Calibration of Multispectral Video Imagery.* PhD thesis, Utah State University, 1992.

[18] Dennison, P. E., Charoensiri, K., Roberts, D. A., Peterson, S. H., and Green, R. O. Wildfire Temperature and Land Cover Modeling Using Hyperspectral Data. *Remote Sensing of Environment*, 100(2):212 – 222, 2006.

[19] Despotovic, M., Nedic, V., Despotovic, D., and Cvetanovic, S. Evaluation of Empirical Models for Predicting Monthly Mean Horizontal Diffuse Solar Radiation. *Renewable and Sustainable Energy Reviews*, 56:246 – 260, 2016.

[20] Ebden, M. Gaussian Processes for Regression: A Quick Introduction. 2008.

[21] Elarab, Manal, Ticlavilca, Andres M, Torres-Rua, Alfonso F., Maslova, Inga, and McKee, Mac. Estimating Chlorophyll With Thermal and Broadband Multispectral High Resolution Imagery From an Unmanned Aerial System Using Relevance Vector Machines for Precision Agriculture. *International Journal of Applied Earth Observation and Geoinformation*, 43:32–42, 2015. Special Issue on "Advances in remote sensing of vegetation function and traits".

[22] Essa, W., van der Kwast, J., Verbeiren, B., and Batelaan, O. Downscaling of Thermal Images Over Urban Areas Using the Land Surface Temperature–impervious Percentage Relationship. *International Journal of Applied Earth Observation and Geoinformation*, 23:95 – 108, 2013.

[23] Gao, F., Kustas, W. P., and Anderson, M. C. A Data Mining Approach for Sharpening Thermal Satellite Imagery over Land. *Remote Sensing*, 4(11):3287–3319, 2012.

[24] Inamdar, A. K. and French, A. Disaggregation of GOES Land Surface Temperatures Using Surface Emissivity. *Geophysical Research Letters*, 36(2), 2009.

[25] Inamdar, A. K., French, A., Hook, S., Vaughan, G., and Luckett, W. Land Surface Temperature Retrieval at High Spatial and Temporal Resolutions Over the Southwestern United States. *Journal of Geophysical Research: Atmospheres*, 113(D7), 2008.

[26] Kaheil, Y. H., Rosero, E., Gill, M. K., McKee, M., and Bastidas, L. A. Downscaling and Forecasting of Evapotranspiration Using a Synthetic Model of Wavelets and Support Vector Machines. *IEEE Transactions on Geoscience and Remote Sensing*, 46(9):2692–2707, Sep. 2008.

[27] Kumar, P. and Foufoula-Georgiou, E. A Multicomponent Decomposition of Spatial Rainfall Fields: 1. Segregation of Large- and Small-scale Features Using Wavelet Transforms. *Water Resources Research*, 29(8):2515–2532, 1993.

[28] Kustas, W. P., Anderson, M. C., Alfieri, J. G., Knipper, K., Torres-Rua, A., Parry, C. K., Nieto, H., Agam, N., White, W. A., Gao, F., McKee, L., Prueger, J. H., Hipps, L. E., Los, S., Alsina, M. M., Sanchez, L., Sams, B., Dokoozlian, N., McKee, M., Jones, S., Yang, Y., Wilson, T. G., Lei, F., McElrone, A., Heitman, J. L., Howard, A. M., Post, K., Melton, F., and Hain, C. The Grape Remote Sensing Atmospheric Profile and Evapotranspiration Experiment. *Bulletin of the American Meteorological Society*, 99(9):1791–1812, 2018.

[29] Kustas, W. P. and Norman, J. M. Evaluation of Soil and Vegetation Heat Flux Predictions Using a Simple Two-source Model With Radiometric Temperatures for Partial Canopy Cover. *Agricultural and Forest Meteorology*, 94(1):13 – 29, 1999.

[30] Kustas, W. P., Norman, J. M., Anderson, M. C., and French, A. N. Estimating Subpixel Surface Temperatures and Energy Fluxes From the Vegetation Index–radiometric Temperature Relationship. *Remote Sensing of Environment*, 85(4):429 – 440, 2003.

[31] Li, B., Yang, R., and Jiang, H. Remote-Sensing Image Compression Using Two-Dimensional Oriented Wavelet Transform. *IEEE Transactions on Geoscience and Remote Sensing*, 49(1):236–250, Jan 2011.

[32] Li, M., Tang, X., Wu, W., and Liu, H. General Models for Estimating Daily Global Solar Radiation for Different Solar Radiation Zones in Mainland China. *Energy Conversion and Management*, 70:139 – 148, 2013.

[33] Liu, H., Wang, L., and Jezek, K. C. Wavelet-transform Based Edge Detection Approach to Derivation of Snowmelt Onset, End and Duration From Satellite Passive Microwave Measurements. *International Journal of Remote Sensing*, 26(21):4639–4660, 2005.

[34] Miura, T and Huete, AR. Performance of Three Reflectance Calibration Methods for Airborne Hyperspectral Spectrometer Data. *Sensors (Basel)*, 9(2):794–813, 2009.

[35] Neale, C. M.U. and Crowther, B. G. An Airborne Multispectral Video/radiometer Remote Sensing System: Development and Calibration. *Remote Sensing of Environment*, 49(3):187 – 194, 1994.

[36] Nemani, R., Pierce, L., Running, S., and Goward, S. Developing Satellite-derived Estimates of Surface Moisture Status. *Journal of Applied Meteorology*, 32(3):548–557, 1993.

[37] Nieto, H., Kustas, W. P., Torres-Rúa, A., Alfieri, J. G., Gao, F., Anderson, M. C., White, W. A., Song, L., Alsina, M. M., Prueger, J. H., McKee, M., Elarab, M., and McKee, L. G. Evaluation of TSEB Turbulent Fluxes Using Different Methods for the Retrieval of Soil and Canopy Component Temperatures From UAV Thermal and Multispectral Imagery. *Irrigation Science*, 37(3):389–406, May 2019.

[38] Pelgrum, H., Schmugge, T., Rango, A., Ritchie, J., and Kustas, W. Length-scale Analysis of Surface Albedo, Temperature, and Normalized Difference Vegetation Index in Desert Grassland. *Water Resources Research*, 36(7):1757–1765, 2000.

[39] Rasmussen, CE. and Williams, CKI. *Gaussian Processes for Machine Learning*. Adaptive Computation and Machine Learning. MIT Press, Cambridge, MA, USA, January 2006.

[40] Schulz, E., Speekenbrink, M., and Krause, A. A Tutorial on Gaussian Process Regression: Modelling, Exploring, and Exploiting Functions. *Journal of Mathematical Psychology*, 85:1 – 16, 2018.

[41] Song, C., Jia, L., and Menenti, M. Retrieving High-Resolution Surface Soil Moisture by Downscaling AMSR-E Brightness Temperature Using MODIS LST and NDVI Data. *IEEE Journal of Selected Topics in Applied Earth Observations and Remote Sensing*, 7(3):935–942, March 2014.

[42] Strahler, A. H., Woodcock, C. E., and Smith, J. A. On the Nature of Models in Remote Sensing. *Remote Sensing of Environment*, 20(2):121 – 139, 1986.

[43] Tello Alonso, M., Lopez-Martinez, C., Mallorqui, J. J., and Salembier, P. Edge Enhancement Algorithm Based on the Wavelet Transform for Automatic Edge Detection in SAR Images. *IEEE Transactions on Geoscience and Remote Sensing*, 49(1):222–235, Jan 2011.

[44] Torres-Rua, A. Vicarious Calibration of sUAS Microbolometer Temperature Imagery for Estimation of Radiometric Land Surface Temperature. *Sensors*, 17(7), 2017.

[45] Twine, T.E., Kustas, W.P., Norman, J.M., Cook, D.R., Houser, P.R., Meyers, T.P., Prueger, J.H., Starks, P.J., and Wesely, M.L. Correcting Eddy-Covariance Flux Underestimates over a Grassland. *Agricultural and Forest Meteorology*, 103(3):279 – 300, 2000.

[46] Vapnik, V. N. *The Nature of Statistical Learning Theory.* Springer-Verlag, Berlin, Heidelberg, 1995.

[47] Vapnik, V. N. *Statistical Learning Theory.* Wiley-Interscience, 1998.

[48] Voogt, J.A and Oke, T.R. Thermal Remote Sensing of Urban Climates. *Remote Sensing of Environment*, 86(3):370 – 384, 2003. Urban Remote Sensing.

[49] White, W. A., Alsina, M. M., Nieto, H., McKee, L. G., Gao, F., and Kustas, W. P. Determining a Robust Indirect Measurement of Leaf Area Index in California Vineyards for Validating Remote Sensing-based Retrievals. *Irrigation Science*, 37:269–280, 2018.

[50] Willmott, C. J. and Matsuura, K. Advantages of the Mean Absolute Error (MAE) Over the Root Mean Square Error (RMSE) in Assessing Average Model Performance. *Climate Research*, 30(1):79–82, 2005.

[51] Yang, G., Pu, R., Huang, W., Wang, J., and Zhao, C. A Novel Method to Estimate Subpixel Temperature by Fusing Solar-Reflective and Thermal-Infrared Remote-Sensing Data With an Artificial Neural Network. *IEEE Transactions on Geoscience and Remote Sensing*, 48(4):2170–2178, April 2010.

[52] Yang, G., Pu, R., Zhao, C., Huang, W., and Wang, J. Estimation of Subpixel Land Surface Temperature Using an Endmember Index Based Technique: a Case Examination on ASTER and MODIS Temperature Products Over a Heterogeneous Area. *Remote Sensing of Environment*, 115(5):1202 – 1219, 2011.

[53] Zakšek, K. and Oštir, K. Downscaling Land Surface Temperature for Urban Heat Island Diurnal Cycle Analysis. *Remote Sensing of Environment*, 117:114 – 124, 2012. Remote Sensing of Urban Environments.

[54] Zhan, W., Chen, Y., Zhou, J., Wang, J., Liu, W., Voogt, J., Zhu, X., Quan, J., and Li, J. Disaggregation of Remotely Sensed Land Surface Temperature: Literature Survey, Taxonomy, Issues, and Caveats. *Remote Sensing of Environment*, 131:119 – 139, 2013.

[55] Zhao, H. and Chen, X. Use of Normalized Difference Bareness Index in Quickly Mapping Bare Areas from TM/ETM+. In *Proceedings. 2005 IEEE International Geoscience and Remote Sensing Symposium, 2005. IGARSS '05.*, volume 3, pages 1666–1668, July 2005.

[56] Zhou, J., Civco, D. L., and Silander, J. A. A Wavelet Transform Method to Merge Landsat TM and SPOT Panchromatic Data. *International Journal of Remote Sensing*, 19(4):743–757, 1998.

CHAPTER 5

Conclusions

Considering the climate change, increasing population, and the high pressure on groundwater, one of the main concerns in precision agriculture is increasing the water use efficiency and optimizing irrigation systems to improve crop yield and maintain quality.

During these years, several irrigation systems have been developed by engineers for improving irrigation systems based on different purposes. For example, a variable rate drip irrigation (VRDI) concept was developed to reduce yield and fruit quality variability, particularly in vineyards. In this concept, the vineyard is divided into different irrigation zones (e.g., 30 x 30-meter, Landsat pixel resolution), allowing individual irrigation for each zone. VRDI assumes that the observed variability in yield and fruit quality can be managed by different applied water for the plant-based on soil variability. VRDI is an efficient irrigation system for reaching full yield potential. However, there is an open question as to how to optimally use this system to improve yield and quality improvement and reduce variability" because the operation of VRDI requires reliable and frequent ET estimates at the grid size of VRDI.

As discussed above, having accurate ET maps is essential for irrigation systems and particularly for optimized irrigation scheduling. Emerging and developing remote sensing platforms such as satellites and UAVs provide a unique opportunity for estimation and mapping of ET. Several remote sensing-based models have been developed to estimate ET as a residual in the energy balance equation in the past decade. TSEB, SEBAL, Alexi, DisAlexi, and METIRC are popular models among them. Although these models have been developed based on physical and semi-empirical equations, uncertainties in their inputs can significantly affect their performance.

These inputs include land cover, wind speed and direction, LAI, air temperature, and LST. Wind speed, wind direction, and air temperature are obtained from the weather

station and numerical models. However, the land cover, LAI, and LST inputs are estimated from remote sensing platforms (satellites and UAVs). More specifically, land cover maps can be achieved by applying supervised classification methods. LAI maps are indirectly estimated by fitting an empirical equation between in-situ LAI measurements and VIs. LST can be estimated based on the radiant temperature measured by the thermal sensor. Although each input can be considered as a potential source of uncertainty to ET models, investigations show that remote sensing based ET models (particularly the TSEB model) are more sensitive to LAI and LST.

The sources of uncertainties in LAI can be classified into three categories: in-situ LAI measurements, mixed information in VIs calculation, and the fitting models between in-situ LAIs and VIs. Among these categories, the uncertainties in LAI measurements have been described in previous studies. However, the uncertainties in VIs and fitting models have not been addressed yet. The main factor that can lead to increasing uncertainties in VIs is the coarse spatial resolution of the satellite imagery where signals of different objects are aggregated over a pixel (e.g., 30m in Landsat data). For instance, the NDVI value for one pixel at 30-m in vineyards can be a combination of shaded and sunlit areas of vegetation and soil. In vineyards, canopy height, row orientation, and topography can lead to different patterns of shadows on objects. The appearance of shadows due to canopy height and row orientation may not be visible and detectable in the signal received by satellites. Since shadows can affect VIs (e.g., reduction in NDVI), fitting regression models between VIs and observed LAI must be applied based on "shadow-free" imagery. Shadow-free imagery means detection and removal of shaded pixels from the original imagery. This process requires super-high resolution imagery that UAVs can provide. Among popular methods for detecting objects, we found that both supervised and index-based methods outperformed others.

Another solution to reduce the uncertainty in LAI models is to incorporate vineyard 3D structure information. Despite satellites, UAVs can capture multiple imagery at different angles from objects. Overlapping those images along with implementing the Structure from

Motion algorithm provides a 3D database called “Point Cloud”. A dense point cloud is a valuable database for LAI models because it is not affected by shadows. Secondly, it provides information about canopy geometry and canopy structure such as canopy height, canopy surface area, and canopy volume. Although extraction of canopy geometry and structure from point cloud requires advanced algorithms being developed and run on high-performance computing systems, it can provide parameters that are physically linked to the definition of LAI (the one-sided green leaf area per unit ground surface area). Our results showed that the combination VIs and canopy structural information along with a non-linear fitted model can achieve the most accurate LAI model. However, a significant effort is necessary to enhance the speed of the computational process.

Concerning the second main input for remote sensing ET models, LST, there is a similar story about mixed pixel information. Although the mixed information in thermal signals is more highlighted at satellite pixel resolutions, 50 cm to 1 m resolution of UAVs thermal imagery can even contain mixed pixels. For example, 50 cm resolution of thermal imagery in vineyards could be a combination of shaded and sunlit pixels of leaves, soil, and cover crops. Thus, higher thermal imagery by UAVs is still needed. UAV thermal imagery at the vine level plays an important role in vine water stress, virus detection, separation of ET into evaporation and transpiration components, and separation of active cover crops from green pixels of vines, specifically in the early growing season. In addition to the importance of higher resolution of UAV thermal imagery for different purposes, higher thermal resolution of satellites with a daily repeat cycle is imperative. In the operational mode of an irrigation system such as VRDI, relying on one snapshot every other week from Landsat 8 is not sufficient. In contrast, LST and ET at 500 m to 1 Km spatial resolution from satellites providing daily images are not useful for monitoring water consumption at the field level. One solution to overcome this issue is to develop a reliable downscaling approach providing higher resolution of thermal imagery using satellites providing daily LST. In the near future, the availability of more robust downscaling algorithms, data fusion, and data assimilation will provide reliable daily ET, which is a key for the operational mode of irrigation systems.

To sum up, several models can estimate ET using remotely sensed information and climatic data. Still, providing reliable estimates of LAI and LST, the critical inputs for these models, is challenging. Satellites will continue playing an essential role in delivering more frequent geospatial information, particularly LST. Thus, the application of downscaling methods on daily LST images will be more pronounced. On the other hand, more advanced and cheaper UAVs and sensors will be developed to carry heavier sensors and batteries and to cover more than 10,000 acres in a single flight. Also, faster algorithms that take advantage of the point cloud, LiDAR, high-resolution imagery, and machine learning algorithms will be developed to model LAI. Thus, satellites and UAVs will be used together to advance ET models from the "experimental version" to the operational mode for more accurate irrigation scheduling

Appendices

06/02/2021

To Whom It May Concern:

I hereby give permission to Mahyar Aboutalebi to reprint the following material in his dissertation:

Aboutalebi, M.; Torres-Rua, A.F.; McKee, M.; Kustas, W.P.; Nieto, H.; Alsina, M.M.; White, A.; Prueger, J.H.; McKee, L.; Alfieri, J.; Hipps, L.; Coopmans, C.; Dokoozlian, N. Incorporation of Unmanned Aerial Vehicle (UAV) Point Cloud Products into Remote Sensing Evapotranspiration Models. Remote Sens. 2020, 12, 50. https://doi.org/10.3390/rs12010050

Sincerely,

Maria del Mar Alsina Marti

06/02/2021

To Whom It May Concern:

I hereby give permission to Mahyar Aboutalebi to reprint the following material in his dissertation:

Aboutalebi, M.; Torres-Rua, A.F.; McKee, M.; Kustas, W.P.; Nieto, H.; Alsina, M.M.; Sanchez, L.; Prueger, J.H.; McKee, L.; Alfieri, J.; Hipps, L.; Coopmans, C.; Dokoozlian, N. Downscaling UAV Land Surface Temperature using a Coupled Wavelet-Machine Learning-Optimization Algorithm and Its Impact on Evapotranspiration and Energy Balance Components Estimated by the TSEB Model. (Not published)

Sincerely,

Maria del Mar Alsina Marti

United States Department of Agriculture

Research, Education, and Economics
Agricultural Research Service

June 1, 2021

To Whom It May Concern:

I hereby give permission to Mahyar Aboutalebi to reprint the following material in his dissertation:

Aboutalebi, M.; Torres-Rua, A.F.; McKee, M.; Kustas, W.P.; Nieto, H.; Alsina, M.M.; White, A.; Prueger, J.H.; McKee, L.; Alfieri, J.; Hipps, L.; Coopmans, C.; Dokoozlian, N. Incorporation of Unmanned Aerial Vehicle (UAV) Point Cloud Products into Remote Sensing Evapotranspiration Models. Remote Sens. 2020, 12, 50. https://doi.org/10.3390/rs12010050

Aboutalebi, M.; Torres-Rua, A.F.; McKee, M.; Kustas, W.P.; Nieto, H.; Alsina, M.M.; Sanchez, L.; Prueger, J.H.; McKee, L.; Alfieri, J.; Hipps, L.; Coopmans, C.; Dokoozlian, N. Downscaling UAV Land Surface Temperature using a Coupled Wavelet-Machine Learning-Optimization Algorithm and Its Impact on Evapotranspiration and Energy Balance Components Estimated by the TSEB Model. (Not published)

Sincerely,

Joseph G. Alfieri

Hydrology & Remote Sensing Laboratory
Beltsville Agricultural Research Center, Building 007, Room 104
10300 Baltimore Avenue, Beltsville, Maryland 20705

Date: June 2, 2021

To Whom It May Concern:

I hereby give permission to Mahyar Aboutalebi to reprint the following material in his dissertation:

Aboutalebi, M.; Torres-Rua, A.F.; McKee, M.; Kustas, W.P.; Nieto, H.; Alsina, M.M.; Sanchez, L.; Prueger, J.H.; McKee, L.; Alfieri, J.; Hipps, L.; Coopmans, C.; Dokoozlian, N. Downscaling UAV Land Surface Temperature using a Coupled Wavelet-Machine Learning-Optimization Algorithm and Its Impact on Evapotranspiration and Energy Balance Components Estimated by the TSEB Model. (Not published)

Sincerely,

Lynn McKee

Date: June 2, 2021

To Whom It May Concern:

I hereby give permission to Mahyar Aboutalebi to reprint the following material in his dissertation:

Aboutalebi, M.; Torres-Rua, A.F.; McKee, M.; Kustas, W.P.; Nieto, H.; Alsina, M.M.; White, A.; Prueger, J.H.; McKee, L.; Alfieri, J.; Hipps, L.; Coopmans, C.; Dokoozlian, N. Incorporation of Unmanned Aerial Vehicle (UAV) Point Cloud Products into Remote Sensing Evapotranspiration Models. Remote Sens. 2020, 12, 50. https://doi.org/10.3390/rs12010050

Sincerely,

Lynn McKee

June 2, 2021

To Whom It May Concern:

I hereby give permission to Mahyar Aboutalebi to reprint the following material in his dissertation:

Aboutalebi, M.; Torres-Rua, A.F.; McKee, M.; Kustas, W.P.; Nieto, H.; Alsina, M.M.; White, A.; Prueger, J.H.; McKee, L.; Alfieri, J.; Hipps, L.; Coopmans, C.; Dokoozlian, N. Incorporation of Unmanned Aerial Vehicle (UAV) Point Cloud Products into Remote Sensing Evapotranspiration Models. Remote Sens. 2020, 12, 50. https://doi.org/10.3390/rs12010050

Sincerely,

William Alexander White

Date: November 8, 2021

To Whom It May Concern:

I hereby give permission to Mahyar Aboutalebi to reprint the following material in his dissertation:

Aboutalebi, M., Torres-Rua, A.F., Kustas, W.P., Nieto, H., Coopmans, C. and McKee, M. Assessment of different methods for shadow detection in high-resolution optical imagery and evaluation of shadow impact on calculation of NDVI, and evapotranspiration. Irrig Sci 37, 407–429 (2019). https://doi.org/10.1007/s00271-018-0613-9

Aboutalebi, M.; Torres-Rua, A.F.; McKee, M.; Kustas, W.P.; Nieto, H.; Alsina, M.M.; White, A.; Prueger, J.H.; McKee, L.; Alfieri, J.; Hipps, L.; Coopmans, C.; Dokoozlian, N. Incorporation of Unmanned Aerial Vehicle (UAV) Point Cloud Products into Remote Sensing Evapotranspiration Models. Remote Sens. 2020, 12, 50. https://doi.org/10.3390/rs12010050

Aboutalebi, M.; Torres-Rua, A.F.; McKee, M.; Kustas, W.P.; Nieto, H.; Alsina, M.M.; Sanchez, L.; Prueger, J.H.; McKee, L.; Alfieri, J.; Hipps, L.; Coopmans, C.; Dokoozlian, N. Downscaling UAV Land Surface Temperature using a Coupled Wavelet-Machine Learning-Optimization Algorithm and Its Impact on Evapotranspiration and Energy Balance Components Estimated by the TSEB Model. (Not published)

Sincerely

Digitally signed by NIETO SOLANA HECTOR - 52876942B the date 11/08/2021 with a digital certificate issued by AC FNMT Usuarios

Gmail **mahyar aboutalebi <mahyar.aboutalebi@gmail.com>**

Permission to use

Sanchez, Luis <Luis.Sanchez@ejgallo.com> Wed, Jun 9, 2021 at 1:59 PM
To: mahyar aboutalebi <mahyar.aboutalebi@gmail.com>

Signed!

From: mahyar aboutalebi <mahyar.aboutalebi@gmail.com>
Sent: Tuesday, June 08, 2021 10:29 PM
To: Sanchez, Luis <Luis.Sanchez@ejgallo.com>
Subject: Permission to use

Hi Luis,

Utah State University's library requires me to provide a permission-to-use letter from all co-authors of my papers for publishing a digital version of my dissertation. I appreciate it if you could sign the following statement and send it to me.

Thanks,

Mahyar

Date:

To Whom It May Concern:

I hereby give permission to Mahyar Aboutalebi to reprint the following material in his dissertation:

Aboutalebi, M.; Torres-Rua, A.F.; McKee, M.; Kustas, W.P.; Nieto, H.; Alsina, M.M.; Sanchez, L.; Prueger, J.H.; McKee, L.; Alfieri, J.; Hipps, L.; Coopmans, C.; Dokoozlian, N. Downscaling UAV Land Surface Temperature using a Coupled Wavelet-Machine Learning-Optimization Algorithm and Its Impact on Evapotranspiration and Energy Balance Components Estimated by the TSEB Model. (Not published)

Sincerely,

Luis Sanchez

Gmail **mahyar aboutalebi <mahyar.aboutalebi@gmail.com>**

Permission to use letter

Dokoozlian, Nick <Nick.Dokoozlian@ejgallo.com> Wed, Jun 2, 2021 at 7:45 AM
To: mahyar aboutalebi <mahyar.aboutalebi@gmail.com>

From: mahyar aboutalebi <mahyar.aboutalebi@gmail.com>
Sent: Tuesday, June 01, 2021 10:49 PM
To: Hector Nieto <hector.nieto.solana@gmail.com>; Nieto, Hector <hector.nieto@irta.cat>; Mimar Alsina <mimaralsina@gmail.com>; Alsina Marti, Maria del Mar <MariadelMar.Alsina@ejgallo.com>; White, Alex <Alex.White@ars.usda.gov>; Alfieri, Joe <joe.alfieri@usda.gov>; Cal Coopmans <cal.coopmans@usu.edu>; Cal Coopmans <coopmans@gmail.com>; John.Prueger@ars.usda.gov; Lynn.McKee@ars.usda.gov; Dokoozlian, Nick <Nick.Dokoozlian@ejgallo.com>
Subject: Permission to use letter

Dear co-authors,

Utah State University's library requires me to provide a permission-to-use letter from all co-authors of my papers for publishing a digital version of my dissertation. I appreciate it if you could sign the following statement and send it to me.

Thanks,

Mahyar

Date:

To Whom It May Concern:

I hereby give permission to Mahyar Aboutalebi to reprint the following material in his dissertation:

Aboutalebi, M.; Torres-Rua, A.F.; McKee, M.; Kustas, W.P.; Nieto, H.; Alsina, M.M.; White, A.; Prueger, J.H.; McKee, L.; Alfieri, J.; Hipps, L.; Coopmans, C.; Dokoozlian, N. Incorporation of Unmanned Aerial Vehicle (UAV) Point Cloud Products into Remote Sensing Evapotranspiration Models. Remote Sens. 2020, 12, 50. https://doi.org/10.3390/rs12010050

Sincerely,

Nick Dokoozlian

E&J Gallo Winery

Gmail mahyar aboutalebi <mahyar.aboutalebi@gmail.com>

Permission to use (2)

Dokoozlian, Nick <Nick.Dokoozlian@ejgallo.com> Wed, Jun 2, 2021 at 7:25 AM
To: mahyar aboutalebi <mahyar.aboutalebi@gmail.com>

Is this ok? Thank you – Nick

From: mahyar aboutalebi <mahyar.aboutalebi@gmail.com>
Sent: Tuesday, June 01, 2021 11:20 PM
To: Hector Nieto <hector.nieto.solana@gmail.com>; Nieto, Hector <hector.nieto@irta.cat>; Alsina Marti, Maria del Mar <MariadelMar.Alsina@ejgallo.com>; Mimar Alsina <mimaralsina@gmail.com>; Sanchez, Luis <Luis.Sanchez@ejgallo.com>; John.Prueger@ars.usda.gov; Lynn.McKee@ars.usda.gov; Alfieri, Joe <joe.alfieri@usda.gov>; Cal Coopmans <cal.coopmans@usu.edu>; Cal Coopmans <coopmans@gmail.com>; Dokoozlian, Nick <Nick.Dokoozlian@ejgallo.com>
Subject: Permission to use (2)

Dear co-authors,

Utah State University's library requires me to provide a permission-to-use letter from all co-authors of my papers for publishing a digital version of my dissertation. I appreciate it if you could sign the following statement and send it to me.

Thanks,

Mahyar

Date:

To Whom It May Concern:

I hereby give permission to Mahyar Aboutalebi to reprint the following material in his dissertation:

Aboutalebi, M.; Torres-Rua, A.F.; McKee, M.; Kustas, W.P.; Nieto, H.; Alsina, M.M.; Sanchez, L.; Prueger, J.H.; McKee, L.; Alfieri, J.; Hipps, L.; Coopmans, C.; Dokoozlian, N. Downscaling UAV Land Surface Temperature using a Coupled Wavelet-Machine Learning-Optimization Algorithm and Its Impact on Evapotranspiration and Energy Balance Components Estimated by the TSEB Model. (Not published)

Sincerely,

Nick Dokoozlian

E&J Gallo Winery

Gmail mahyar aboutalebi <mahyar.aboutalebi@gmail.com>

Permission to use

Cal Coopmans <cal.coopmans@usu.edu> Tue, Oct 26, 2021 at 11:49 AM
To: mahyar aboutalebi <mahyar.aboutalebi@gmail.com>, Cal Coopmans <coopmans@gmail.com>, "c.r.coopmans@ieee.org" <c.r.coopmans@ieee.org>
Cc: Alfonso Torres <alfonso.torres@usu.edu>, Alfonso Torres-Rua <a.torres@aggiemail.usu.edu>

Mahyar, sorry for the delay. Yes, I approve. Good work!

From: mahyar aboutalebi <mahyar.aboutalebi@gmail.com>
Date: Tuesday, August 31, 2021 at 10:56 PM
To: Cal Coopmans <cal.coopmans@usu.edu>, Cal Coopmans <coopmans@gmail.com>, c.r.coopmans@ieee.org <c.r.coopmans@ieee.org>
Cc: Alfonso Torres <alfonso.torres@usu.edu>, Alfonso Torres-Rua <a.torres@aggiemail.usu.edu>
Subject: [EXT] Fwd: Permission to use

Hi Cal,

Utah State University's library requires me to provide a permission-to-use letter from all co-authors of my papers for publishing a digital version of my dissertation. I appreciate it if you could sign the following statement and send it to me.

Thanks,

Mahyar

Date:

To Whom It May Concern:

I hereby give permission to Mahyar Aboutalebi to reprint the following material in his dissertation:

Aboutalebi, M., Torres-Rua, A.F., Kustas, W.P., Nieto, H., Coopmans, C. and McKee, M. Assessment of different methods for shadow detection in high-resolution optical imagery and evaluation of shadow impact on calculation of NDVI, and evapotranspiration. Irrig Sci 37, 407–429 (2019). https://doi.org/10.1007/s00271-018-0613-9.

Aboutalebi, M.; Torres-Rua, A.F.; McKee, M.; Kustas, W.P.; Nieto, H.; Alsina, M.M.; White, A.; Prueger, J.H.; McKee, L.; Alfieri, J.; Hipps, L.; Coopmans, C.; Dokoozlian, N. Incorporation of Unmanned Aerial Vehicle (UAV) Point Cloud Products into Remote Sensing Evapotranspiration Models. Remote Sens. 2020, 12, 50. https://doi.org/10.3390/rs12010050

Aboutalebi, M.; Torres-Rua, A.F.; McKee, M.; Kustas, W.P.; Nieto, H.; Alsina, M.M.; Sanchez, L.; Prueger, J.H.; McKee, L.; Alfieri, J.; Hipps, L.; Coopmans, C.; Dokoozlian, N. Downscaling UAV Land Surface Temperature using a Coupled Wavelet-Machine Learning-Optimization Algorithm and Its Impact on Evapotranspiration and Energy Balance Components Estimated by the TSEB Model. (Not published)

Sincerely,

[Your Name]

We didn't hear back from John Prueger on signing the permission letter for the following papers:

(1) Incorporation of Unmanned Aerial Vehicle (UAV) Point Cloud Products into Remote Sensing Evapotranspiration Models. Remote Sens. 2020, 12, 50.
(2) Downscaling UAV Land Surface Temperature using a Coupled Wavelet-Machine Learning-Optimization Algorithm and Its Impact on Evapotranspiration and Energy Balance Components Estimated by the TSEB Model. (Not published).

mahyar aboutalebi *<mahyar.aboutalebi@gmail.com>* *Tue, Jun 8, 2021 at 10:32 PM*

To: John.Prueger@ars.usda.gov, john.prueger@usda.gov

Hi John,

Utah State University's library requires me to provide a permission-to-use letter from all co-authors of my papers for publishing a digital version of my dissertation. I appreciate it if you could sign the following statement and send it to me.

Thanks,

Mahyar

Date:

To Whom It May Concern:

I hereby give permission to Mahyar Aboutalebi to reprint the following material in his dissertation:

Aboutalebi, M.; Torres-Rua, A.F.; McKee, M.; Kustas, W.P.; Nieto, H.; Alsina, M.M.; White, A.; Prueger, J.H.; McKee, L.; Alfieri, J.; Hipps, L.; Coopmans, C.; Dokoozlian, N. Incorporation of Unmanned Aerial Vehicle (UAV) Point Cloud Products into Remote Sensing Evapotranspiration Models. Remote Sens. 2020, 12, 50. https://doi.org/10.3390/rs12010050

Aboutalebi, M.; Torres-Rua, A.F.; McKee, M.; Kustas, W.P.; Nieto, H.; Alsina, M.M.; Sanchez, L.; Prueger, J.H.; McKee, L.; Alfieri, J.; Hipps, L.; Coopmans, C.; Dokoozlian, N. Downscaling UAV Land Surface Temperature using a Coupled Wavelet-Machine Learning-Optimization Algorithm and Its Impact on Evapotranspiration and Energy Balance Components Estimated by the TSEB Model. (Not published)

Sincerely,

*[**YOUR NAME**]*

mahyar aboutalebi <mahyar.aboutalebi@gmail.com> Tue, Aug 31, 2021 at 9:58 PM

To: John.Prueger@ars.usda.gov, john.prueger@usda.gov
Cc: Alfonso Torres <alfonso.torres@usu.edu>, Alfonso Torres-Rua <a.torres@aggiemail.usu.edu>

Hi John,

Utah State University's library requires me to provide a permission-to-use letter from all co-authors of my papers for publishing a digital version of my dissertation. I appreciate it if you could sign the following statement and send it to me.

Thanks,

Mahyar

Date:

To Whom It May Concern:

I hereby give permission to Mahyar Aboutalebi to reprint the following material in his dissertation:

Aboutalebi, M.; Torres-Rua, A.F.; McKee, M.; Kustas, W.P.; Nieto, H.; Alsina, M.M.; White, A.; Prueger, J.H.; McKee, L.; Alfieri, J.; Hipps, L.; Coopmans, C.; Dokoozlian, N. Incorporation of Unmanned Aerial Vehicle (UAV) Point Cloud Products into Remote Sensing Evapotranspiration Models. Remote Sens. 2020, 12, 50. https://doi.org/10.3390/rs12010050

Aboutalebi, M.; Torres-Rua, A.F.; McKee, M.; Kustas, W.P.; Nieto, H.; Alsina, M.M.; Sanchez, L.; Prueger, J.H.; McKee, L.; Alfieri, J.; Hipps, L.; Coopmans, C.; Dokoozlian, N. Downscaling UAV Land Surface Temperature using a Coupled Wavelet-Machine Learning-Optimization Algorithm and Its Impact on Evapotranspiration and Energy Balance Components Estimated by the TSEB Model. (Not published)

Sincerely,

*[**YOUR NAME]***

Curriculum Vitae
Mahyar Aboutalebi
(Last Updated on: 07/19/2020)

PERSONAL DETAILS

Website: www.mahyarona.com
Email: mahyar.aboutalebi@gmail.com
Google Scholar: https://goo.gl/t4K6qz
Cell: +1 435 557 6271
Homepage: https://goo.gl/gojVaW
GitHub: https://github.com/Mahyarona
Address: Utah State University, Utah Water Research Laboratory, 1600 Canyon Rd, Logan, UT 84321.

EDUCATION

PhD Candidate in Civil and Environmental Engineering, Remote Sensing in Precision Agriculture (2016-present), Utah State University, Logan, Utah.
PhD thesis: Improvement opportunities in the Two-Source Energy Balance Model for ET using UAV imagery and point cloud information.
Supervisor: Dr. Alfonso Torres-Rua

Master of Science in Agricultural Engineering – Water Resources (2011-2014)
College of Agriculture and Natural Resources, Faculty of Agricultural Engineering and Technology, Department of Irrigation and Reclamation Engineering, University of Tehran
M.Sc. thesis: Multi-objective optimization of water quality monitoring network in river reservoir system under injection of sudden contamination
Supervisor: Dr. Omid Bozorg Haddad

Bachelor of Science in Agricultural Engineering - Water (2007-2011)
College of Agriculture and Natural Resources, Faculty of Agricultural Engineering and Technology, Department of Irrigation and Reclamation Engineering, University of Tehran

HONORS AND AWARDS

- Outstanding PhD Scholar of the Year, 2020. Link
- Top Peer Reviewer in the Global Peer Review Awards 2019. Link
- UWRL Outstanding Student Spotlight, 2019. Link
- Best Paper Award in 'Autonomous Air and Ground Sensing Systems for Agricultural Optimization and Phenotyping IV' Conference, April 2019. Link
- Winner of "Water Data Visualization Competition". Link
- Best Reviewer Award 2018, Remote Sensing Journal, MDPI. Link
- Runner-up for the 'Autonomous Air and Ground Sensing Systems for Agricultural Optimization and Phenotyping III' Conference Best Paper Award, 2018. Link
- Awarded from J. Paul Riley AWRA Paper Competition, 2017. Link
- Awarded Full Scholarship of PhD Program, Utah State University, 2016-2020.
- Outstanding Master's Thesis Award issued by Water & Wastewater Association

RESEARCH EXPERIENCES

- Evapotranspiration, yield and soil moisture modelling using UAV high-resolution imagery
- LiDAR and Point Cloud datasets in order to derived canopy structural parameters

- Downscaling land surface temperature using a wavelet-machine learning technique
- Design of water quality monitoring systems
- Flood inundation map using remote sensing information and physical-based models
- Simulation-optimization modelling for water resources management

RESEARCH INTEREST

Application of remote sensing in surface hydrology and groundwater
Precision agriculture activities
Machine Learning
Multi-Objective Optimization Algorithms

PUBLICATIONS (161 citations- Google Scholar)

- **Remote Sensing**

1- **Aboutalebi, M.,** Torres-Rua, A., McKee, M., Kustas, W. P., Nieto, H., Alsina, M., White, A., Prueger, J., McKee, L., Alfieri, J., Hipps, L., Coopmans, C., and Dokoozlian, N. (2019) "Incorporation of Unmanned Aerial Vehicle (UAV) Point Cloud Product into Remote Sensing Evapotranspiration Models", **Remote Sensing**, Link

2- Garousi-Nejad, I., Tarboton, D., **Aboutalebi, M.,** and Torres-Rua, A., (2019) "Terrain analysis enhancements to the height above nearest drainage flood inundation mapping method," **Water Resources Research.** Link

3- **Aboutalebi, M.,** Torres-Rua, A., Allen, N. (2018). "Spatial and Temporal Analysis of Precipitation and Effective Rainfall using Gauge Observations, Satellite, and Gridded Climate Data for Agricultural Water Management in the Upper Colorado River Basin", **Remote Sensing.** Link

4- **Aboutalebi, M.,** Torres-Rua, A., Kustas, W.P., Nieto, H., Coopmans, C., and McKee, M. (2018). "Assessment of different methods for shadow detection in high-resolution imagery and evaluation of shadows impact on calculation of NDVI, LAI, and evapotranspiration", **Irrigation science.** Link

- **Water Resources Optimization Methods**

5- **Aboutalebi, M.,** Bozorg Haddad, O., Sarzaiem, P., and Loaiciga, H.A., (2019). "Application of teaching-learning-based optimization (TLBO) algorithm for nonlinear Muskingum model parameters estimation", **Hydrological Sciences Journal,** Major Revision.

6- Bozorg-Haddad, O., Mani, M., **Aboutalebi, M.,** and Loaiciga, H.A. (2017). "Choosing an optimization method for water resources problems based on the features of their solution spaces", **Journal of Irrigation and Drainage Engineering**, 144 (2). Link

7- **Aboutalebi, M.,** Bozorg Haddad, O., and Loaiciga, H.A., (2016). "Multi-objective design of water-quality monitoring networks in river-reservoir systems", **Journal of Environmental Engineering**, DOI : 10.1061/(ASCE)EE.1943-7870.0001155. Link

- **Machine Learning**

8- Bozorg-Haddad, O., **Aboutalebi, M.,** and Loaiciga, H.A. (2018). "Real-time reservoir operation using data mining techniques", **Environmental Monitoring and Assessment.** Link

9- **Aboutalebi, M.,** Bozorg Haddad, O., and Loaiciga, H.A., (2016). "Simulation of methyl tertiary butyl ether concentrations in river-reservoir systems using support vector regression", ***Journal of* Irrigation and Drainage Engineering**, DOI: 10.1061/(ASCE)IR.1943-4774.0001007. Link

10- **Aboutalebi, M.,** Bozorg Haddad, O., and Loaiciga, H.A., (2015). "Application of the SVR-NSGAII to hydrograph routing in open channels", **Journal of Irrigation and Drainage Engineering**, 142 (3), DOI : 10.1061/(ASCE)IR.1943-4774.0000969, Link

11- **Aboutalebi, M.,** Bozorg Haddad, O., and Loaiciga, H.A., (2015). "Optimal monthly reservoir operation rules for hydropower generation derived with SVR- NSGAII". **Journal of Water**

Resources Planning and Management, 141 (11), DOI :10.1061/(ASCE)WR.1943-5452.0000553, Link

- **Human-Environment Interactions**

12- Bozorg-Haddad, O., Zolghadr-Asli, B., Sarzaeim, P., **Aboutalebi, M.**, Chu, X., and Loaiciga, H.A. (2019). "Evaluation of water shortage crisis in the Middle East and possible remedies", **Journal of Water Supply: Research and Technology - AQUA**, Link

13- Bozorg-Haddad, O., **Aboutalebi, M.**, Chu, X., and Loaiciga, H.A. (2019). "Assessment of potential of intraregional conflicts, interbasin water transfers, and their impacts on the water resources", **Environmental Monitoring and Assessment**, Link.

Discussion and Closure (peer-reviewed):

1- **Aboutalebi, M. (2018).** Discussion of "Equation to Predict Riverine Transport of Suddenly Discharged Pollutants", Journal of Irrigation and Drainage Engineering, 144 (4). Link

2- **Aboutalebi, M.,** Bozorg-Haddad, O., and Loaiciga, H.A. (2017). Closure to "Simulation of Methyl Tertiary Butyl Ether concentrations in river-reservoir systems using support vector regression", Journal of Irrigation and Drainage Engineering, 143 (6). Link

3- **Aboutalebi, M.** and Garousi-Nejad, I., (2015). "Discussion of Application of the water cycle algorithm to the optimal operation of reservoir systems". Journal of Irrigation and Drainage Engineering. DOI: 10.1061/(ASCE)IR.1943-4774.0000947. Link

4- Garousi-Nejad, I., Bozorg Haddad, O., and **Aboutalebi, M.,** (2015). "Discussion of investigating parameters of two-point hedging policy for operating a storage reservoir". ISH Journal of Hydraulic Engineering, 21(3), 312-314 DOI: 10.1080/09715010.2015.1021282. Link

5- Bozorg Haddad, O., **Aboutalebi, M.,** and Garousi-Nejad, I., (2014). "Discussion of Hydro climatic stream flow prediction using least square-support vector". ISH Journal of Hydraulic Engineering, 20(3)-274-275. Link

6- Bozorg Haddad, O., **Aboutalebi, M.,** and Marino, M. A., (2014). "Discussion of Prediction of missing rainfall data using conventional and artificial neural network". ISH Journal of Hydraulic Engineering, 19(2), 76-77. Link

Conference

1- **Aboutalebi, M.,** Torres-Rua, A., McKee, M., Kustas, W. P., Nieto, H., Alsina, M., White, A., Prueger, J., McKee, L., Alfieri, J., Hipps, L., Coopmans, C., and Dokoozlian, N. "Deriving Daily Evapotranspiration from Multiple Unmanned Aerial Vehicle (UAV) Thermal Imageries and High Frequency Ground Thermal Measurements", SPIE DEFENSE + Commercial Sensing 2020, *Anaheim, CA.*

2- **Aboutalebi, M.,** Torres-Rua, A., McKee, M., Nieto, H., Kustas, W.P., Sanchez, L., Alsina, M., White, W.A., Hipps, L., Prueger, J.H., McKee, L., Alfieri, J., Dokoozlian N., and Coopmans, C. (2019) "Incorporation of Unmanned Aerial Vehicle (UAV) Point Cloud Product into Remote Sensing Evapotranspiration Models and Yield Estimation in Grapevine Vineyards", AGU Annual Meeting 2019, San Francisco, California. Link

3- **Aboutalebi, M.,** Nieto, H., Torres-Rua, A., McKee, M., Kustas, W.P., Coopmans, C., Alfieri, J., White, W.A., McKee, L., Hipps, L., Prueger, J.H. (2019) "Two source energy balance model (TSEB) with internal LAI estimation for evapotranspiration estimation using sUAS high-resolution imagery over vineyards" AMS Annual Meeting 2019, Phoenix, Arizona. Link

4- **Aboutalebi, M.**, Torres-Rua, A., McKee, M., Kustas, W.P., Nieto, H., and Coopmans, C. "Validation of Digital Terrain Models Retrieved from UAV Point Clouds using Geometrical Information from Shadows." SPIE DEFENSE + Commercial Sensing 2019, *Baltimore, Maryland.* Link

5- **Aboutalebi, M.**, Torres-Rua, A., McKee, M., Nieto, H., Kustas, W.P., and Coopmans, C. "The Impact of Shadows on Partitioning of Radiometric Temperature to Canopy and Soil Temperature Based on the Contextual Two-Source Energy Balance Model (TSEB-2T)." SPIE DEFENSE + Commercial Sensing 2019, *Baltimore, Maryland.* Link

6- **Aboutalebi, M.**, Allen, N., Torres-Rua, A., McKee, M., and Coopmans, C. "Estimation of Soil Moisture at Different Soil Levels using Data Mining Techniques and UAV Multispectral Imagery" SPIE DEFENSE + Commercial Sensing 2019, *Baltimore, Maryland.* Link

7- McKee, M., Torres-Rua, **Aboutalebi, M.** Nassar, A., Coopmans, C., Kustas, W., Gao, F., Dokoozlian, N., Sanchez, L., Maati, A. "Challenges that beyond-visual-line-of-sight technology will create for UAS-based remote sensing in agriculture" SPIE DEFENSE + Commercial Sensing 2019, *Baltimore, Maryland.* Link

8- Torres-Rua, A., **Aboutalebi, M.**, Wright, T., Nassar, A., Guillevic, P., Hipps, L., Gao, F., Jim, K., Alsina, M., Coopmans, C., McKee, M., and Kustas, W. P. "Estimation of surface thermal emissivity in a vineyard for UAV microbolometer thermal cameras using NASA HyTES hyperspectral thermal, and landsat and AggieAir optical data" SPIE DEFENSE + Commercial Sensing 2019, *Baltimore, Maryland.* Link

9- **Aboutalebi, M.,** Torres-Rua, A., McKee, M., Nieto, H., Kustas, W.P., Prueger, J.H., McKee, L., Alfieri, J., Hipps, L., Coopmans, C. (2018). "Assessment of Landsat Harmonized sUAS reflectance products using point spread function (PSF) on vegetation indices (VIs) and evapotranspiration (ET) using the two-source energy balance (TSEB) model", AGU Fall Meeting 2018, Washington, D.C. Link

10- Torres-Rua, A., **Aboutalebi, M.,** Esfahani, L., Elarab, M., Kustas, W. P., McKee, M., and Coopmans, C. (2018). "Fusion of satellite and UAV imagery and big data for smarter farming", AGU Fall Meeting 2018, Washington, D.C. Link

11- Nassar, A., Nieto, H., **Aboutalebi, M.,** Torres-Rua, A., McKee, M., Kustas, W.P., Prueger, J.H., McKee, L., Alfieri, J., Hipps, L., Coopmans, C. (2018). "Pixel resolution sensitivity analysis for the estimation of evapotranspiration using the two-source energy balance model and sUAS imagery under agricultural complex canopy environments ", AGU Fall Meeting 2018, Washington, D.C. Link

12- Garousi-Nejad, I., Tarboton, D., **Aboutalebi, M.,** and Torres-Rua, A. "Assessment and enhancement of National Water Model height above nearest drainage flood inundation mapping using Planet CubeSat for the 2017 Bear River flood event" AGU Fall Meeting 2018, Washington, D.C. Link

13- **Aboutalebi, M.,** Torres-Rua, A., and Allen, N. (2018). "Multispectral Remote Sensing for Yield Estimation Using High-Resolution Imagery from an Unmanned Aerial Vehicle." SPIE DEFENSE + Commercial Sensing 2018, *Orlando, Florida.* Link

14- **Aboutalebi, M.,** Torres-Rua, A., McKee, M., Kustas, W.P., Nieto, H., and Coopmans, C. (2018). "Behavior of vegetation/soil indices in shaded and sunlit pixels and evaluation of different shadow compensation methods using UAV high-resolution imagery over vineyards." SPIE DEFENSE + Commercial Sensing 2018, *Orlando, Florida.* Link

15- McKee, M., Nassar, A., Torres-Rua, A., **Aboutalebi, M.,** and Kustas, W.P., "Implications of sensor inconsistencies and remote sensing error in the use of small unmanned aerial systems for generation of information products for agricultural management" SPIE DEFENSE + Commercial Sensing 2018, *Orlando, Florida.* Link

16- **Aboutalebi, M.,** Torres-Rua, A., McKee, M., Kustas, W.P., and Nieto, H. (2017). "Evaluation of different shadow detection and restoration methods and their impact on vegetation indices using UAV high-resolution imageries over vineyards." AGU Fall meeting 2017, *New Orleans, Louisiana.* Link

17- **Aboutalebi, M.** (2017). "Satellite-based Prediction of Internal Migratory Movement under the Lack of Sufficient water for the Entire U.S." Spring Runoff Conference, *Logan, Utah.*

18- **Aboutalebi, M.,** and Bozorg Haddad, O., (2014). "Support Vector Machine with Non-dominated sorting genetic algorithm for the monthly inflow prediction in hydropower reservoir". Proceedings of the Second International Conference on Advances in Civil, Structural and Environmental Engineering-ACSEE, *Zurich, Switzerland, 25-26, October.*

GRANT-WRITING EXPERIENCE (Not funded)

Aboutalebi, M. (2018-2019). Improving Estimation of Plant Canopy Evapotranspiration and Stress Using UAV-derived Canopy Structure Information, NASA Earth and Space Science Fellowship (NESSF), $30,000.

REVIEWER For JOURNALS (reviewed 88 submissions, Link)

1-Science of the total environment (Elsevier)
2- Remote Sensing (MDPI)
3- Water (MDPI)
4- Sustainability (MDPI)
5- Forest (MDPI)
6- Hydrology Research (IWA)
7- Journal of Water and Climate Change (IWA)
8- Journal of Water Supply (IWA)
9- Interdisciplinary Sciences: Computational Life Sciences (Springer)
10- Irrigation and Drainage (WILEY)

PROGRAMMING EXPERIENCES

1- MATLAB programming (Advanced)
2- ArcGIS Pro (Advanced)
3- LINGO (Advanced)
4- Python (Intermediate)
5- ERDAS Imagine (Intermediate)
6- Google Earth Engine (Intermediate)
7- Jupyter Notebook (Intermediate)

FIELD EXPERIMENTS

1- LAI measurements with LAI-2200 LICOR sensor
2- Real-time kinematic (RTK) GPS
3- UAV sensor calibration
4- Soil moisture measurement with Augur kit

PERFORMED TASKS

1- Carried out TA for Agricultural Water Management, College of Civil and Environmental Engineering, Utah State University, USA, 2019
2- Carried out TA for Remote Sensing of Land Surfaces, College of Civil and Environmental Engineering, Utah State University, USA, 2018 and 2019
3- Carried out TA for Water resources engineering, College of Agriculture and Natural Resources, University of Tehran, 2015
4- Carried out Workshop, Faculty of environment, "The basis of evolutionary algorithms and artificial intelligence in MATLAB programming", University of Tehran, 2015

MEMBERSHIP IN PROFESSIONAL SOCIETIES

Member, American Society of Civil Engineers (ASCE), 2015-present.
Member, American Geophysical Union (AGU), 2016-present
Member, American Meteorological Society (AMS), 2016-present